

2

AFAPL-TR-78-81  
Volume III

FOREIGN OBJECT IMPACT DESIGN CRITERIA

Albert F. Storace

General Electric Company  
Aircraft Engine Group  
Cincinnati, Ohio 45215



February 1982

Interim Report for 31 December 1978 - 31 December 1979

Approved for public release; distribution unlimited.

AERO PROPULSION LABORATORY  
AIR FORCE WRIGHT AERONAUTICAL LABORATORIES  
AIR FORCE SYSTEMS COMMAND  
WRIGHT-PATTERSON AIR FORCE BASE, OHIO 45433

DTIC  
ELECTE  
MAR 25 1982  
S B D

82 03 24 069

AD A 112447

DTIC FILE COPY

## NOTICE

When Government drawings, specifications, or other data are used for any purpose other than in connection with a definitely related Government procurement operation, the United States Government thereby incurs no responsibility nor any obligation whatsoever, and the fact that the Government may have formulated, furnished, or in any way supplied the said drawings, specifications, or other data, is not to be regarded by implication or otherwise as in any manner licensing the holder or any other person or corporation, or conveying any rights or permission to manufacture, use, or sell any patented invention that may in any way be related thereto.

This technical report has been reviewed and is approved for publication.

  
SANDRA DRAKE  
Project Engineer

  
ISAAC J. GERSHON  
Technical Area Manager,  
Propulsion Mechanical Design

FOR THE COMMANDER:

  
J. SHIPMAN, MAJ, USAF  
Chief, Components Branch

If your address has changed, if you wish to be removed from our mailing list, or if the addressee is no longer employed by your organization, please notify AFWAL/POTC WPAFB, OH 45433 to help us maintain a current mailing list.

Copies of this report should not be returned unless return is required by security considerations, contractual obligations, or notice on a specific document.

Unclassified  
SECURITY CLASSIFICATION OF THIS PAGE (When Data Entered)

REPORT DOCUMENTATION PAGE		READ INSTRUCTIONS BEFORE COMPLETING FORM
1. REPORT NUMBER AFAPL-TR-78-81, Vol III	2. GOVT ACCESSION NO. AD-A112 447	3. RECIPIENT'S CATALOG NUMBER
4. TITLE (and Subtitle) FOREIGN OBJECT IMPACT DESIGN CRITERIA		5. TYPE OF REPORT & PERIOD COVERED Interim Technical Report 31 Dec. 1978 - 31 Dec. 1979
7. AUTHOR(s) Albert F. Storace		6. PERFORMING ORG. REPORT NUMBER
9. PERFORMING ORGANIZATION NAME AND ADDRESS General Electric Company Aircraft Engine Group Cincinnati, Ohio 45215		8. CONTRACT OR GRANT NUMBER(s) F33615-77-C-5221
11. CONTROLLING OFFICE NAME AND ADDRESS Aero Propulsion Laboratory (AFWAL/POTC) Air Force Wright Aeronautical Laboratories Wright-Patterson Air Force Base, Ohio 45433		10. PROGRAM ELEMENT, PROJECT, TASK AREA & WORK UNIT NUMBERS 3006-12-33
14. MONITORING AGENCY NAME & ADDRESS (if different from Controlling Office)		12. REPORT DATE February 1982
		13. NUMBER OF PAGES 121
		15. SECURITY CLASS. (of this report) Unclassified
		15a. DECLASSIFICATION/DOWNGRADING SCHEDULE
16. DISTRIBUTION STATEMENT (of this Report)  Approved for public release; distribution unlimited.		
17. DISTRIBUTION STATEMENT (of the abstract entered in Block 20, if different from Report)		
18. SUPPLEMENTARY NOTES The computer program contained in this report is theoretical and in no way reflects any Air Force owned software programs.		
19. KEY WORDS (Continue on reverse side if necessary and identify by block number) Transient Structural Response      Fan/Compressor Blading Foreign Object Loading              Material Transient Response FOD Design Criteria                  Structural Failure Criteria Damage-Tolerant Design              Airfoil Structural Modeling		
20. ABSTRACT (Continue on reverse side if necessary and identify by block number) The program objective is to establish specific design criteria and provide the analytical design tools to assess and improve the foreign object damage (FOD) tolerance of turbine engine fan and compressor blading.  The program will aid in the design of more efficient, damage-tolerant blading by replacing trial-and-error FOD test and evaluation practices with systematic transient-structural-analysis methods, test procedures, and design criteria. → int		

DD FORM 1 JAN 73 1473 EDITION OF 1 NOV 65 IS OBSOLETE

Unclassified

SECURITY CLASSIFICATION OF THIS PAGE (When Data Entered)

Unclassified

SECURITY CLASSIFICATION OF THIS PAGE(When Data Entered)

Task I has been completed. A design structure was developed for the purposes of providing a consistent framework in which to constitute the design criteria, guiding the overall technical effort, and formulating a data foundation to define the problem environment.

The major part of Tasks II and III, development of the transient-structural response and interactive-loading models and interfacing these models, has been accomplished.

Task IV through XI ~~are currently underway and~~ address local and structural impact testing, material-property determination, error-band analysis, and the formulation of design criteria. All of the Task IV testing to establish the properties for the metallic materials in the program has been completed, and testing is currently underway to establish the properties for the composite materials that are under investigation.

>Tests and analysis for the generation of local and gross structural-damage design data are in progress, and bench testing of structural elements for analysis validation is nearing completion.

>Single-blade whirligig testing has started, and the R&D test plan for a full stage of shrouded F101 blades has been completed.

Initial FOD design criteria have been established preparatory to the formulation of final criteria which will be based on correlations between analysis and test.

Unclassified

SECURITY CLASSIFICATION OF THIS PAGE(When Data Entered)

//

# PREFACE

This report covers work performed by the Aircraft Engine Group at General Electric, Evendale, Ohio. This report covers work completed during the period 1 January 1979 through 31 December 1979. The contract, F33615-77-C-5221 was sponsored by the Aero Propulsion Laboratory, Air Force Systems Command, Wright-Patterson AFB, Ohio 45433, under Program Element 62203F, Project 3066, Task Area 12, Work Unit 33 and under the direction of Sandra K. Drake (AFWAL/POTC), Project Engineer. Albert F. Storace was technically responsible for the work and preparation of this report in fulfillment of the aforementioned contract.



Accession for	
AFIS	<input checked="" type="checkbox"/>
DTIC	<input type="checkbox"/>
Distribution/	
AFIS Utility Codes	
Dist All and/or Special	
A	

## TABLE OF CONTENTS

<u>Section</u>	<u>Page</u>
1.0 INTRODUCTION	1
2.0 SUMMARY	2
3.0 TASK I - DESIGN SYSTEM STRUCTURE	4
4.0 TASK II - TRANSIENT RESPONSE ANALYSIS MODELS	8
4.1 Introduction	8
4.2 First-Level Response Model (NOSAPM)	9
4.3 Second-Level Response Model (COMET-BLADE)	19
4.4 Interface With the Loading Model	24
5.0 TASK III - IMPACT LOADING MODEL	29
5.1 Introduction	29
5.2 Subtask A - Simulate Bird and Ice Impact Parameter	29
5.3 Subtask B - Loading Model Sensitivity Study	29
5.4 Subtask C - Formulation/Interfacing of Loading Models With Structural Models	32
5.4.1 Introduction	32
5.4.2 The Slicing Model	33
5.4.2.1 Slicing Model Development for Birds	33
5.4.2.2 Slicing Model for Ice Spheres	36
5.4.2.3 Slicing Model for Ice Slab	36
5.4.3 Bird-Slice Geometry Parametric Study Results	36
5.4.4 Fluid Flow Model of Impact	37
5.4.4.1 Surface Singularity Method - Superposition of Onset Flow and Surface Source Distribution.	40
5.4.4.2 The Body Surface Approximation	40
5.4.4.3 Solution Procedure	40
5.4.5 Structure of the Loading Model and Interface with the First-Level Response Model	41
5.4.6 Structure of the Loading Model and Interface with the Second-Level Response Model	42
5.4.7 Summary	43
5.5 Subtask D - Experimental Verification of Loading Models	46

TABLE OF CONTENTS (Continued)

<u>Section</u>		<u>Page</u>
6.0	TASK IV - MATERIAL RESPONSE AND FAILURE CRITERIA	48
6.1	Subtask A - Gross Structural Damage Properties	48
6.1.1	Introduction	48
6.1.2	Real-Blade Strain Rate	49
6.1.3	Material-Property Data	49
6.2	Subtask B - Local Leading-Edge Damage	57
6.2.1	Introduction	57
6.2.2	Overall Approach	61
6.3	Subtask C - Material-Screening Tests	61
6.3.1	Introduction	61
6.3.2	Testing and Analysis	62
7.0	TASK V - PARAMETRIC ANALYSIS	64
7.1	Introduction	64
7.2	Blades Selected for Analysis	64
7.3	Parametric Matrix	64
7.4	NOSAPM Modeling and Analysis	65
7.4.1	Normal-Impact Analysis	65
7.4.2	Comparison Between First- and Second-Level Analyses for Normal Impact	81
7.4.3	Comparison Between First-Level Analysis and Experimental Data for Normal Impact	83
7.4.4	Oblique-Impact Analysis	85
7.5	COMET Modeling and Oblique-Impact Analysis	89
8.0	TASK VI - STRUCTURAL ELEMENT TESTS	96
8.1	Introduction	96
8.2	Description of Tests	96
8.2.1	Composite Structural Specimens	96
8.2.2	Metal Structural Specimens	96
8.3	Discussion	98
9.0	TASK VII - ERROR-BAND ANALYSIS	103
9.1	Introduction	103
9.2	Properties Requiring an Error-Band Estimation	103
9.3	Damage Vector	103

TABLE OF CONTENTS (Concluded)

<u>Section</u>		<u>Page</u>
10.0	TASK VIII - FOREIGN OBJECT IMPACT DESIGN CRITERIA	105
10.1	Introduction	105
10.2	Design Criteria	105
10.2.1	Design Criteria for Use with Task II Transient Structural-Response Models and Task IV-A Test Data	106
10.2.2	Design Criteria Based on Task IV-A, B, and C Test Data and Methods	106
11.0	TASK IX - SINGLE-BLADE IMPACT TESTS	107
11.1	Introduction	107
11.2	Test Plan	107
11.3	Impact Testing	111
11.3.1	J79 Compressor Stage 1 Blade Testing	111
11.3.2	APSI Fan B/A1 Blade Testing	112
11.3.3	F101 Fan Stage 1 Blade Testing	112
11.4	Whirligig Facility	114
12.0	TASK X - FULL-STAGE-RESPONSE PREDICTION	116
12.1	Introduction	116
12.2	Analysis Approach	116
12.3	Response Predictions	116
13.0	TASK XI - FULL-SCALE IMPACT TESTS	117
13.1	Introduction	117
13.2	Test Plan	117
13.3	Impact Testing	118
13.3.1	F101 Fan Stage 1 Blades - Bird- Ingestion Test	118
13.3.2	F101 Fan Stage 1 Blades - Ice- Slab-Ingestion Test	118
13.4	Whirligig Facility	118
13.5	Gas Gun Facility	120
	REFERENCES	121



## LIST OF ILLUSTRATIONS

<u>Figure</u>		<u>Page</u>
1.	Program/Tasks Flow - Foreign Object Impact Design Criteria.	5
2.	Foreign Objective Impact Design Criteria Program Functional Organization.	6
3.	FOD Project Team.	7
4.	Three-Dimensional, Finite Element Used in NOSAPM.	10
5.	Three-Dimensional, Finite-Element Model of J79 Stainless Steel Compressor Blade.	12
6.	Three-Dimensional, Finite-Element Model of APSI B/A1 Fan Blade.	13
7.	Three-Dimensional, Finite-Element Model of F101 Titanium Fan Blade.	14
8.	Blade Modeling and Analysis System.	15
9.	Radial Displacement Due to Centrifugal Loading at 5000 RPM.	16
10.	NOSAPM 30-Element Model of Plate Rotating at 5000 RPM.	17
11.	Model Used in Formulation of Closed-Form Solution for Stresses and Displacements from Centrifugal Forces.	18
12.	Undeformed Plate.	20
13.	Plate Deformation at 100 $\mu$ sec (Scale Factor = 1).	21
14.	Plate Deformation at 220 $\mu$ sec (Scale Factor = 1).	22
15.	Plate Deformation at 100 $\mu$ sec (Scale Factor = 5).	23
16.	Plate Element Used in COMET-BLADE.	25
17.	Level 2 Transient-Response Model Formulated from a System of Plate Elements.	26
18.	Link-Up Between the Loading Model Subroutine and the Executive or Main Response-Model Program.	28

LIST OF ILLUSTRATIONS (Continued)

<u>Figure</u>		<u>Page</u>
19.	Cantilever Plate Definition Selected for Sensitivity Study.	30
20.	Three-Dimensional-Element Finite Model of Cantilever Plate Used in Sensitivity Study.	31
21.	Bird/Blade Interaction Geometry.	34
22.	Impulse-Momentum Principle; Bird is Treated as a Fluid Body.	44
23.	Generalized Bird-Impact Pressure/Time Profile Based on Experimental Results.	45
24.	Generalized Bird-Impact Geometry Profile Based on Experimental Results.	45
25.	Deflected-Shape Plots of Cantilever Plate Struck by Simulated (Gelatin) Bird for Analytical-Model Validation.	47
26.	Specimen for Low- and Intermediate-Strain-Rate Tests for Metals.	51
27.	Specimen for High-Strain-Rate Tests.	52
28.	Young's Modulus Vs. Strain Rate.	55
29.	Yield Stress Vs. Strain Rate.	56
30.	Modified ITTRI Specimen.	58
31.	Modified 10° Off-Axis Shear Specimen.	59
32.	Through-the-Thickness Test Specimen.	60
33.	Geometry of Test Impact.	66
34.	Finite-Element Model.	66
35.	Stress-Strain Curve Used in Analysis of Test Shot 20094.	67
36.	Pressure-Loading History.	69
37.	Stiffness Reformation and Equilibrium Iteration Strategy.	72

LIST OF ILLUSTRATIONS (Continued)

<u>Figure</u>		<u>Page</u>
38.	Lateral Displacement Along Chord Line.	73
39.	Lateral Displacement Along Centerline B-B.	74
40.	Lateral Deflection Under the Center of Impact.	75
41.	Lateral Tip Deflection.	76
42.	Deflected Shape Along Plate Centerline at $t = 500 \mu\text{sec}$ .	77
43.	Membrane Stress History at Center of Impact.	79
44.	Membrane Stress History at Root.	80
45.	Large Displacements.	82
46.	Impact Geometry.	84
47.	Finite-Element Model.	84
48.	Tip-Displacement History; NOSAPM Predictions Vs. Test for Simulated-Bird Impact.	86
49.	Deformed Geometry Profile; NOASPM Prediction Vs. Test for Simulated-Bird Impact.	87
50.	Pressure Distribution for $\theta = 24.4^\circ$ Impact on a Flat Plate.	88
51.	Impact Geometry and Pressure Distribution.	90
52.	Model of Blade/Bird Impact for COMET Analysis.	91
53.	Deflections at Leading Edge.	92
54.	Deflections at Nodal Positions Along Chord Line at 17-in. Radius.	93
55.	Interaction of Blade and Bird Along Chord at 17-in. Radius.	94
56.	Task VI B/A1 Composite Test Specimen Configurations.	97
57.	Tip Deflection Vs. Time for 3-Oz-Bird Impact at 70% Span on a Flat Ti Plate.	100

LIST OF ILLUSTRATIONS (Concluded)

<u>Figure</u>		<u>Page</u>
58.	Strain/Time Curve for Root Gage in Span Direction.	101
59.	Strain-Rate/Time Curve for Root Gage in Span Direction.	102
60.	Test Setup for J79 and APSI Blades.	108
61.	Test Setup for F101 Blades for Tasks IX and XI.	109
62.	J79 Blade and Injection Mechanism.	113
63.	Whirligig Test Facility.	115

## LIST OF TABLES

<u>Table</u>		<u>Page</u>
1.	First-Level (NOSAPM) Analysis Based on Finite-Element Method.	9
2.	Second-Level (COMET-BLADE) Analysis Based on Component-Element Methods.	27
3.	Blade Calculation Input Data Sheet of 3-Oz Bird.	38
4.	Blade Calculation Input Data Sheet for 1.5-lb Bird.	39
5.	Strain Rates of Metallic Material Characterization Tests.	50
6.	Density.	50
7.	Mechanical Properties Obtained for 8Al-1Mo-1V Titanium.	53
8.	Mechanical Properties Obtained for 410 Stainless Steel.	54
9.	Characterization Tests for B/Al and Stainless Steel Wire Mesh.	57
10.	Ballistic Limit Results (ft/sec).	62
11.	Charpy Test Results.	63
12.	Dayton Test Conditions.	68
13.	Characteristic Times.	70
14.	Some Task VI Impact Tests Conducted on Real Blades.	99
15.	Matrix of Error-Band Properties and Associated Damage Modes.	104
16.	Planned Test Conditions for Full-Stage Whirligig Impact Tests.	119

## 1.0 INTRODUCTION

The objective of this program is to develop and validate structural design criteria that account for the transient overloads produced by bird and ice impacts on turbine engine first-stage fan/compressor blades. This program is part of a continuing effort of the Air Force to minimize ownership costs by placing added emphasis on the derivation of durable, damage-tolerant, advanced-turbomachinery component designs.

Foreign object damage (FOD) in aircraft engines has been an increasing drain on defense economic resources. Present-generation engine blading designs have substantial material toughness and cross section to meet the mechanical and aeromechanical requirements, but they were not specifically designed for damage tolerance. The prevailing design state of the art concerning damage-tolerant blading is mostly empirical and based on experience from major incidents and associated ad hoc testing. The empirical approach to designing damage-tolerant blading requires considerable investment of resources and is sometimes incapable of providing directly predictable foreign-object-impact response of blading. This approach is not adequate for newer, more damage-prone blading designs incorporating lightweight materials (including advanced composites) and thinner cross sections to achieve improved performance.

Comprehensive design criteria based upon transient-structural-response tools are needed to achieve more efficient, damage-tolerant blading. This program will provide the necessary computer tools and validation testing to establish reliable design criteria to provide direct assessment of blade impact-damage tolerance and identify areas for improvement.

This program consists of 11 tasks that progressively develop the FOD design criteria from computer models, structural element and material property tests, and static and rotating single-blade tests to full- or partial-stage rotating tests. The 11 tasks are identified as follows:

- Task I - Design System Structure
- Task II - Transient Response Analysis Models
- Task III - Impact Loading Model
- Task IV - Material Response and Failure Criteria
- Task V - Parametric Analysis
- Task VI - Structural Element Tests
- Task VII - Error Band Analysis
- Task VIII - Foreign Object Impact Design Criteria
- Task IX - Single-Blade Impact Tests
- Task X - Full-Stage Response Prediction
- Task XI - Full-Scale Impact Tests

The design analysis methods and failure criteria derived in the course of this program will be applicable both to advanced composite materials and to monolithic materials for current and advanced fan/compressor blading.

## 2.0 SUMMARY

The program consists of 11 tasks to establish reliable FOD design criteria. The emphasis will be on determining the effects of the ingestion of birds and ice during takeoff and landing (which present the greatest hazards to aircraft engines).

The 11 tasks progressively develop the FOD design criteria from transient-structural-response computer models, test specimens, and single-blade tests to full- or partial-stage rotating rig tests. The transient-response computer models will be based on existing mathematical approaches and on existing computing programs that will be adjusted as required for the specific application of this study.

Task I has been completed. A design structure was developed for the purposes of providing a consistent framework in which to constitute the design criteria, guiding the overall technical effort, and formulating a data foundation to define the problem environment.

Tasks II through IX are currently underway and address the development of the transient-response and loading models, local and structural impact testing, material-property determination, error-band analysis, and the formulation of design criteria.

The preliminary and final designs of the transient-structural-response computer programs have been developed, and checkout is nearing completion. In addition, the coding for interfacing the bird-loading model (developed by the University of Dayton Research Institute) with the final-design response model (developed by General Electric) has been completed and checked out.

Models of the three first-stage blades (representing airfoils from Air Force inventory, production-development, and advanced-development engines) have been constructed, and bench impact testing of these blades has been completed.

Composite and metallic specimens for local impact and structural-element bench impact and material-property tests have been designed and fabricated. Plans defining the testing of these specimens and real blades have been completed and approved by the Air Force. Real-blade impact testing has been completed to establish the maximum strain rates needed for the material property tests.

A parametric matrix has been formulated to define the conditions and geometries that will be analyzed in Tasks V and X and to provide guidance in the structural tests of Tasks VI and IX. Transient analyses have been performance on plate-like structural models.

Work was performed on the compilation of relevant blade and impactor properties for use in the error-band analysis. FOD design criteria were established within the framework of the projected capabilities of the transient-structural-analysis computer tools developed in Tasks II and III.

Single-blade impact testing (whirligig) was completed on the J79 compressor Stage 1 steel blade, and data reduction/analysis is underway. This blade represents Air Force inventory airfoils.



### 3.0 TASK I - DESIGN SYSTEM STRUCTURE

A design system structure was developed, through the Task I effort, to establish a consistent framework in which to constitute FOD design criteria and guide the overall technical effort. This design system structure defines the objective and interfaces of the various multidisciplined tasks that must be satisfied to achieved meaningful design criteria, and it includes a data foundation that describes the problem environment.

Figure 1 depicts the interrelations between the major distinct activities of quantification of experience, analytic development, bench tests, rotating rig tests, and the work flow of the program.

The results of the Task I effort were documented in a Research/Development Test Plan<sup>1</sup> that was approved by the Air Force.

To conduct the program described in Figure 1, a team of technical personnel has been gathered from several organizations to utilize their specific technical expertise and FOD experience. These organizations are:

- General Electric Aircraft Engine Group (AEG)
- General Electric Corporate Research and Development Center (CR&DC)
- University of Dayton Research Institute (UDRI)

Figures 2 and 3 show the functional responsibilities of the participants and the organization.

\*Superscript numbers refer to references.



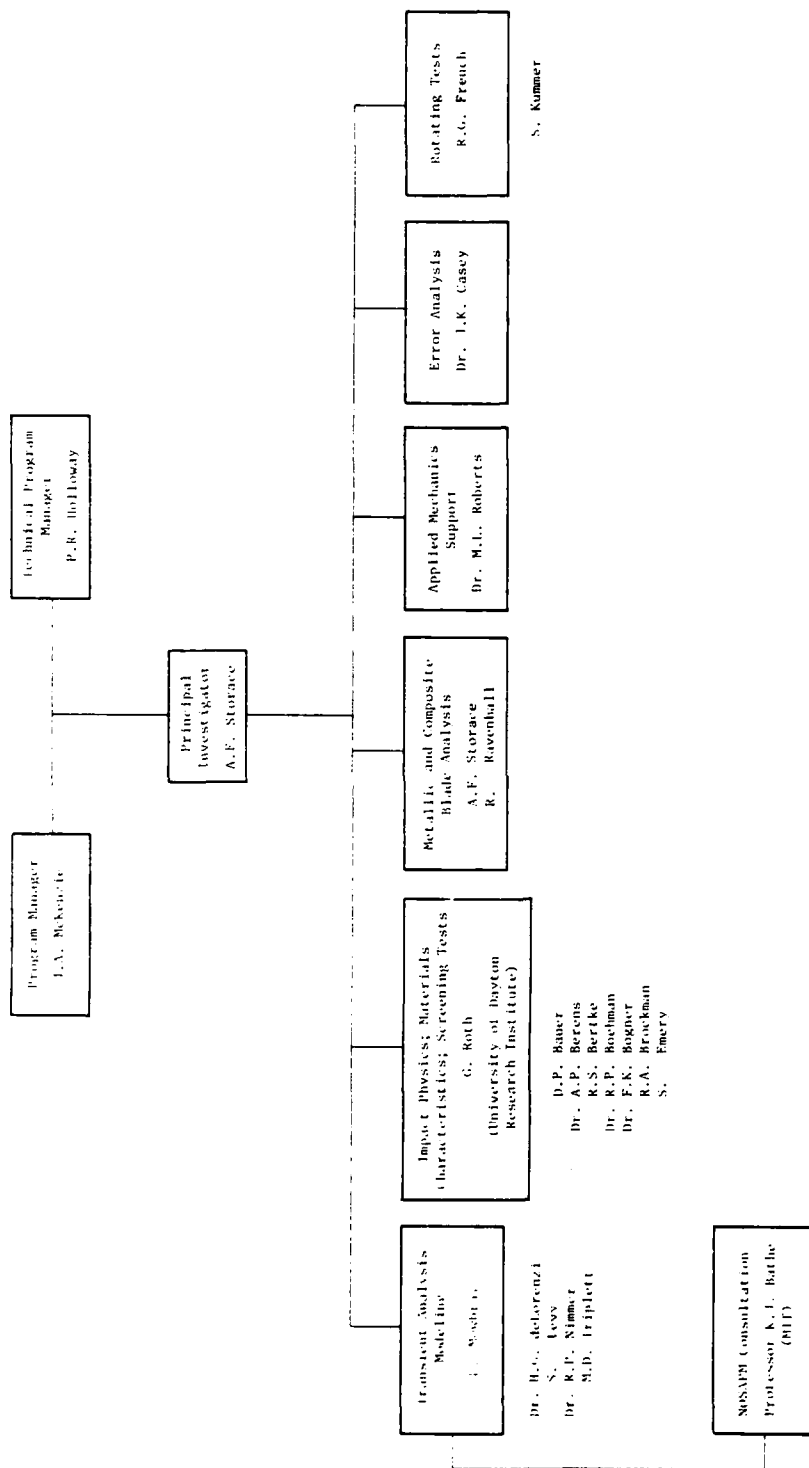


Figure 2. Foreign Object Impact Design Criteria Program Functional Organization.

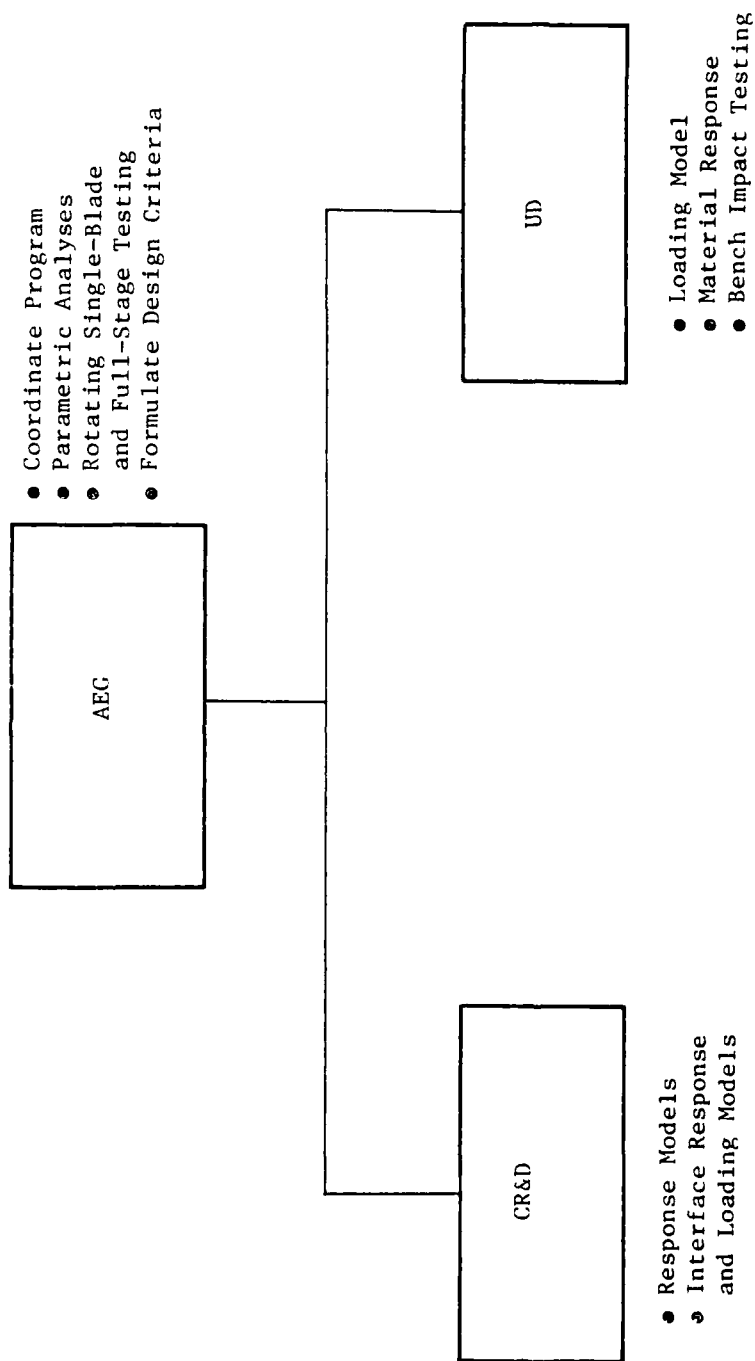


Figure 3. FOD Project Team.

#### 4.0 TASK II - TRANSIENT RESPONSE ANALYSIS MODELS

The first- and second-level models<sup>2</sup> selected for use in the transient-response analysis of first-stage fan and compressor blades were approved by the Air Force.

##### 4.1 INTRODUCTION

The transient response due to foreign object impact on first-stage fan and compressor blades will be analyzed on two different levels during the course of this program. The rationale for this approach is based on the fact that each level of analysis possesses intrinsic advantages which make it very attractive for the study of different aspects of the FOD problem. The first level of analysis will be accomplished with a modified version of the finite-element program NONSAP. This analysis will be capable of carrying out a very detailed analysis embracing local impact damage as well as gross structural damage. NONSAP is a very general and accurate package for nonlinear, finite-element analyses and employs three-dimensional (3-D) elements. The modified version used in this program will be called NOSAPM. This program has a library of three different time-integration techniques (Wilson <sup>6</sup>, Newmark, central difference) as well as two elastoplastic hardening models (kinematic hardening and isotropic hardening). This versatility will prove useful in finding the most efficient strategy for solution of the dynamic problem. However, the detail and versatility of this NONSAP package is obtained at the expense of high computing costs which could prove to be a problem during parametric design studies. As a result, the second-level analysis based on S. Levy's component-element method of transient dynamics<sup>3</sup> will be employed in situations where cost becomes an important factor. The savings in the Component Element Method (COMET) are accomplished through the use of simplified element models and an explicit time-integration technique that allows nonlinear structural-dynamics problems to be solved without physically assembling stiffness matrices. This Level 2 analysis will be somewhat less detailed, but experience in other fields including pipe whip<sup>4</sup>, locomotive dynamics, and nuclear fuel rod vibration<sup>5</sup> shows that the technique is as accurate as well as efficient tool. In addition to being of use in parametric studies, the lower cost of this level of analysis should prove to be an advantage in blade-interaction studies.

No dynamic crack-growth analyses will be incorporated into the first- and second-level analyses. Stresses and strains will simply be calculated and then used to indicate damage based on the design criteria to be formed as part of Task VIII. Plastic curl-back of blades will be considered. Graphical output of stresses and strains will be provided, and a method of implementing the results of the impact-damage design criteria within the structural codes will be incorporated. Based on the transient-response models of Task II and the damage criteria formulated in Task VIII, the final package would then indicate probable areas of failure as they are encountered in the analysis.

#### 4.2 FIRST-LEVEL RESPONSE MODEL (NOSAPM)

As indicated above, the program NOSAPM contains a wide range of tools that will be necessary in modeling the FOD problem. Specifically, in this analysis, the 3-D isoparametric element will be used. This element can be used with a variable number of nodal points ranging from 8 to 21 (see Figure 4). It is anticipated that 16-noded elements will be used to allow the blades to be modeled with one element through the thickness while still including the bending effects which will be most important in this problem. NOSAPM is capable of large-displacement, elastoplastic analysis and uses an efficient, out-of-core, equation solver. The inelastic material behavior will be modeled with a bilinear stress-strain curve, and both isotropic and kinematic hardening will be available for application. In the case of composite materials, a linear orthotropic material model is already available. Centrifugal stiffening has been incorporated in NOSAPM through the addition of a body-force (centrifugal) load vector. This load vector is used to calculate centrifugal displacements which are used as initial conditions for the transient response. The constant centrifugal-load vector is also added to the impact loads for each time step. The centrifugal displacements calculated by the initial state of the blade before the impact are also utilized in the calculation of eigenfrequencies and eigenmodes that indicate the effects of centrifugal stiffening.

If the strain-rate effects are found to be substantial, in the course of material characterization, they will also be included. Flexible root fixity as well as blade interaction at the shrouds will be handled with spring elements. Table 1 is a summary of the capabilities of NOSAPM.

Table 1. First-Level (NOSAPM) Analysis Based on Finite-Element Method.

- Blade model formulated from 3-D solid elements of from 8 to 21 nodes.
- Sixteen-noded elements have been selected (midsided nodes only for in-plane directions) for the blade models.
- NOSAPM is capable of large-displacement, elastoplastic analysis and uses an efficient, out-of-core, equation solver.
- The inelastic material behavior is modeled with a bilinear stress-strain curve, and both isotropic and kinematic hardening are available for application.
- For composite materials, a linear orthotropic material model is used.
- Centrifugal stiffening has been incorporated through the addition of a body-force (centrifugal) load vector.
- Flexible root fixity as well as blade interaction at the shrouds is handled with spring (Truss) elements.

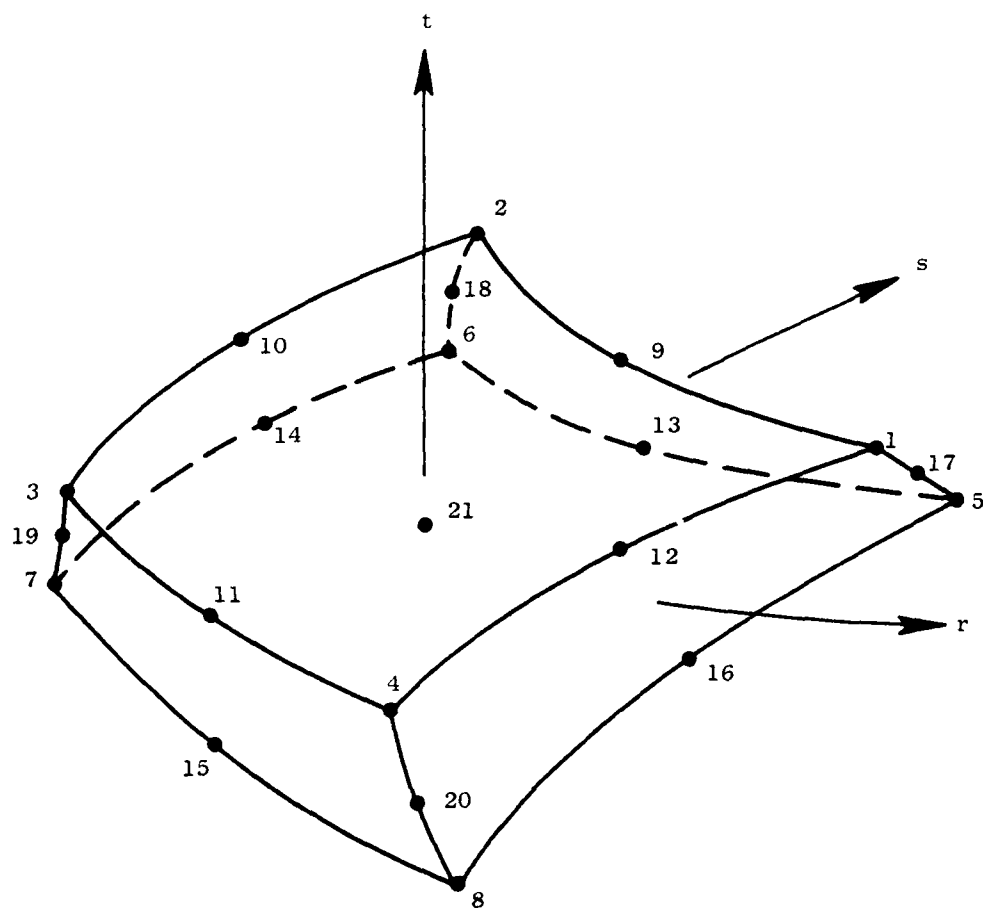


Figure 4. Three-Dimensional, Finite Element Used in NOSAPM.

Figures 5, 6, and 7 show NOSAPM three-dimensional models of the three first-stage blades selected for analysis in Task V. Figure 5 shows the unshrouded, stainless steel, J79 compressor first-stage blade. Figure 6 shows the unshrouded, boron/aluminum (B/Al) composite, first-stage fan blade developed in the Advanced Propulsion System Integration Program (APSI). And Figure 7 shows the shrouded, titanium, F101 first-stage fan blade.

In order to facilitate the running of NOSAPM from Evendale, a data-deck-generator program has been written. This program generates card images of the NOSAPM input data based on element and node files (created with an existing mesh-generator program available at Evendale) and on user input specified in the interactive time-sharing mode. The input data decks so created are transmitted to the WPAFB 6600 systems via the remote Evendale input/output (I/O) site to establish data files. Control of job execution in the batch mode is then accomplished at Evendale, through time-sharing, with the job output directed to the remote I/O site at Evendale. Work is proceeding on the coding of a deck-generator program for the second-level analysis, and Figure 8 shows a schematic of the steps required in generating and running blade models with the first- and second-level analyses.

Figure 9 shows the results of a check case used to verify the accuracy of the NOSAPM solution for displacements induced by centrifugal forces. The figure indicates excellent agreement between a closed-form solution and NOSAPM for centrifugal displacements in the radial direction for a flat-plate rotating at 5000 rpm. In NOSAPM this flat plate was modeled by the thirty 16-noded-element configuration shown in Figure 10. Referring to Figure 11, the expression for the closed-form solution was developed as follows. The elemental centrifugal force is:

$$dF = A \, dX \, (\rho/g) \, \omega^2 \, (r_1 + X) \quad (1)$$

where  $\rho/g$  is the mass density and  $\omega$  is the angular velocity. The centrifugal stress developed by the plate mass lying above the section defined by  $Z$  is:

$$\sigma = F/A = (\rho/g) \, \omega^2 \, \int_Z^{\ell} (r_1 + X) \, dX \quad (2)$$

$$\sigma = (\rho/g) \, \omega^2 \, [r_1 (\ell - Z) + (\ell^2 - Z^2)/2] \quad (3)$$

Radial strain is:

$$\epsilon_Z = dW/dZ \quad (4)$$

Radial displacement is:

$$W = \int_0^Z \epsilon_Z \, dZ \quad (5)$$

$$W = (\rho\omega^2/gE) \int_0^Z [r_1 (\ell - Z) + (\ell^2 - Z^2)/2] \, dZ \quad (6)$$

$$W = (\rho\omega^2/gE) [r_1 (\ell Z - Z^2/2) + (\ell^2 Z - Z^3/3)/2] \quad (7)$$



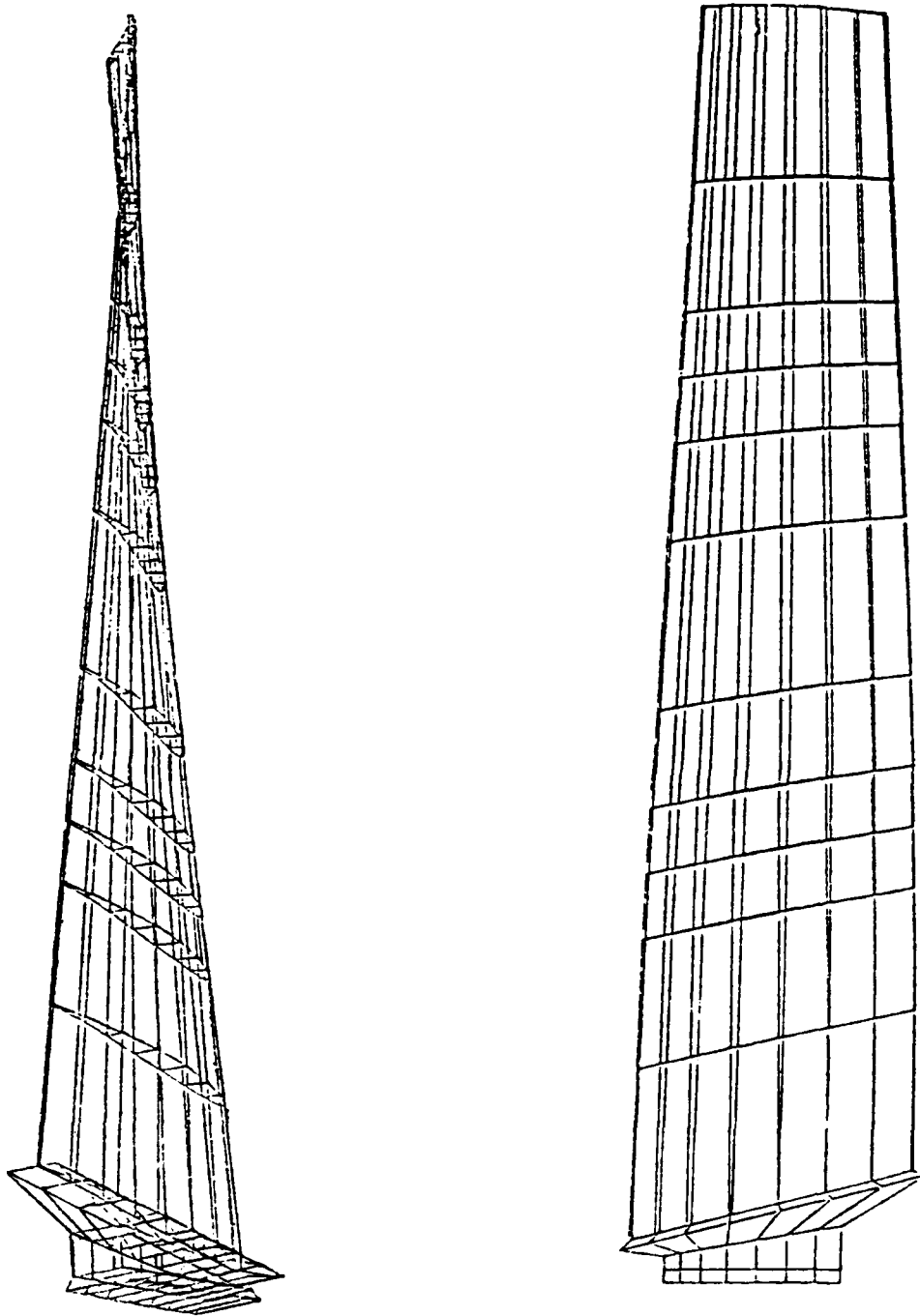


Figure 5. Three-Dimensional, Finite-Element Model of J79 Stainless Steel Compressor Blade.

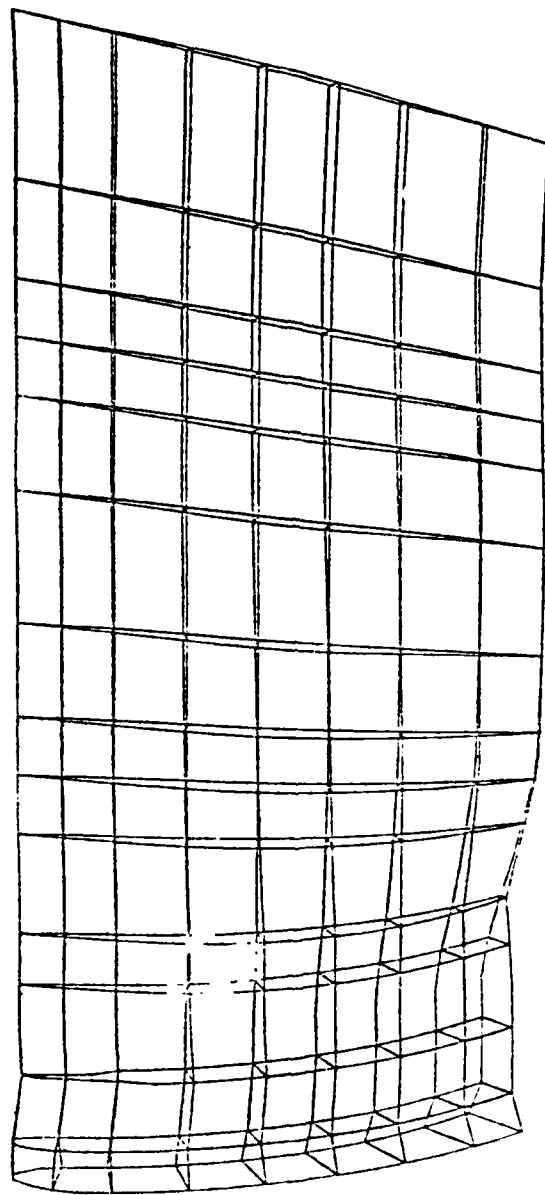


Figure 6. Three-Dimensional, Finite-Element  
Model of APSI B/A1 Fan Blade.

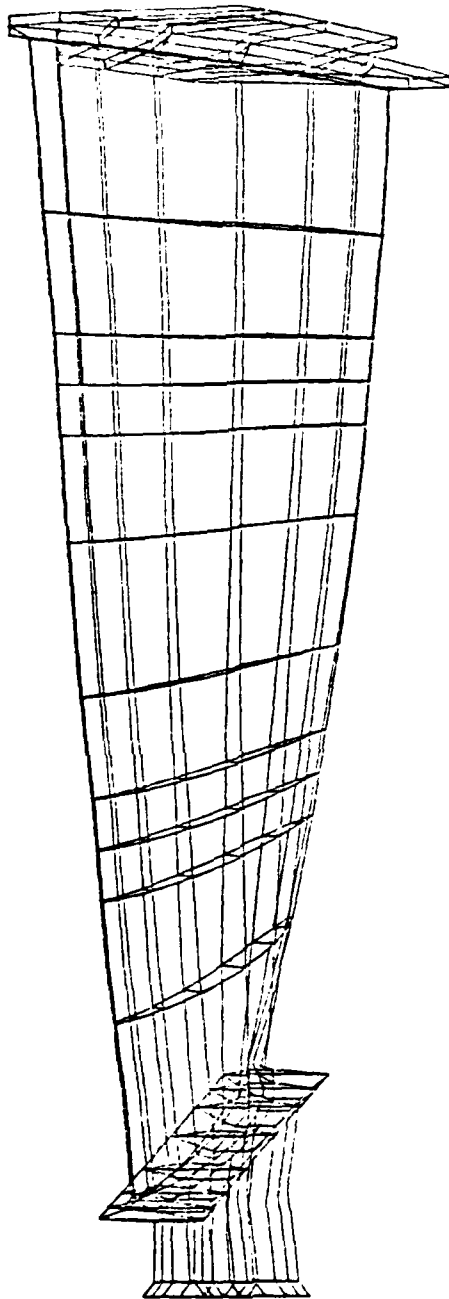


Figure 7. Three-Dimensional, Finite-Element Model of F101 Titanium Fan Blade.

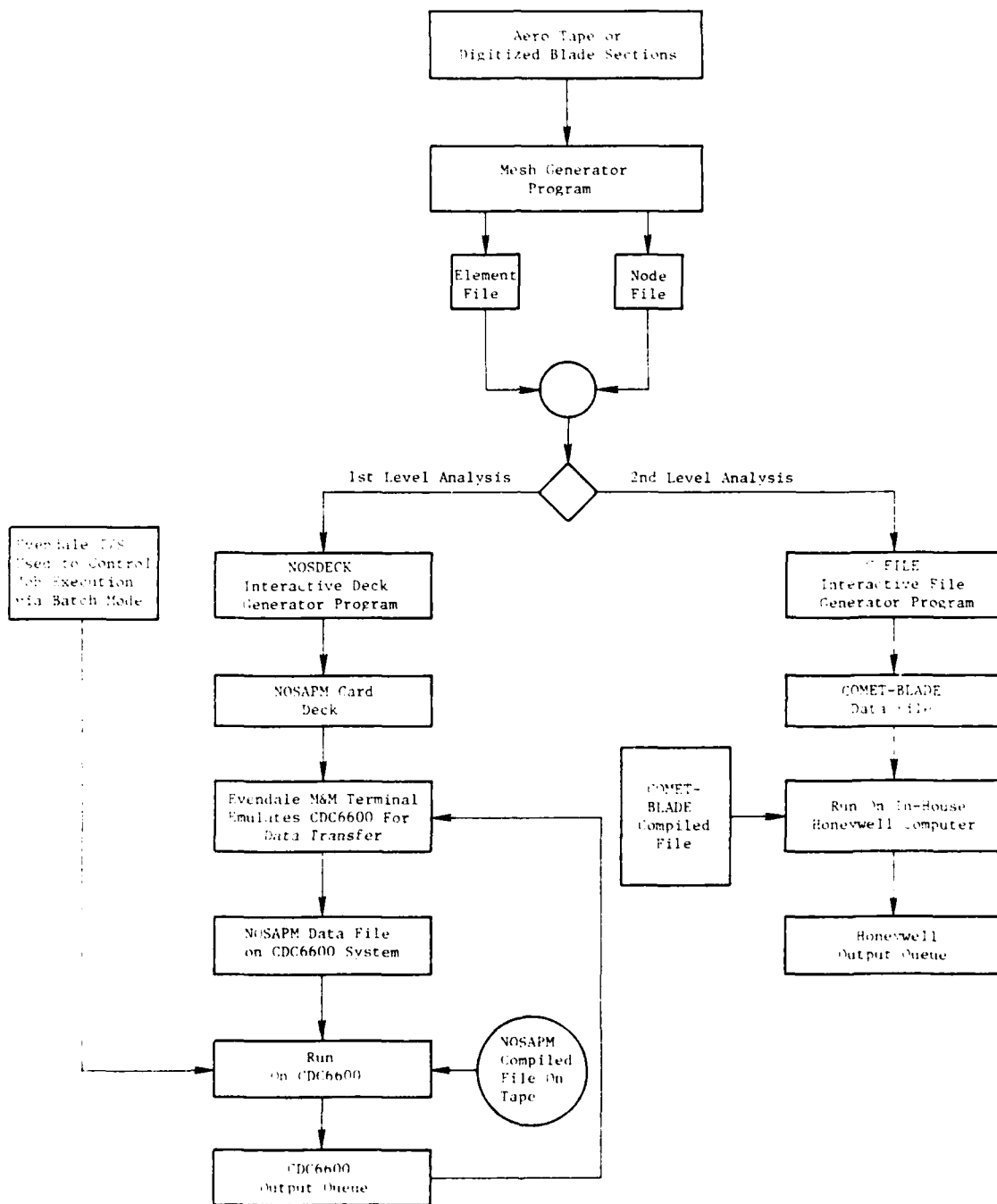


Figure 8. Blade Modeling and Analysis System.

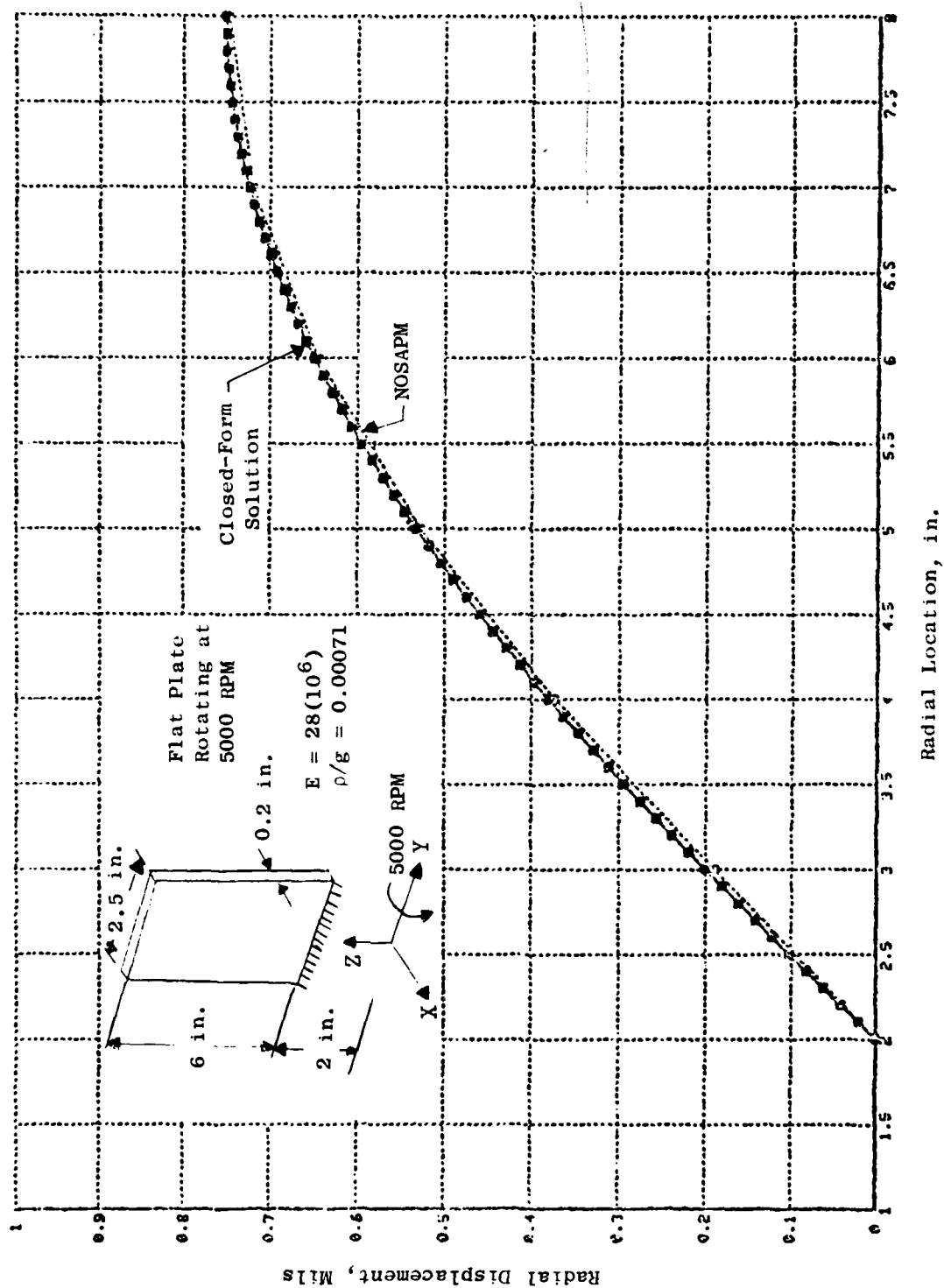


Figure 9. Radial Displacement Due to Centrifugal Loading at 5000 RPM.

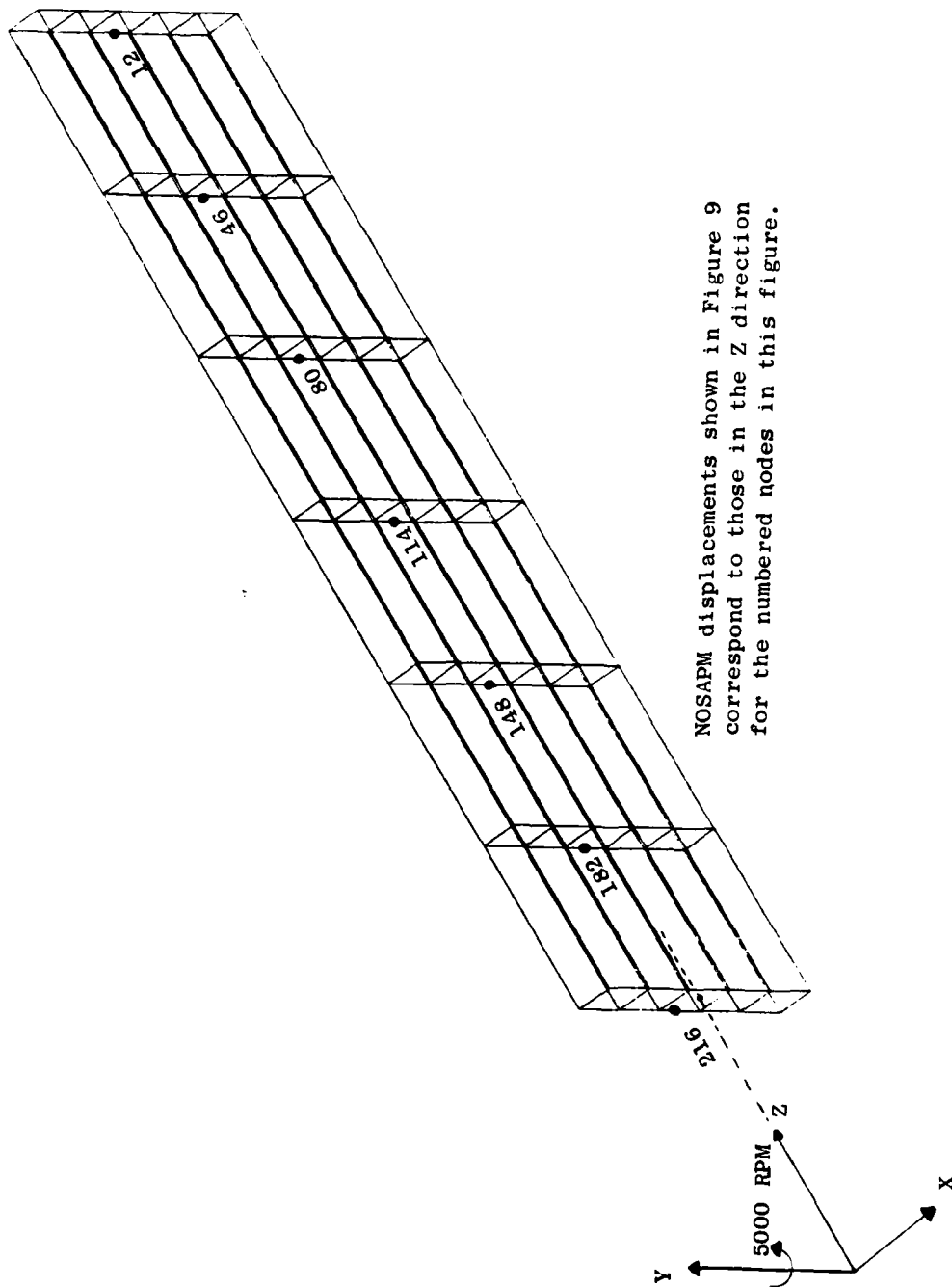


Figure 10. NOSAPM 30-Element Model of Plate Rotating at 5000 RPM.

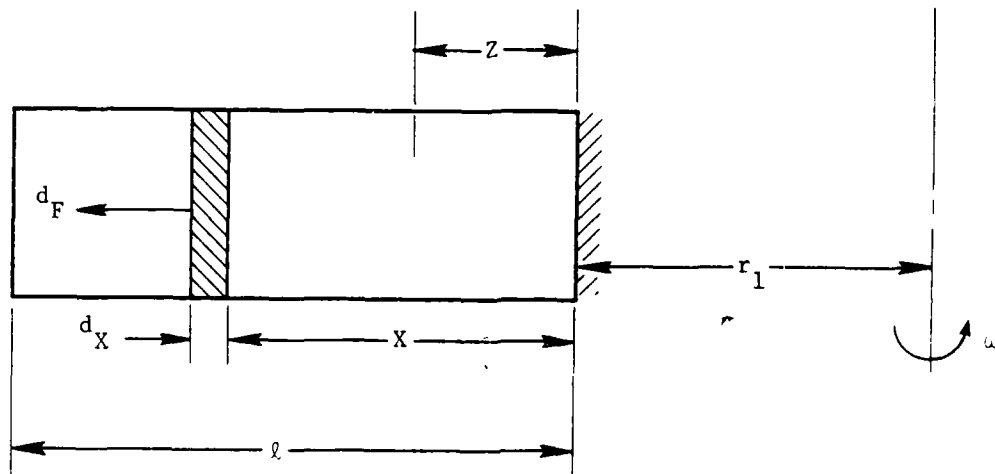


Figure 11. Model Used in Formulation of Closed-Form Solution for Stresses and Displacements from Centrifugal Forces.

Significant progress has been made in the integration of plotting capabilities into the first-level NOSAPM analysis to aid data interpretation. The graphics package MOVIE-BYU is being applied to represent displacement and strain data from NOSAPM. MOVIE-BYU is a 3-D, finite-element, plotting code in general use today; it offers a variety of options. Preprocessing of data output by NOSAPM should provide all the information required for this program. Briefly, these are the capabilities currently available with MOVIE-BYU and the associated preprocessing completed to date:

1. Deformed mesh plots can be obtained at predetermined time intervals.
  - a. These plots can be made with the option of suppressing hidden lines - thus improving the ease of visualization. Figures 12 through 14 illustrate typical results from a normal impact.
  - b. The distortion of the mesh can be scaled to any size the user desires in order to make small displacements visible. Figure 15 illustrates this option. Here, the displacements in Figure 13 are amplified fivefold.
  - c. The user can move his field of view of the structure and "zoom in" to study local behavior.
2. Plots of the effective strain on the surface of the elements can be displayed as contours.
  - a. These plots can be displayed either on a deformed or an undeformed structure.
  - b. With proper supporting equipment, these contours can be translated into color plots. This makes it possible, in turn, to identify surface areas which have surpassed yield strain by coding these areas all to be a particular color - red for example.
3. A method of obtaining surface strains on the deformed structure has been formulated for the preprocessor and is being programmed now.

#### 4.3 SECOND-LEVEL RESPONSE MODEL (COMET-BLADE)

Work on the development of the second-level response model is basically complete. Essentially, the same physical effects are considered in the Level 2 (COMET-BLADE) analysis as in the Level 1, but the element approach is somewhat simplified to gain efficiency. The Level 2 analysis is based on the component-element method<sup>3</sup> and provides an analytical computer capability for predicting gross and local structural response of blades to representative large-body-impact loading stimuli.



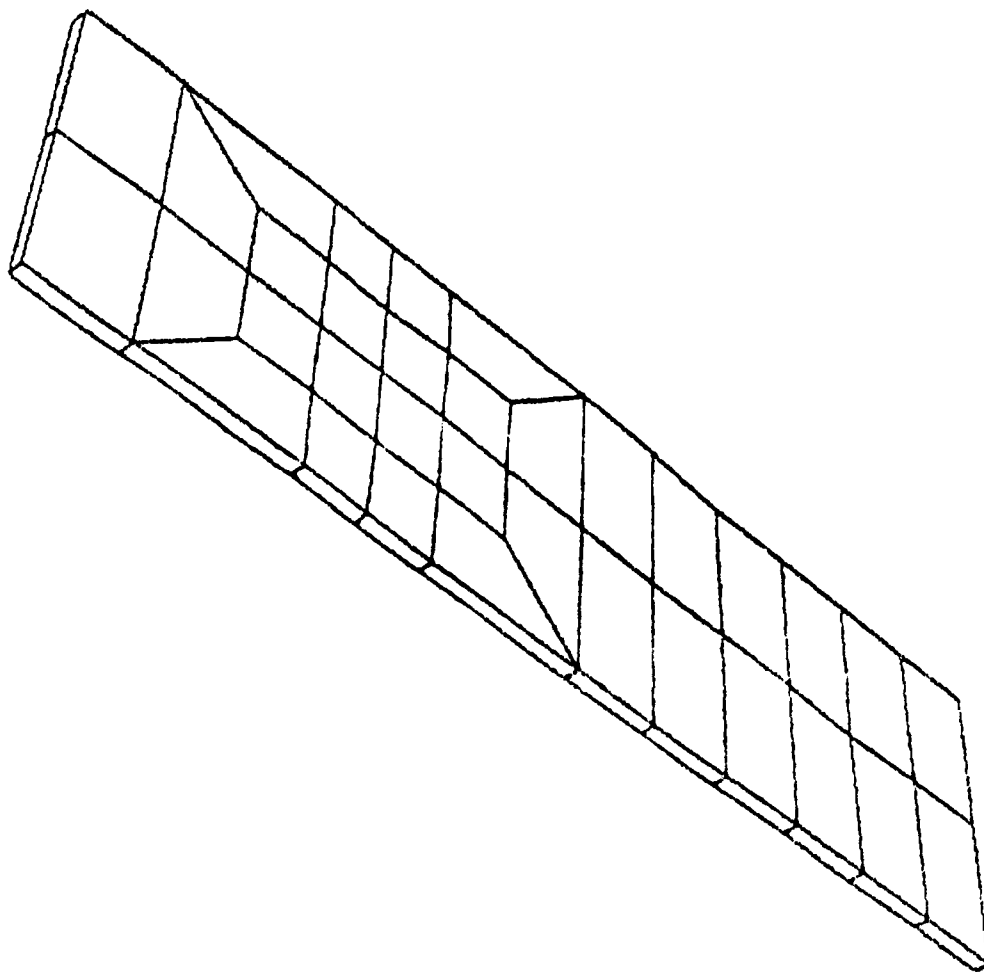


Figure 12. Undeformed Plate.

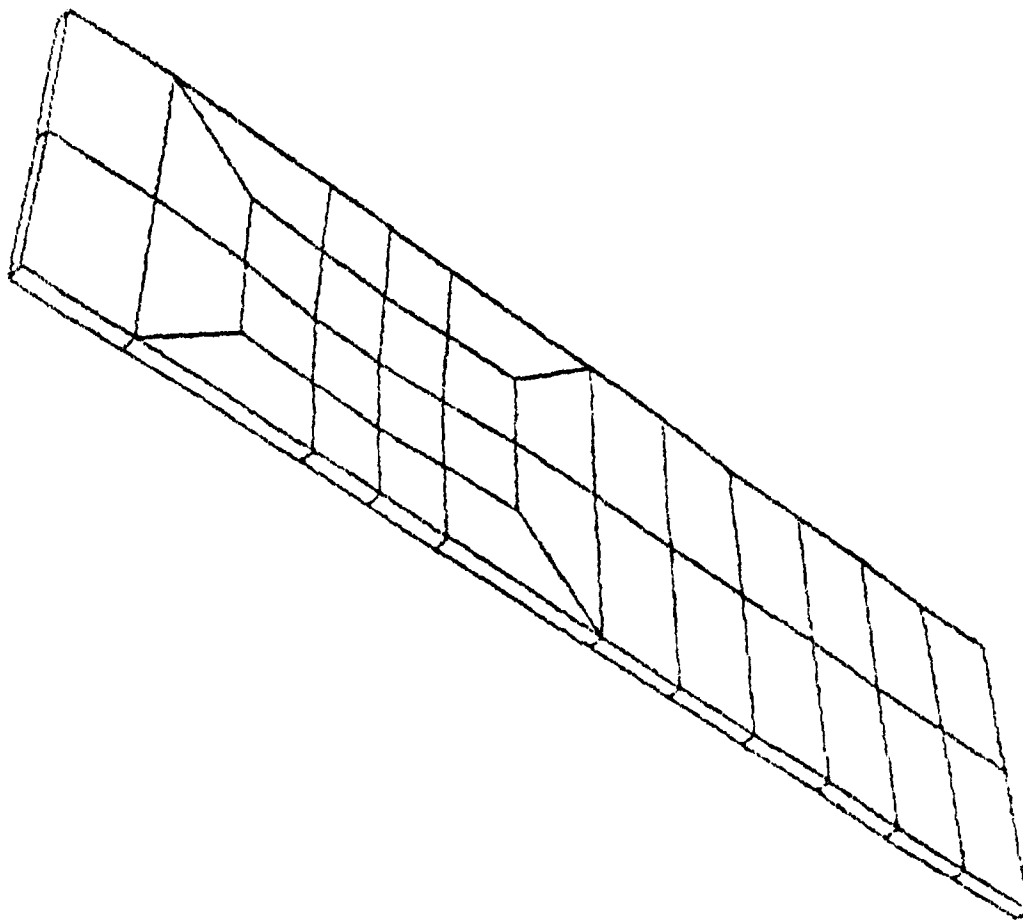


Figure 13. Plate Deformation at 100  $\mu$ sec (Scale Factor = 1).

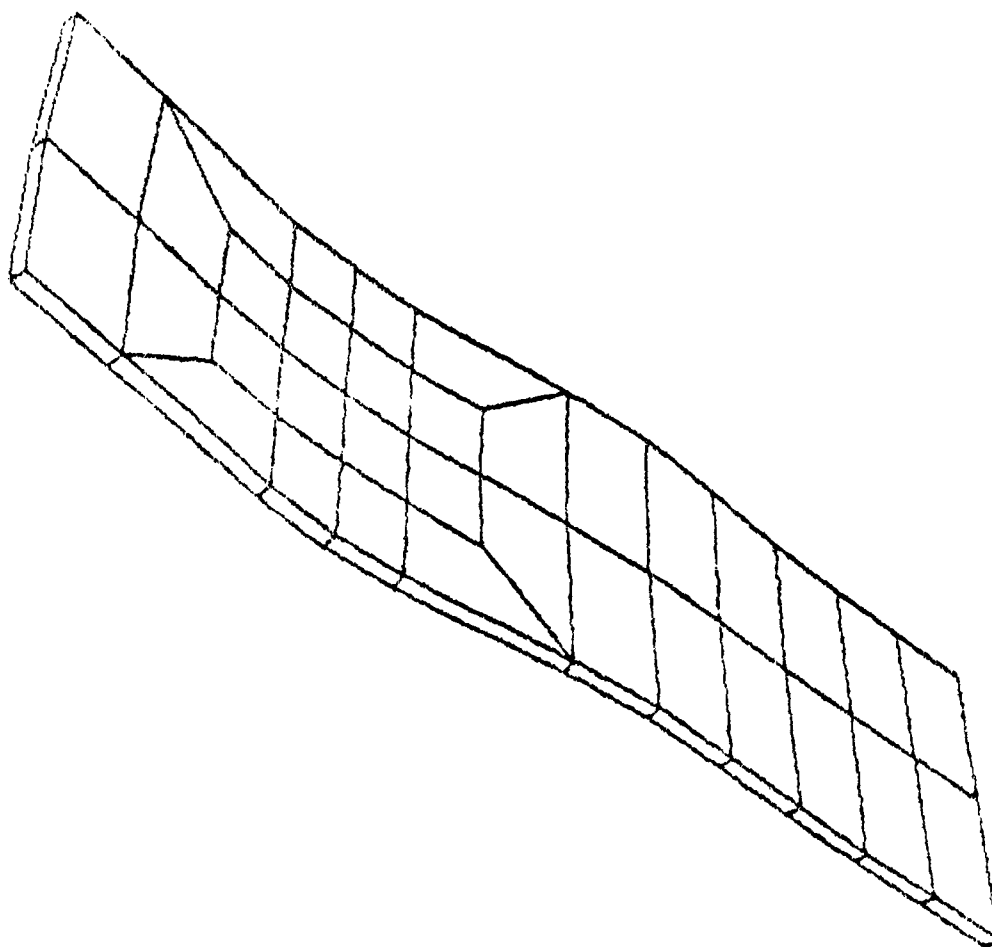


Figure 14. Plate Deformation at 220  $\mu\text{sec}$  (Scale Factor = 1).

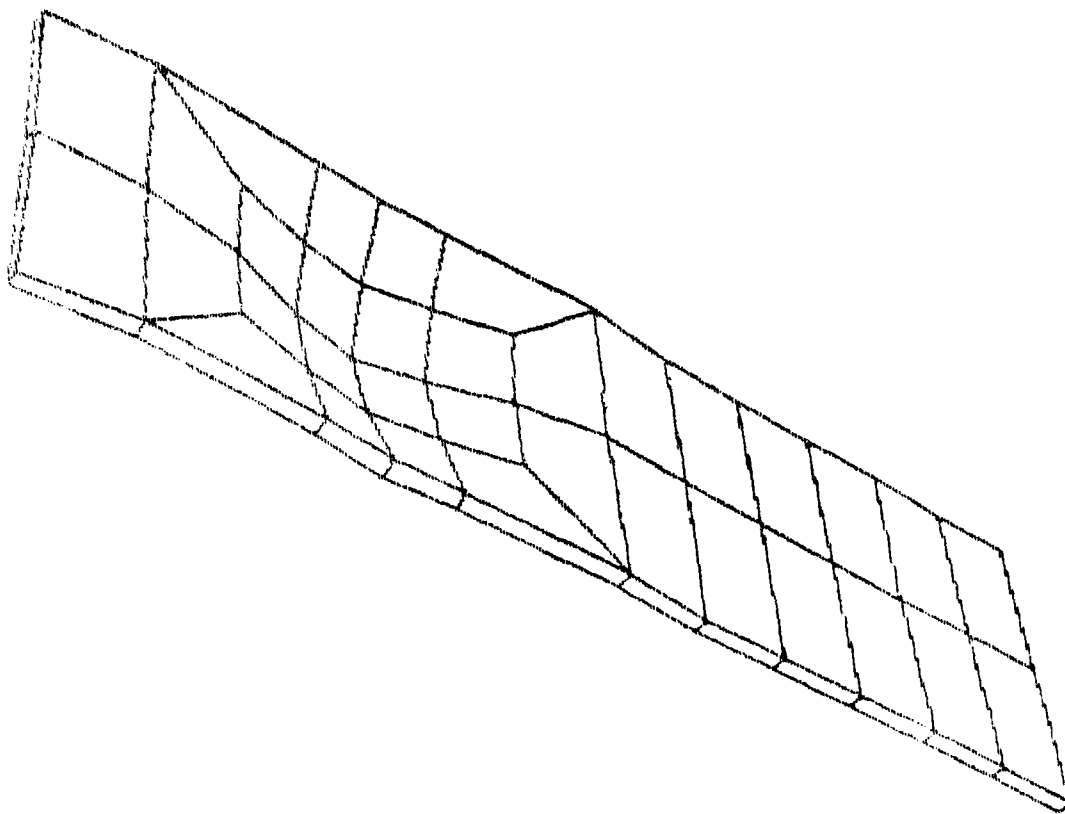


Figure 15. Plate Deformation at 100  $\mu$ sec (Scale Factor = 5).

Bending and membrane effects are modeled with a system of plate elements. These elements couple membrane and bending forces and are similar to those that have been highly successful in modeling both plasticity and hysteresis in the General Electric COMET-PIPE computer program<sup>4</sup>.

The formulation and programming of the plate elements for large deformations, material yielding, and hysteresis effects are complete. These elements have nine nodes and address three cases: (a) an element around a central node for interior regions of the blade, (b) a corner element, and (c) a middle-of-an-edge element. The COMET plate element has nine nodes and is shown in Figure 16; Figure 17 illustrates Level 2 modeling.

Level 2 analysis also includes centrifugal loading effects, in a manner similar to that of the first-level analysis, and provides for the specification of damping that can be proportional to mass, to stiffness, or to a combination of the two. The blade can have twist and camber and can vary in thickness. Boundary conditions, such as restraint of rotation and displacement, can be specified. An elastic, anisotropic option is provided, and spring-damper elements can be used to restrain nodes on the blade.

The blade is modeled by giving the positions of nodes in global coordinates, the blade thickness, the material real-stress versus real-strain curve, the density, the damping, the speed in rpm, and the boundary conditions. The loads can be applied at any node in any direction. Step-by-step numerical integration is used to obtain a solution for the response.

Table 2 is a summary of COMET capabilities.

#### 4.4 INTERFACE WITH THE LOADING MODEL

The interface between the response and loading models will be described in detail in the loading model section (Section 5). A brief description of the interface follows.

Since loading due to a foreign-object impact will depend upon the deformation of the blade, interaction between the structural model and the impactor model will be necessary. This requires the interfacing of the response routines developed by CR&D with the loading model developed by UDRI.

The interface between the first-level response model developed by CR&D and the loading model developed by UDRI has been accomplished. Geometric and dynamic information is periodically transferred from the structural analysis and used to update the impact loads. This need not be done at every structural time step of the transient analysis since large time steps may be suitable without loss of accuracy.

The interface with a loading model developed by CR&D has also been included in the second-level response model. Figure 18 shows the linkup between the loading model subroutine and the executive or main response-model program.

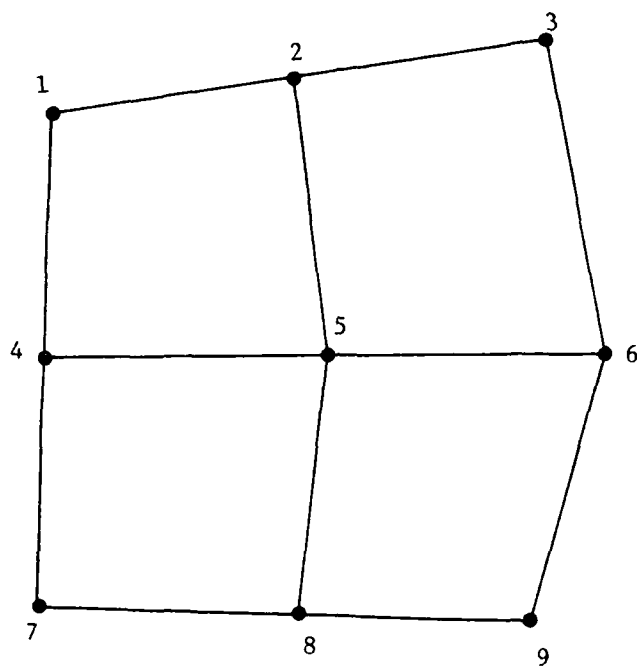


Figure 16. Plate Element Used in  
COMET-BLADE.

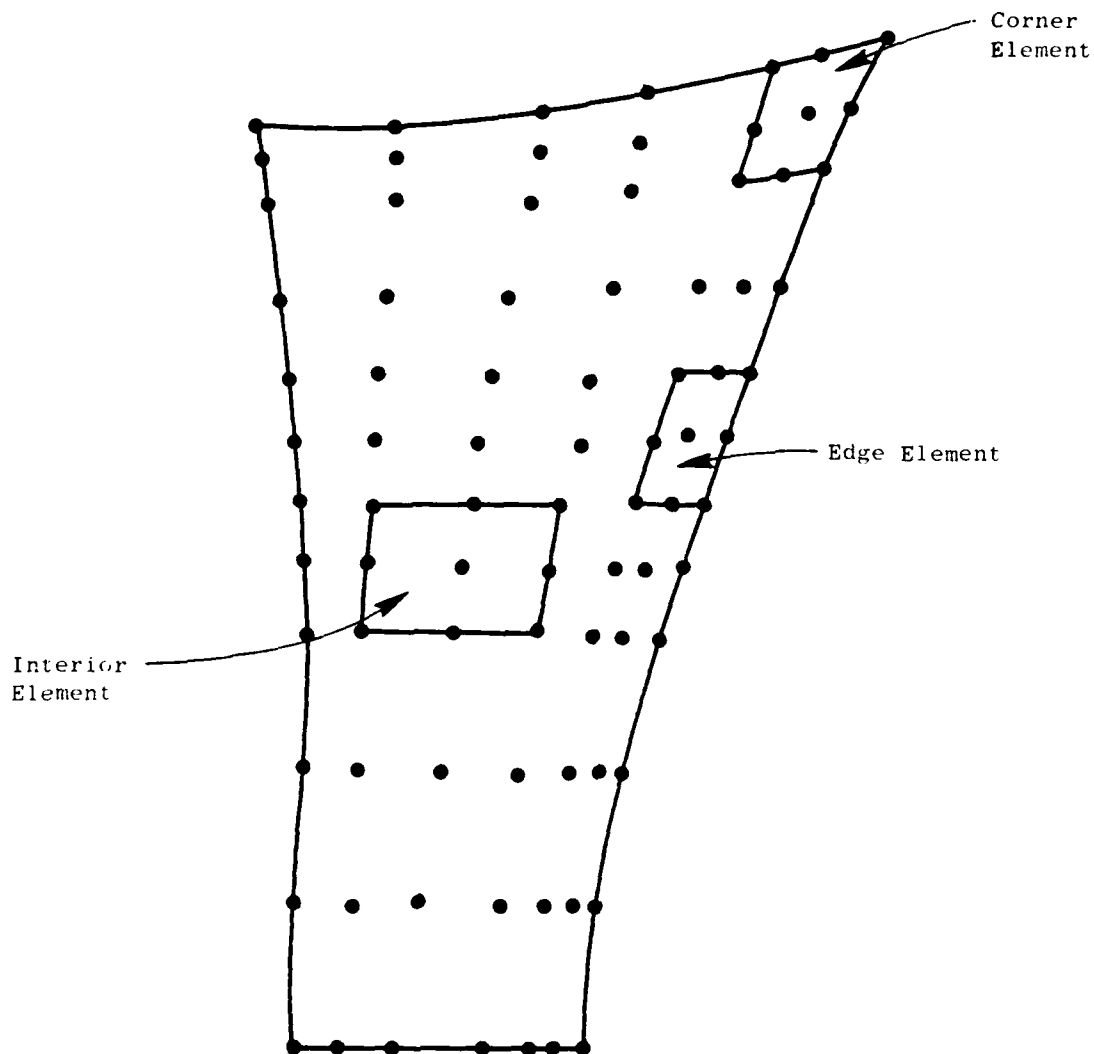


Figure 17. Level 2 Transient-Response Model Formulated from a System of Plate Elements.

Table 2. Second-Level (COMET-BLADE) Analysis  
Based on Component-Element Method.

- The component-element method provides an efficient, nonlinear, analysis capability that does not require the assembly of a global stiffness matrix or the solution of simultaneous equations.
- Simplified element models and an explicit time-integration technique are combined with an approach that treats external (bird loading) and internal restoring forces as forces externally applied to nodal points representing a distributed mass system.
- No iteration is necessary, and the solution for future displacements and strains is obtained by calculating the current values of the nodal accelerations using the current values of all externally applied forces.

$$\ddot{z}^0_i = Q_i/m_i = \text{current acceleration at node point } i$$

$$z^1_i = 2z^0_i - z^{-1}_i + \ddot{z}^0_i (\Delta t)^2 = \text{future displacement}$$

- Centrifugal stiffening is incorporated through a body-force load vector.
- The blade model is constructed in 3-D space from a system of nine-noded plate elements and addresses twist, camber, and thickness variation.
- The plate elements model bending and membrane forces and include the effects of large displacements, material yielding, and hysteresis.



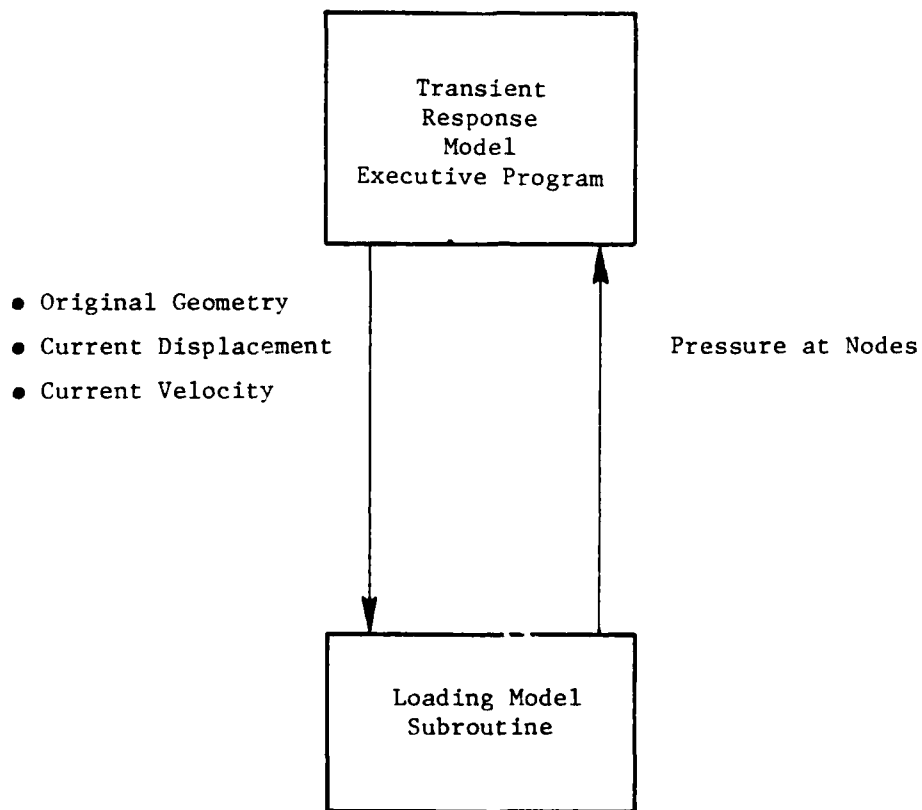


Figure 18. Linkup Between the Loading Model Subroutine and the Executive or Main Response-Model Program.

## 5.0 TASK III - IMPACT LOADING MODEL

### 5.1 INTRODUCTION

The objective of this task is to generate an impact-loading model, for birds and ice, which can be interfaced and used with the transient-response, structural-analysis tools developed in Task II. The effort in this task is divided into four subtasks: (a) simulated bird and ice impact parameters, (b) loading-model sensitivity study, (c) formulation/interfacing of loading model with structural models, and (d) experimental verification of loading model.

### 5.2 SUBTASK A - SIMULATED BIRD AND ICE IMPACT PARAMETERS

The work on this subtask has been completed. A report<sup>6</sup> written by UDRI documenting the effort has been completed and transmitted to the Air Force. This report presents the results obtained from spatially and temporally resolved pressure measurements made during impacts of artificial (gelatin) birds and ice on rigid targets. The data indicate that gelatin behaves the same as real birds during impact and that the analytically predicted pressure distributions obtained with the loading model of Subtask C agree with the measured pressures both for bird impacts and for ice impacts.

### 5.3 SUBTASK B - LOADING MODEL SENSITIVITY STUDY

The work under this subtask has been completed, and a UDRI report on the effort is being reviewed prepratory to transmittal to the Air Force. The purpose of the sensitivity study is to provide specific guidance as to which aspects of the loading-model formulation must be modeled most accurately to properly predict specific aspects of blade response.

The Materially And Geometrically Nonlinear Analysis (MAGNA) finite-element code developed by UDRI was used for the numerical analysis in the sensitivity study. The complex geometry of a real fan blade was avoided in this study by using a flat, cantilever plate. This simplification of real bird-impact conditions in a jet engine permitted a less ambiguous study of the loading details. A flat plate 7.62 cm (3 in.) across the chord by 24.46 cm (9.63 in.) span by 3.81 cm (0.15 in.) thick was chosen as representative of medium-sized jet engine fan blades. The geometry is shown in Figure 19. The material properties of Type 410 stainless steel were employed in the model.

The finite-element model of the cantilever plate is shown in Figure 20. Three-dimensional solid-brick, isoparametric elements with 21 nodes (the 21st node was located at the center of the loaded face) were used to model the plate. The additional node on the loaded face permitted more accurate load definition over the loaded elements. Analyses were performed to account for

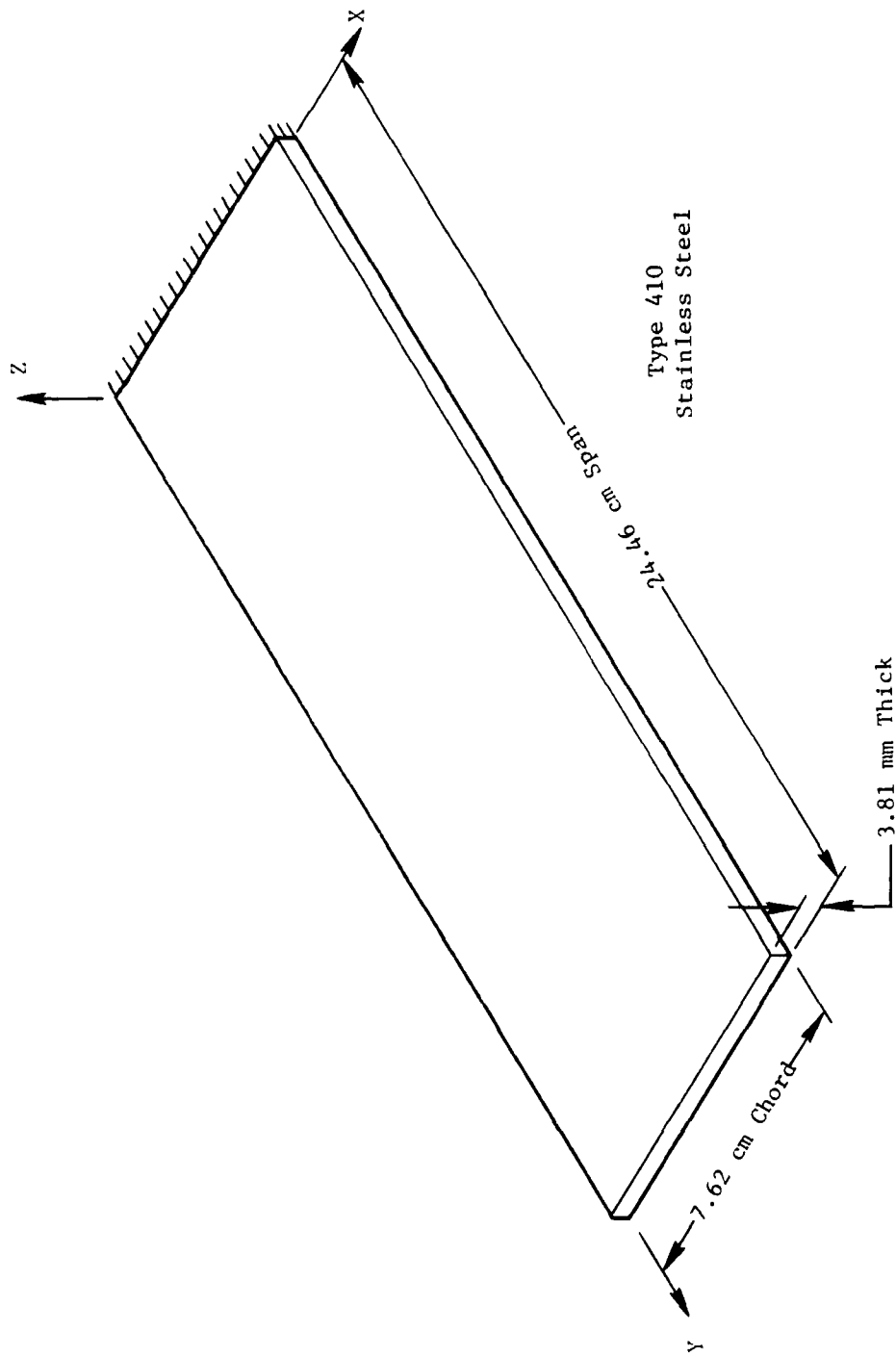


Figure 19. Cantilever Plate Definition Selected for Sensitivity Study.

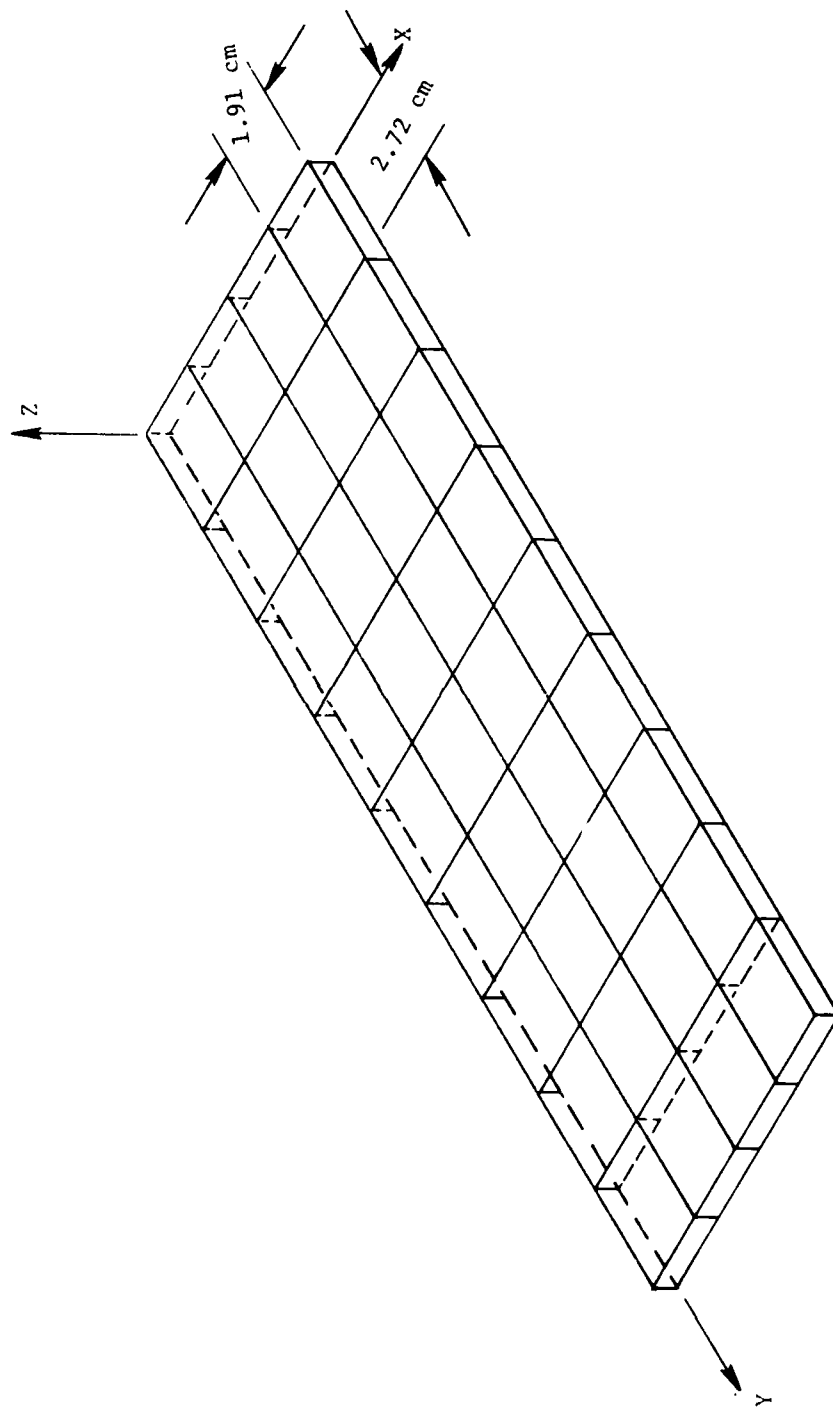


Figure 20. Three-Dimensional-Element Finite Model of Cantilever Plate Used in Sensitivity Study.

geometric and material nonlinearities. The nonlinear dynamic analysis requires considerable computing time for small time steps where a long response calculation is desired. The time step for most analyses was fifteen microseconds. This short time step dictated by solution accuracy made only early time, local response analysis practicable for the large number of analyses performed. The local response (as opposed to overall, late-time deflections) was determined to be more valuable as a measure of sensitivity to loading function details. The overall, maximum, late-time deflection of the cantilever plate was always directly proportional to the projectile momentum at impact. Thus, either bird size or impact velocity, not the details of spatial or temporal load distribution, affected the overall deflection.

#### 5.4 SUBTASK C - FORMULATION/INTERFACING OF LOADING MODELS WITH STRUCTURAL MODELS

##### 5.4.1 Introduction

The loads exerted on a structure during an impact can be characterized in terms of a number of fundamental parameters. The most important of these parameters are the total impulse imparted to the structure, the forces (i.e., the rate of impulse transfer), the pressures (i.e., the spatial distribution of the force), and the time variation of forces and pressures.

Loading models have been developed that address the parameters identified above to the extent required to accurately define bird and ice loading on a target which not only translates and rotates during impact but also deforms locally. The loading models compute the pressure distribution exerted on surfaces during bird and ice impacts (soft-body impacts). The bird and ice impacts are considered as fluid dynamic in nature and are modeled as fluid jets impinging on arbitrarily shaped, three-dimensional, deformable surfaces.

A quasi-steady, potential-flow analysis is applied to the jet-impact problem thereby reducing it to the problem of solving Laplace's equation. The surface-singularity technique is used to solve Laplace's equation.

A subroutine for computing pressure distributions on either rotating or nonrotating turbine engine components has been developed. A model for treating slicing of birds and ice by rotating blades is incorporated into this routine. The loading-model routine is specifically developed to be interfaced with finite-element, structural-analysis, computer programs. Given the instantaneous impacted surface shape and displacement velocity, the loading-model program computes the pressure distribution existing on the impacted surface. The shape of the impact surface is fed to the loading model in the form of finite-element, surface-nodal-point coordinates. From this information, the loading-model computer program constructs a system of quadrilateral elements covering the impacted surface. A uniform distribution of fluid dynamic sources of unknown but determinable strength is applied to each of these quadrilateral elements. The strength of each source distribution is determined from boundary condition considerations. The jet-velocity field and the

pressure distribution are ultimately determined from the velocity field induced by the distribution of sources over the impact surface combined with the jet-velocity field which would exist without the presence of the impacted surface.

#### 5.4.2 The Slicing Model

Because the forces required to slice a soft body are small compared to the forces required to decelerate the body, the slicing forces can be ignored. Therefore, the slicing-model development reduces to simply a geometric problem of determining the dimensions and weight of a slice. For birds and ice spheres (such as hail), the velocity of the ingested object is small compared to the velocity of the aircraft; thus, the object velocity can be ignored. For slab ice, such as ice breaking loose from an engine nacelle, the velocity of the slab relative to the nacelle is not well-defined, but we can expect this velocity to be small in comparison to the aircraft velocity.

##### 5.4.2.1 Slicing Model Development for Birds

The bird is idealized as a right circular cylinder with a length-to-diameter ratio of 2, and the velocity of the bird relative to the aircraft is taken to be equal and opposite to the aircraft velocity. In the following analysis, a coordinate system attached to the blade is used. The bird/blade interaction geometry in such a coordinate system is shown in Figure 21. The following information is assumed to be known (supplied as input data to the loading model subroutine):

$N$  - number of blades per stage

$n$  - blade rotational speed (rpm)

$Z_i$  - distance from the rotational axis of the rotor to the point on the blade at which the center of the impact occurs

$\delta$  - blade orientation angle (defined as the angle  $\delta$  in Figure 21)

$V_b$  - axial velocity of the bird

$W_b$  - bird weight

$\rho_b$  - bird density (0.91 g/cm<sup>3</sup> or 0.033047 lbm/in.<sup>3</sup>)

An infinite number of slice shapes are possible for a given set of these input parameters; the shape depends on the orientation of the bird relative to the blade and on the span location on the blade at which the impact occurs. Since worst-case slice shapes are desired (i.e., slice shapes having the largest possible slice mass), the orientation of the axis of the bird and the center of impact of a slice are chosen to produce a slice having the largest possible mass. The largest slice mass occurs when the axis of the

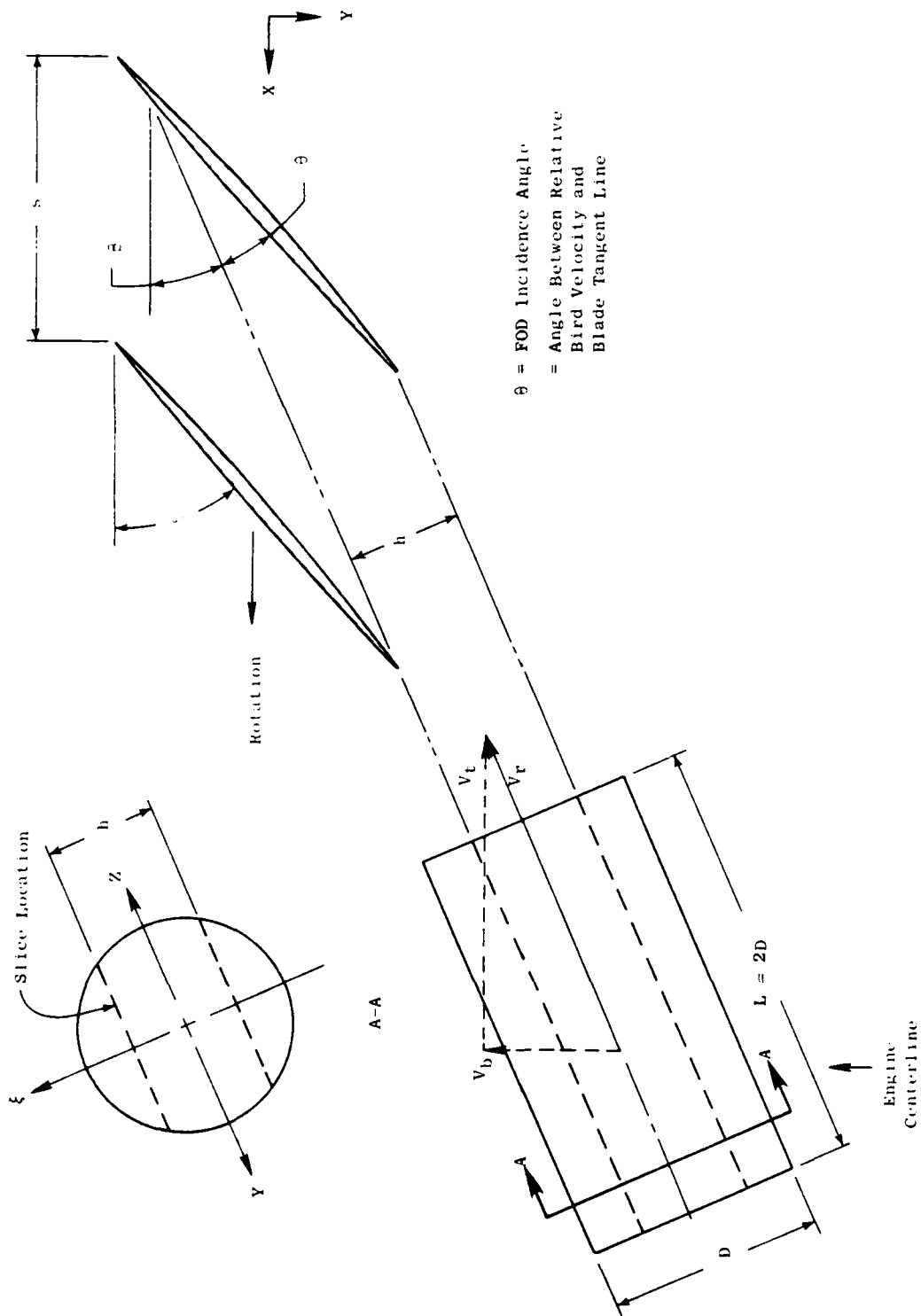


Figure 21. Bird/Blade Interaction Geometry.

slice is coincident with the axis of the right circular cylinder. The slice geometry depicted in Figure 21 corresponds to this worst-case situation.

With the bird idealized as a right circular cylinder with  $L = 2D$ , the diameter of the bird is determined from the bird weight and density as:

$$D = (2W_b / \pi \rho_b)^{1/3} \quad (8)$$

The tangential velocity of the bird,  $V_t$ , is computed at the impact radius  $Z_i$  and is given by:

$$V_t = 2\pi n Z_i / 60 \quad (9)$$

And the magnitude of the velocity of the bird relative to the blade,  $V_r$ , is given by:

$$V_r = \sqrt{(V_b^2 + V_t^2)} \quad (10)$$

The direction of  $V_r$  relative to the plane of rotation of the blade at the impact location,  $Z_i$ , is:

$$\beta = \sin^{-1} (V_b / V_r) \quad (11)$$

$V_r$  is assumed to have no component in the radial direction. The impact angle, defined as  $\theta$  in Figure 21, is:

$$\theta = \delta - \beta \quad (12)$$

The blade spacing (defined at  $Z_i$  and denoted by  $S$  in Figure 21) is given by:

$$S = 2\pi Z_i / N \quad (13)$$

The bird slice width,  $h$ , is then given by:

$$h = S \sin \beta = (2\pi Z_i / N) (V_b / V_r) \quad (14)$$

Referring to Figure 21, we find that the bird-slice weight is given by:

$$W_{sb} = \rho_b L \int_{-h/2}^{+h/2} 2\sqrt{(D/2)^2 - \xi^2} d\xi \quad (15)$$

$$W_{sb} = 2\rho_b D \left[ h\sqrt{(D/2)^2 - (h/2)^2} + (D^2/2) \sin^{-1} (h/D) \right] \quad (16)$$



The use of Equations 9 and 10 in Equation 14 shows that the bird-slice width at any impact radius depends only on the blade parameters ( $N$  and  $n$ ) and the aircraft speed. The bird-slice weight at any impact radius depends, in addition to the above three parameters, only on the density and total weight of the bird.

If  $h/\sin \theta$  is greater than the chord of the blade at  $Z_i$ , then not all of the slice will impact on the blade.

#### 5.4.2.2 Slicing Model for Ice Spheres

For ice spheres (such as hail), the axial velocity of the sphere relative to the blade is taken to be equal and opposite to the aircraft velocity, just as for birds. The expressions for slice-width, impingement angle, and  $V_r$  are the same as for birds. The slice weight,  $W_{s_{is}}$ , is given by:

$$W_{s_{is}} = 2\pi\rho_i \int_0^{h/2} [(D/2)^2 - \xi^2] d\xi \quad (17)$$

or:

$$W_{s_{is}} = 2\pi\rho_i [(D/2)^2 (h/2) - (h/2)^3/3] \quad (18)$$

where  $h/2 \leq D/2$ , and  $\rho_i$  is the ice density. For ice spheres it is presumed that the diameter of the sphere is a specified quantity along with the ice density.

#### 5.4.2.3 Slicing Model for Ice Slab

For slabs of ice, the operator-specified information is presumed to be the length of the slab ( $L$ ), the thickness of the slab ( $\Delta Z$ ) (i.e., how much of the blade span is to be exposed to the slab), and the axial velocity of the slab relative to the nacelle (this replaces  $V_b$  in Equations 10, 11, and 14). The slice width,  $h$ , is again given by Equation 14 with  $V_b$  replaced by the axial velocity of the slab relative to the nacelle. The slice mass is then given by

$$W_{s_s} = \rho_i(h)(\Delta Z)L \quad (19)$$

#### 5.4.3 Bird-Slice Geometry Parametric Study Results

Using the equations developed in Section 5.4.2.1, the bird-slice parameters were computed both for starling impacts (3-ounce birds) and for big-bird impacts (1.5-pound birds). Three different blade configurations (J79, APSI, and F101) were considered, and typical values of rotor speed, number of blades per stage, blade orientation angle, and impact radius were used. The input parameters and the computed quantities are shown for the two cases of bird

weights in Tables 3 and 4. The primary observation from this parametric study is that bird (and ice sphere) impacts are highly oblique.

#### 5.4.4 Fluid Flow Model of Impact

It has been demonstrated in Reference 6 that for birds having an L/D of 2 or greater the largest contributing factor in the total impulse of a bird impacting a target is the steady-flow phase of the impact. Thus, in the current version of the loading model, the pressure distribution is based on a steady-flow analysis. This method of analysis is extended into a dynamic analysis, for deforming targets, by treating the flow at any instant of time as a quasi-steady flow using the instantaneous relative velocity between the bird slice and the deforming target as the characteristic velocity. The instantaneous shape of the target is used to define the surface on which impact occurs.

In the analysis of the impact process, the strength of the projectile material is considered to be negligible. This assumption is quite reasonable for the typical projectile and target materials of interest.

We assume that, at least as a first approximation, the fluid flow may be treated as incompressible. This is a reasonable assumption because the measured steady-state pressures are quite small in comparison to the pressures required to produce significant density changes in birds or ice.

By virtue of the incompressible flow and steady flow assumptions and the negligible strength of the projectile material, the problem of predicting soft-body impact loads is amenable to analysis within the following real constraints. The computing time required to obtain a reasonable solution must be small in comparison to the computing time required to compute the structural response, and the computer storage requirement for the loading model must be small in comparison to the structural-response-analysis computer program storage requirements.

Three-dimensional potential flow theory was chosen as the most appropriate method for modeling the impact process. Our initial work in using this approach was quite successful<sup>6</sup>. In that work, we used the method of surface singularities to determine the velocity and pressure fields caused by circular jets impacting at oblique angles on flat, rigid plates. This same technique was used to develop the loading model. The method developed earlier was generalized to include the impact-surface curvature and deformation velocity, an arbitrary cross-sectional area of the impacting flow, and a method for generating planar quadrilateral surface elements from given finite-element, surface-nodal-point locations.

Table 3. Blade Calculation Input Data Sheet for 3-Oz Bird.

Parameter	J79		AP-1		F101
Motor Speed, n (rpm)	7460		17500		7555
Number of Blades, N (-)	21		28		50
Tip Radius, R <sub>t</sub> (in.)	14.65		11.00		22.18
Root Radius, R <sub>r</sub> (in.)	5.21		4.95		11.71
Span Location (%)	30	70	30	70	30
Radius, r <sub>i</sub> (in.)	8.04	11.82	6.76	9.19	14.85
Orientation Angle, $\delta$ (°)	72.0	51.0	49.8	27.0	52.5
Chord Length, C (in.)	2.23	2.23	2.90	3.06	3.30
<u>Calculated Values</u>					
Blade Tangential Velocity, W <sub>θ</sub> (ft/sec)	523	769	1032	1403	979
Bird Axial Velocity, V <sub>b</sub> (ft/sec)	200	200	200	200	200
Relative Velocity, V <sub>r</sub> (ft/sec)	560	795	1051	1417	999
Bird Weight, W <sub>b</sub> (lb)	0.188	0.188	0.188	0.188	0.188
Bird Slice Width, h (in.)	0.36	0.89	0.29	0.29	0.37
Bird Slice Weight, W <sub>s</sub> (lb)	0.126	0.129	0.045	0.045	0.057
Bird-Blade Incidence Angle, $\theta$ (°)	51.1	36.4	38.8	18.9	41.0
Angle $\beta$ (°)	20.9	14.6	11.0	8.1	11.5
Bird Diameter, D (in.)	1.53	1.53	1.53	1.53	1.53

Table 4. Blade Calculation Input Data Sheet for 1.5-lb Bird.

Parameter	J79			APSI			F101		
Rotor Speed, n (rpm)	7460			17500			7555		
Number of Blades, N (-)	21			28			50		
Tip Radius, $R_t$ (in.)	14.65			11.00			22.18		
Root Radius, $R_R$ (in.)	5.21			4.95			11.71		
Span Location (%)	30	70	70	30	70	70	30	70	70
Radius, $r_i$ (in.)	8.04	11.82		6.76	9.19	14.85	14.85	19.04	
Orientation Angle, $\delta$ (°)	72.0	51.0		49.8	27.0	52.5	52.5	33.5	
Chord Length, C (in.)	2.23	2.23		2.90	3.06	3.30	3.30	3.70	
<u>Calculated Values</u>									
Blade Tangential Velocity, $W_\theta$ (ft/sec)	523	769		1032	1403	979	979	1255	
Bird Axial Velocity, $V_b$ (ft/sec)	200	200		200	200	200	200	200	
Relative Velocity, $V_r$ (ft/sec)	560	795		1051	1417	999	999	1270	
Bird Weight, $W_b$ (lb)	1.50	1.50		1.50	1.50	1.50	1.50	1.50	
Bird Slice Width, h (in.)	0.86	0.89		0.29	0.29	0.37	0.37	0.38	
Bird Slice Weight, $W_s$ (lb)	0.53	0.55		0.18	0.18	0.23	0.23	0.24	
Bird-Blade Incidence Angle, $\theta$ (°)	51.1	36.4		38.8	18.9	41.0	41.0	24.4	
Angle $\beta$ (°)	20.9	14.6		11.0	8.1	11.5	11.5	9.1	
Bird Diameter, r (in.)	3.07	3.07		3.07	3.07	3.07	3.07	3.07	

#### 5.4.4.1 Surface Singularity Method - Superposition of Onset Flow and Surface Source Distribution

The impacting bird slice is idealized as an onset flow, of velocity  $V_r$ , uniformly distributed over the cross-sectional area of the slice. The fluid velocity at a point is expressed as the negative gradient of a potential function that: satisfies Laplace's equation in the region exterior to the blade, has a zero normal derivative on the blade surface, and approaches the proper uniform stream potential function. The flow is viewed as an onset flow potential and disturbance potential due to the blade. The disturbance potential satisfies Laplace's equation in the exterior and the appropriate normal derivative condition on the surface and vanishes at infinity. From potential theory, it can be shown that this potential may be evaluated in terms of a surface source density distribution with which the blade surface may be considered to be covered. The incorporation of the normal derivative condition on the surface produces a source density distribution, over the surface, described by a two-dimensional Fredholm integral equation of the second kind. Once this equation is solved for the source density distribution, first the disturbance potential and then the disturbance flow velocities may be obtained.

#### 5.4.4.2 The Body Surface Approximation

The body surface must be suitably approximated in the numerical solution of the Fredholm integral equation for the surface source density distribution. The body surface is approximated by a large number of small, plane elements formed from the original points defining the body surface. The calculations employ plane, quadrilateral elements; the source density is assumed constant over each of these elements. With this assumption, the problem of determining the continuous function for the source density reduces to one of determining a finite number of values - one for each of the planar elements.

#### 5.4.4.3 Solution Procedure

This section presents a brief description of the method of solution.

As a first step, it is necessary to input a set of points, in three-dimensional space, describing the body surface. This input should be chosen to provide the best representation of the body with the fewest possible points. Four of these inputs are employed to generate one plane, quadrilateral, source element of the body surface.

Once the values of the surface source density have been determined, the velocity components at each null point are calculated, and the appropriate components of the onset flow are added. The resultant velocities and pressures are easily computed from the velocity components.

#### 5.4.5 Structure of the Loading Model and Interface With The First-Level Response Model

We have incorporated in our analysis a procedure for finite-difference numerical computation of the potential flow about arbitrary, three-dimensional bodies; this procedure has certain features that render it compatible with the first-level, finite-element, structural-response-analysis code. Specifically, the nodal points in the finite-element program become approximate locations of the null point (defined as the point where the quadrilateral element induces no velocity in its own plane) around which the plane, quadrilateral elements are constructed in the potential-flow analysis. This greatly facilitates the coupling of the finite-difference loading model and the finite-element structural code.

In loading used for any arbitrarily shaped impact surface, the impact area is divided into small, flat elements; a uniform distribution of sources is assumed to cover each area. At the beginning of impact, an initial pressure distribution is computed for the undeformed blade. During an impact in which local deformation takes place, the deformed shape of the impact zone is calculated in the dynamic structural-response analysis. After significant deformation has occurred, the geometry of the impact zone is provided to the loading model. The loading model is then used to calculate a new pressure distribution. As the structural-analysis calculation proceeds, the local shape, the location, and the velocity of the impact area are updated and passed to the loading model at appropriate time intervals. The loading model, in turn, provides updated pressure-distribution information for the structural-response computation. The loading model is fully interactive with the structural-response calculation. The duration of the impact is computed by keeping track of how much slice has been consumed during each time interval.

A summary of the interface between the loading and response models follows:

- The response model provides displacements and velocities at the surface nodes of the structural elements in the impact region. These structural elements are then subdivided into smaller elements corresponding to the finer grid of the loading model as specified by user input, and the structural-element shape functions are then used to compute the displacements and velocities at the nodes of the smaller elements. These displacements and velocities are provided to the loading model at specified time steps.
- The slice-size calculations are based on user input and are performed by the response program. The impactors available to the user include the following:
  - Bird of any weight represented by a right circular cylinder having  $L/D$  ratio equal to 2.0.
  - Ice ball of any diameter.

- Slab ice of any thickness and length.

User-provided information (in addition to the geometry and material properties of the finite-element response model) will consist of the velocity of the aircraft, the rotational velocity of the fan or compressor, the number of blades in the stage, the spanwise location of the impact, and the specification of the impactor.

- The loading model provides the pressures at the nodes of the smaller elements, and the structural-element shape functions are then used to calculate the pressures at the nodal points of the structural elements. These pressures are then converted to equivalent nodal forces through a consistent force formation.
- A flag is returned by the loads model when the impactor has been consumed (i.e., when it has traveled its own length). When this occurs the response model will no longer call the loading model subroutine, and the nodal pressures are set to zero.

The loading model is capable of detailed interaction with the structural-response model and of dealing with target translation, rotation, and local deformation. The load/response coupling modeled in this formulation should be capable of accurately predicting both overall target response and local deformation.

The principal limitation of the loading model is that it does not include transient effects. The most significant of these is the shock effect; however, the porosity present in birds appreciably reduces the shock stresses without significantly affecting steady flow pressures. In addition, impact obliquity reduces the relative importance of shock stresses. Therefore, it is not obvious that neglect of the shock aspects of bird impact on blades is a significant deficiency. Another transient aspect of bird impacts is the variation of slice cross section at the target surface during impact. This variation results mainly in a time variation of the impact area. If the flow remains quasi-steady during these variations (i.e., the "velocity" of the variation is low with respect to local sound speed - probably a good assumption), then the loading model can be modified to describe these effects. The size and geometry of the "jet" that flows onto the target surface must be updated incrementally to describe the variation with time of the impact area.

#### 5.4.6 Structure of the Loading Model and Interface With The Second-Level Response Model

A simplified, interactive, load model was developed by CR&D for the second-level response code. This model is less elaborate than the potential-flow approach incorporated by UDRI and is based in part upon experimental impact information available in Reference 6. However, it does offer several advantages; as a result, it has been incorporated in the Level 2 structural-response model. Among these advantages, perhaps the most important is simplicity. The pressure calculations in this model require only the geometry and the velocity at the point for which pressure is to be calculated; as a

result, no linear-equation solution is required. This reduces the time for calculation. In addition, the experimental basis for the model allows for the inclusion of the initial pressure shock during impact.

The general operation of this load model is quite simple. The bird and the impact geometry are exactly the same as those defined and applied in UDRI's model. The pressures are calculated at the structural-node points. Each time the loads are calculated, the program determines which nodes of the structure are within the impact zone. It also identifies the location of the trailing end of the impacting bird with respect to the current blade location. Pressure loading is terminated when the end of the bird-slice passes the deformed location of the blade. During the impact event, the pressures at nodes which fall within the impact zone are calculated as follows.

With knowledge of the structural geometry and nodal velocities, as well as the bird-slice velocity, a relative velocity between bird and structure normal to the plane of the blade is defined. This velocity is then used to calculate an average pressure based upon the simple impulse-momentum considerations shown in Figure 22. This pressure reflects a dependence upon the structural deformation occurring during impact.

Use is now made of two experimental observations. The first observation is made with respect to Figure 14 in Reference 6. This figure reflects the observation that the loading on the blade rises to a peak of twice the average pressure at approximately 20% of total impact time before decreasing to zero. Figure 23 shows the temporal variation of pressure that is nondimensionalized with respect to the average, steady-state, dynamic pressure. These experimental data are incorporated in the loading model as a time-scaling factor: FCTRT.

The second observation is made with respect to Figure 34 of Reference 6. For oblique impacts, this information indicates that the pressure is maximum at the leading edge and approximately equal to twice the average, steady-state, dynamic pressure. The pressure decreases to zero at a given distance from the leading edge. Refer to Figure 24 for a description of the spatial variation of pressure. This behavior is incorporated in the model through the use of a second scaling factor, FCTRG, which is also applied to the average dynamic pressure. Thus, the pressure applied at any given node of the structure is:

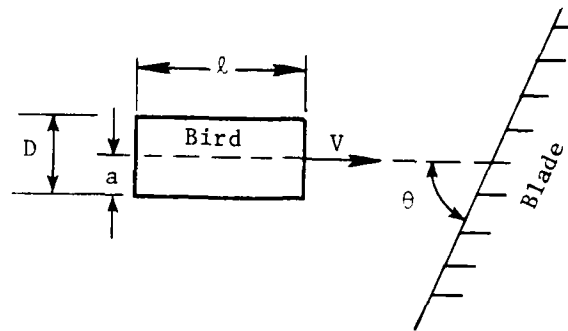
$$P = (FCTRG)(FCTRT)(\rho V^2/g) \sin^2 \theta \quad (20)$$

The calculation is simple, interactive, and representative of the experimental results reported in Reference 6.

#### 5.4.7 Summary

Loading models have been developed for soft-body impacts on structures that respond to the impact in a very general manner. The loading models were developed from a fluid-dynamic description of a soft body impacting (flowing onto) a structure. The structure can translate, rotate, and deform locally





Impulse.  $I = F\Delta t = M\Delta V = \text{Momentum Transfer}$

$$F = I/\Delta t = M\Delta V/\Delta t$$

$$F = MV \sin \theta (V/l)$$

$$F = p A/\sin \theta$$

$$p = (\rho/g)V^2 \sin^2 \theta = \text{Average Steady-State Dynamic Pressure}$$

$$\rho = \text{Bird Density} = 0.033047 \text{ lbm/in.}^3$$

$$V \sin \theta = \text{Normal Velocity of Bird Relative to Blade}$$

Figure 22. Impulse-Momentum Principle; Bird is Treated as a Fluid Body.

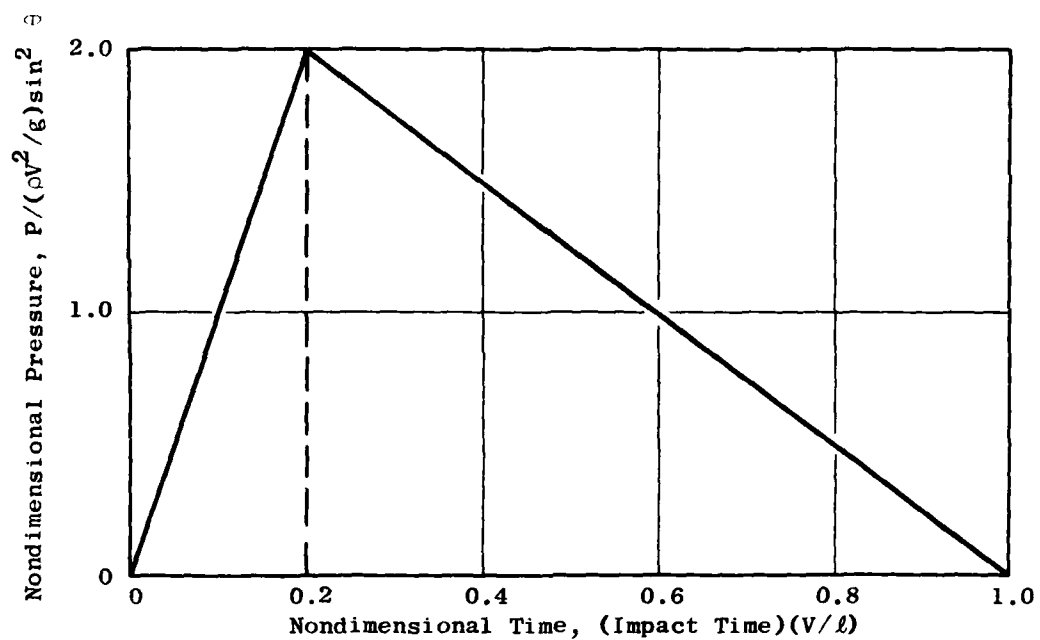


Figure 23. Generalized Bird-Impact Pressure/Time Profile Based on Experimental Results.

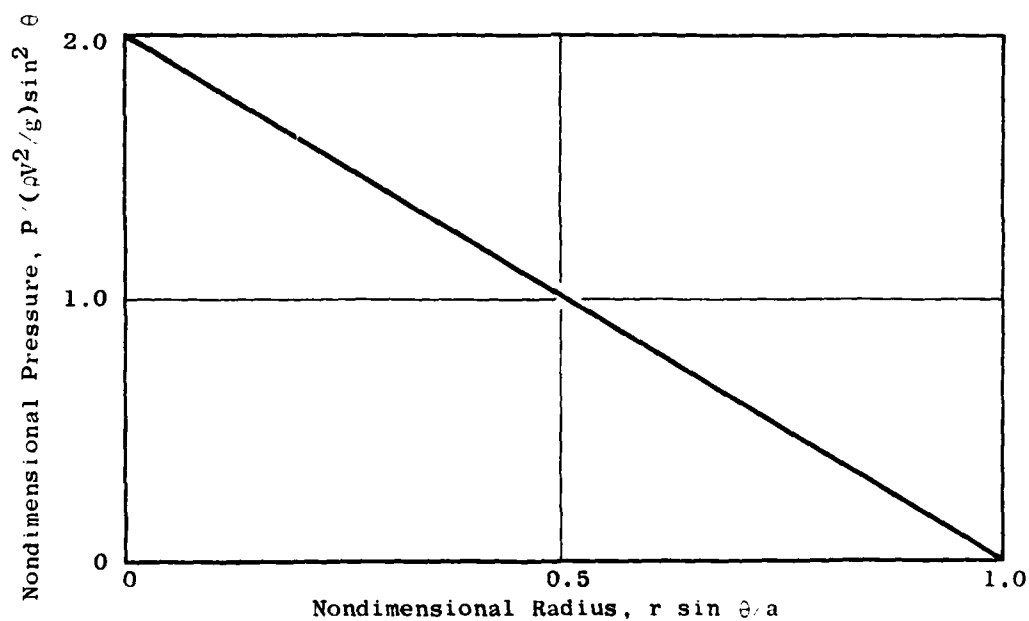


Figure 24. Generalized Bird-Impact Geometry Profile Based on Experimental Results.

during the impact. The loading model for the first-level response code is based on an approximate solution to the problem of the quasi-steady flow of a jet of arbitrary cross section flowing onto a surface with an arbitrary shape.

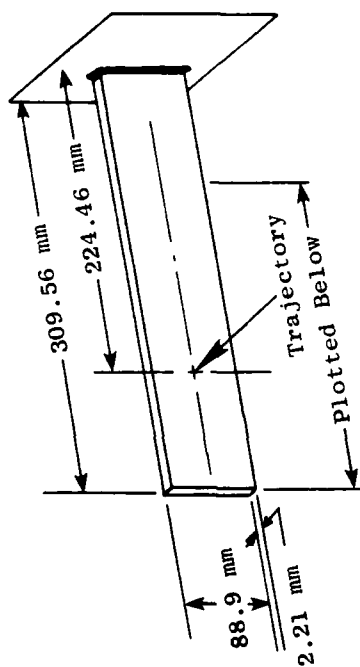
The cross-sectional area of the jet is determined from an analysis of the slicing of soft bodies by a row of fan or compressor blades. The loading-model pressure distributions for the first-level response code show excellent agreement with pressure distributions obtained in experiments in which birds, substitute birds, and ice spheres impacted on rigid targets. The loading model has been successfully interfaced with the first-level, finite-element, structural-analysis computer program.

The overall validity and limitations of the loading models will be determined by comparing the structural response predicted by the combined loading model/structural-analysis model with that observed in experiments.

#### 5.5 SUBTASK D - EXPERIMENTAL VERIFICATION OF LOADING MODELS

In order to check the adequacy of the integrated loading and response models, comparisons will be made between the analysis predictions and the test results for impacts on cantilevered plates. A range of impact parameters (mass for substitute birds and ice, velocity, and incidence) will be employed to ensure a full range of specimen response modes (i.e., elastic and elastic-plastic structural deformation and severe local deformation). The predictions of the complete model will be compared to experimentally derived results obtained from Task VI - Structural Element tests.

The experimental work has been completed. Displacement data collected with the Moiré fringe device for cantilever plates struck by simulated (gelatin) birds has been reduced. These measurements provide detailed, out-of-plane-displacement data at several increments of time and are presented in Figure 25. The excellent agreement between these measurements and analysis predictions is discussed in Section 7.4.3 of this report.



- Shot 40055
- 8-l-1 Titanium Cantilever Plate
- Microballoon Gelatin Projectile (Right Circular Cylinder)  
Mass = 82.6 g (3 oz)  
Density = 0.92 g/cm<sup>3</sup>
- Impact Velocity = 103.8 m/sec
- Impact Orientation: Normal

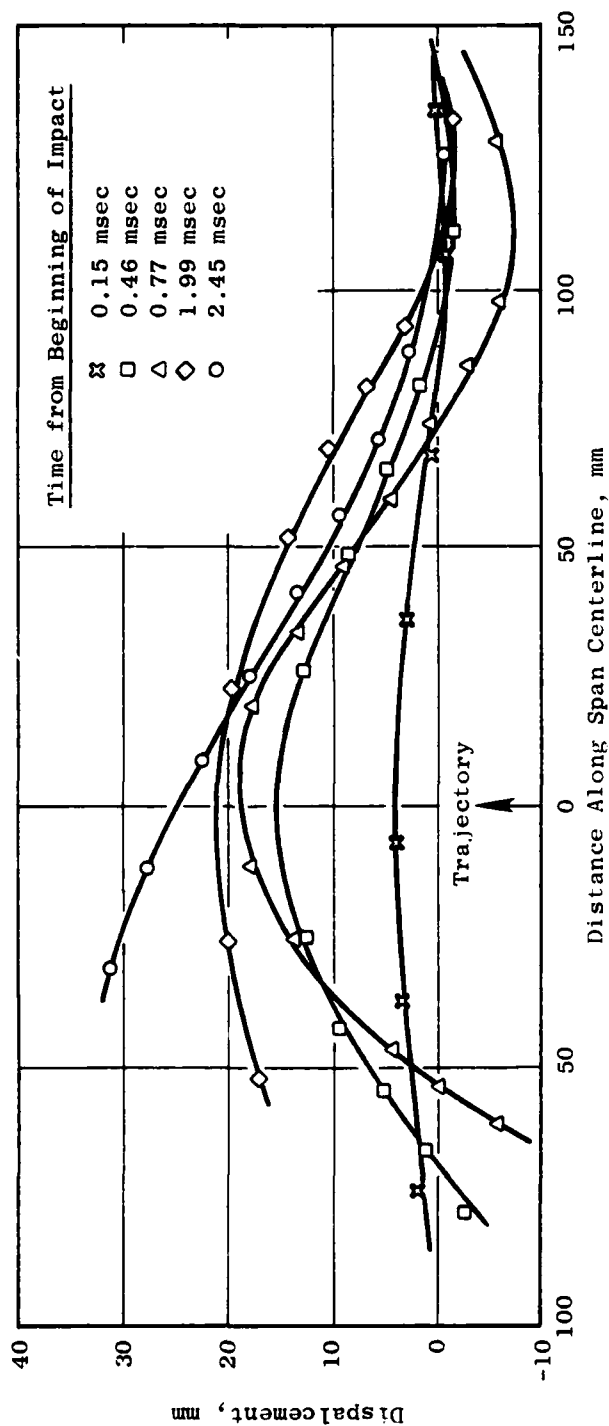


Figure 25. Deflected-Shape Plots of Cantilever Plate Struck by Simulated (Gelatin) Bird for Analytical-Model Validation.

## 6.0 TASK IV - MATERIAL RESPONSE AND FAILURE CRITERIA

### 6.1 SUBTASK A - GROSS STRUCTURAL DAMAGE PROPERTIES

#### 6.1.1 Introduction

Testing has been performed in two areas to establish gross structural-material response and failure data. First, bench impact tests have been conducted using the full-scale blades selected in Task V. The strain rates pertinent to the problem of foreign-object impacts have been determined from these tests. Impact tests, using the parameters of Tables 3 and 4, have been conducted on three different type blades, two of which are unshrouded. The two unshrouded blades are the J79 compressor first-stage stainless steel blade and the APSI first-stage fan B/Al composite blade. These blades were cantilever-mounted at the root. The third blade type is the F101 first-stage fan titanium blade. This blade is tip shrouded and, therefore, was fastened at both ends. Each blade type was impacted at the 30 and 70% span locations, and two blades of each blade type were used.

In the second part of Subtask A, tests are being conducted to obtain material-property data for the relevant strain rates. Forged bar stock was used to make the metal specimens (8Al-1Mo-1V titanium to represent the F101 blade and 410 stainless steel to represent the J79 blade). The 410 is being substituted for 403 stainless steel which is unavailable. Chemically, the two alloys are the same except for a small amount of chromium; this element does not affect the room-temperature mechanical properties. Standard, cylindrical specimens are used for the tension tests at low and intermediate strain rates, and the entire stress-strain curve is obtained using strain gages and an extensometer. The change in diameter is used to calculate Poisson's ratio. The high-strain-rate tests are conducted on the split Hopkinson bar using the standard tension-test specimen for that apparatus.

The mechanical-property tests have been completed for the metallic materials, and testing is in progress to establish the mechanical properties for the composite material.

The advanced composite selected for the study is boron/aluminum, used in the APSI Stage 1 fan blade, with a fiber layup of (0/22/0/-22). The 4-mil boron fibers are in a matrix of 2024 aluminum. Each ply is 4.7 mils thick and does not, in general, run the length of the blade. The center ply of the blade is a plate of aluminum. On either side of it is a ply of stainless steel wire mesh. The next plies on both sides are the B/Al layup. The entire outer blade surface is covered with a ply of stainless steel wire mesh. The leading edge has a thin coat of pure nickel.

The material properties are needed in three principal directions because the composite is anisotropic. The data needed are the tensile stress-strain curves for each direction, three Poisson's ratios, and three shear stress-strain curves. However, the collection of this information is simplified considerably by the use of laminate theory. This theory employs the results of

material-property tests on unidirectional specimens to calculate the bulk properties of the angle-ply layup.

#### 6.1.2 Real-Blade Strain Rates

Testing of the full-scale blades to obtain the maximum strain rates has been completed. The highest strain rates developed were less than 400 in./in./sec in any of the types of blades tested (J79, F101, and APSI). For the J79 impacts, the highest strain rate for the 30% span impact was 344 in./in./sec for a 1.5-pound-bird impact. This value was for a gage located on the midchord at the root in the spanwise direction. For the 70% span impact of the J79 blade, the highest strain rate was 362 in./in./sec for a 1.5-pound-bird impact. This value was for a gage directly behind the impact site and oriented in the chordwise direction.

The highest strain rate for the 30% span impacts of the tip-restrained F101 blade was 341 in./in./sec. For the 70% span impacts of this blade, the highest strain rate was 367 in./in./sec. Both strain rates were for 1.5-pound-bird impacts and for a gage located at the blade tip, along the leading edge, in the spanwise direction.

For the APSI blade, the highest strain rate developed was 366 in./in./sec for a 70% span impact of a 3-ounce bird. This occurred at a gage at the midchord of the root in the spanwise direction. The highest strain rate for the 30% span impact was 362 in./in./sec for a 3-ounce bird. This gage location was behind the impact site, and the orientation of the gate was in the direction of the chord.

#### 6.1.3 Material-Property Data

The material-characterization tests on the two metals, 410 stainless steel (410 substituted for 403) used for the J79 compressor Stage 1 blade and titanium 8Al-1Mo-1V used in the F101 fan Stage 1 blade, have been completed. The tests on the advanced composite (B/A1) used in the APSI fan Stage 1 blade have not yet started. As mentioned previously, the advanced composite used in the APSI blade is actually a hybrid composite. This blade has the following layup: SSWM/0°/22°/0°/-22°/SSWM/A1/SSWM/-22°/0°/22°/0°/SSWM. It will, therefore, be necessary to characterize the stainless steel wire mesh also.

Tensile tests conducted at the strain rates shown in Table 5 provide the desired mechanical-property data for the metallic materials. This range of rates encompasses the range of strain rates measured at select locations on the full-scale blade tests, 12-370 strain/second.

Table 5. Strain Rates of Metallic Material Characterization Tests.

Material	Strain Rates (strain/seconds)
8Al-1Mo-1V Titanium	$10^{-3}$ , $10^{-1}$ , 1, 500
403 Stainless Steel	$10^{-3}$ , $10^{-1}$ , 1, 700

The low and intermediate strain-rate tests ( $0.001 - 1.0 \text{ } \epsilon/\text{sec}$ ) have been conducted per ASTM E8-69<sup>(7)</sup>, and the specimen definition is shown in Figure 26. A standard tensile specimen used for the high-strain-rate tests on the split Hopkinson bar is shown in Figure 27. Table 6 shows the measured densities of 9Al-1Mo-1V titanium and 410 stainless steel. The mechanical properties acquired from the various strain-rate tests are presented in Tables 7 and 8. Figures 28 and 29 are plots of Young's modulus and yield stress versus strain rate.

Table 6. Density.

Material	Density
8Al-1Mo-1V Titanium	4.32 g/cm <sup>3</sup>
410 Stainless Steel	7.57 g/cm <sup>3</sup>

Relative to the high-strain-rate properties, it will be noted that a very small specimen was used to satisfy assumptions made in Hopkinson bar theory equations. This presents problems in obtaining accurate data from the tests, particularly in the elastic region. One problem is that achievable machining tolerances on the specimen in relation to load-surface alignment make it difficult to resolve small strains accurately. Secondly, an assumption made in developing the Hopkinson bar equations is that many stress-wave reflections occur in the specimen before a state of dynamic equilibrium is reached. This does not happen until some plastic deformation has taken place. In addition, once necking occurs in the specimen, a uniform stress field no longer exists; thus, the equations for stress and strain are invalid. This is a significant factor for the small specimens.

However, the split Hopkinson bar apparatus represents the state-of-the-art technique for obtaining stress-strain information at high strain rates. The stress-strain curves are considered most accurate in the range of 2 to 10% strain. The yield-stress values listed in Tables 7 and 8 represent the point on the curves where the load ceases to increase significantly for a rather large increase in displacement. (The 0.2% offset method obviously cannot be used because of the lack of data in the elastic region.) The ultimate stress and ultimate strain values from these tests were the final point of the curve. Although the values from the high-strain-rate tests cannot be used as exact data points, they are useful in establishing the trend of the strain rate dependence of the subject materials over nearly seven decades of strain rate.

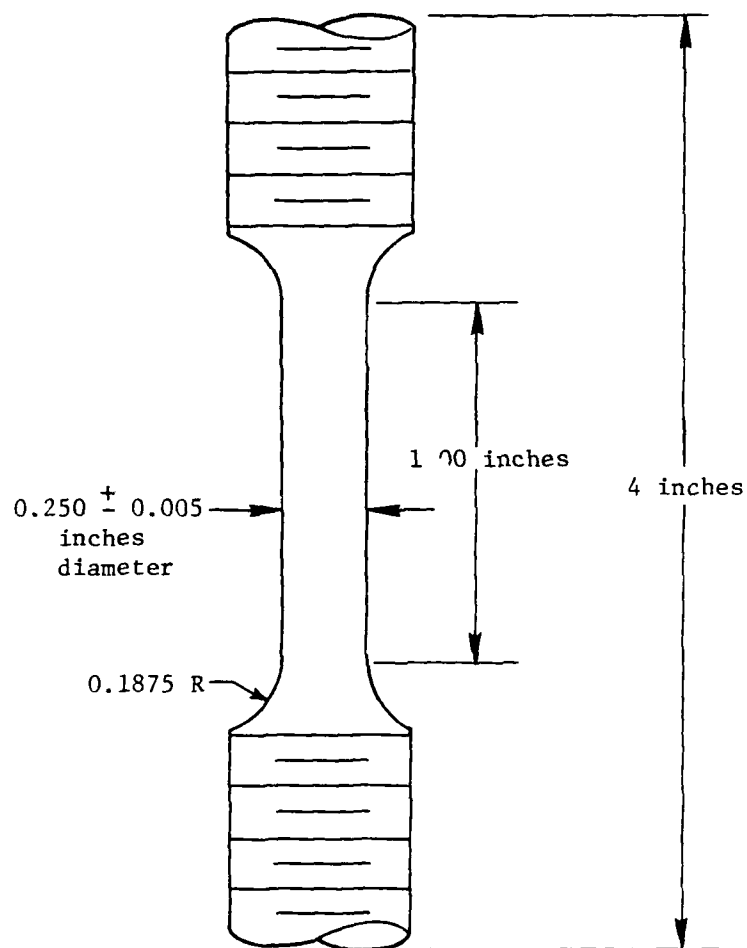
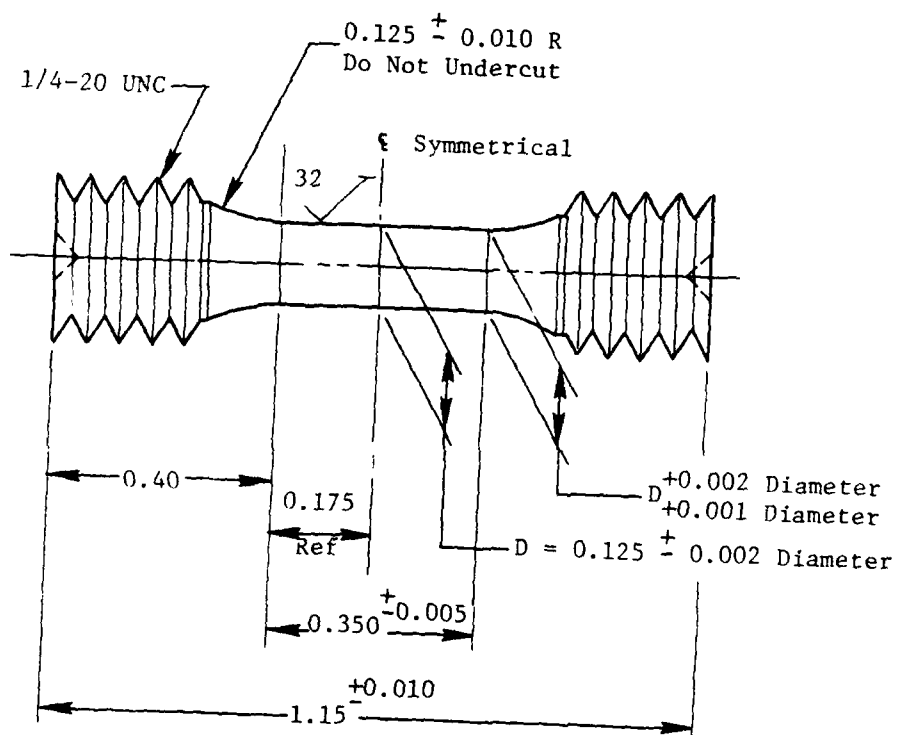


Figure 26. Specimen for Low and Intermediate-Strain-Rate Tests for Metals.





Note: All Dimensions are inches.

Threaded Tension Hopkinson Bar Specimen

Figure 27. Specimen for High-Strain-Rate Tests.

Table 7. Mechanical Properties Obtained for 8Al-1Mo-1V Titanium.

Specimen	Strain Rate ( $\epsilon/\text{sec}$ )	Elastic Modulus ( $\times 10^6$ psi)	Shear Modulus ( $\times 10^6$ psi)	Yield Stress (ksi)	Ultimate Stress (ksi)	Ultimate Strain (percent)
1-Ti	0.001	16.9	6.5	148.9	202.5	28.2
2-Ti	0.001	17.3	6.7	148.7	200.8	27.2
3-Ti	0.001	17.4	6.8	148.7	199.3	21.8
4-Ti	0.10	15.8	6.3	156.3	188.5	13.7
5-Ti	0.10	16.9	6.8	153.0	189.1	15.9
6-Ti	0.10	17.1	6.8	156.4	194.5	15.3
7-Ti	1.0	17.3	6.8	164.0	184.6	15.7
Ti-3	550	*	*	203.0	161.1	13.7
Ti-2	560	*	*	202.0	154.2	14.5
Ti-1	580	*	*	208.0	158.7	15.3

Poisson's Ratio = 0.279

\*Elastic properties are not obtainable from the high-strain-rate tests.

Table 8. Mechanical Properties Obtained for 410 Stainless Steel.

Specimen	Strain Rate ( $\epsilon/\text{sec}$ )	Elastic Modulus ( $\times 10^6$ psi)	Shear Modulus ( $\times 10^6$ psi)	Yield Stress (ksi)	Ultimate Stress (ksi)	Ultimate Strain (percent)
4-SS	0.001	27.4	10.6	84.2	207.2	26.7
5-SS	0.001	30.5	11.7	84.8	207.2	27.2
6-SS	0.001	33.7	12.9	84.9	211.9	26.9
9-SS	0.10	27.7	11.2	87.2	191.9	25.7
10-SS	0.10	26.4	10.2	87.0	188.3	26.8
11-SS	0.10	28.2	10.9	89.2	198.3	23.5
12-SS	1.0	27.2	10.4	86.6	182.7	23.8
13-SS	1.0	26.1	10.0	91.3	185.5	25.4
14-SS	1.0	27.2	10.4	94.5	183.8	24.6
15-SS	1.0	28.0	10.9	88.8	184.7	25.6
SS-5	680.0	*	*	124.0	129.5	16.9
SS-4	760.0	*	*	123.0	130.0	17.2
SS-3	700.0	*	*	131.0	131.4	18.0
SS-2	530.0	*	*	128.0	**	**
SS-1	340.0	*	*	126.0	**	**

Poisson's Ratio = 0.297

\* Elastic properties are not obtainable from the high-strain-rate tests.

\*\* These specimens did not fail.

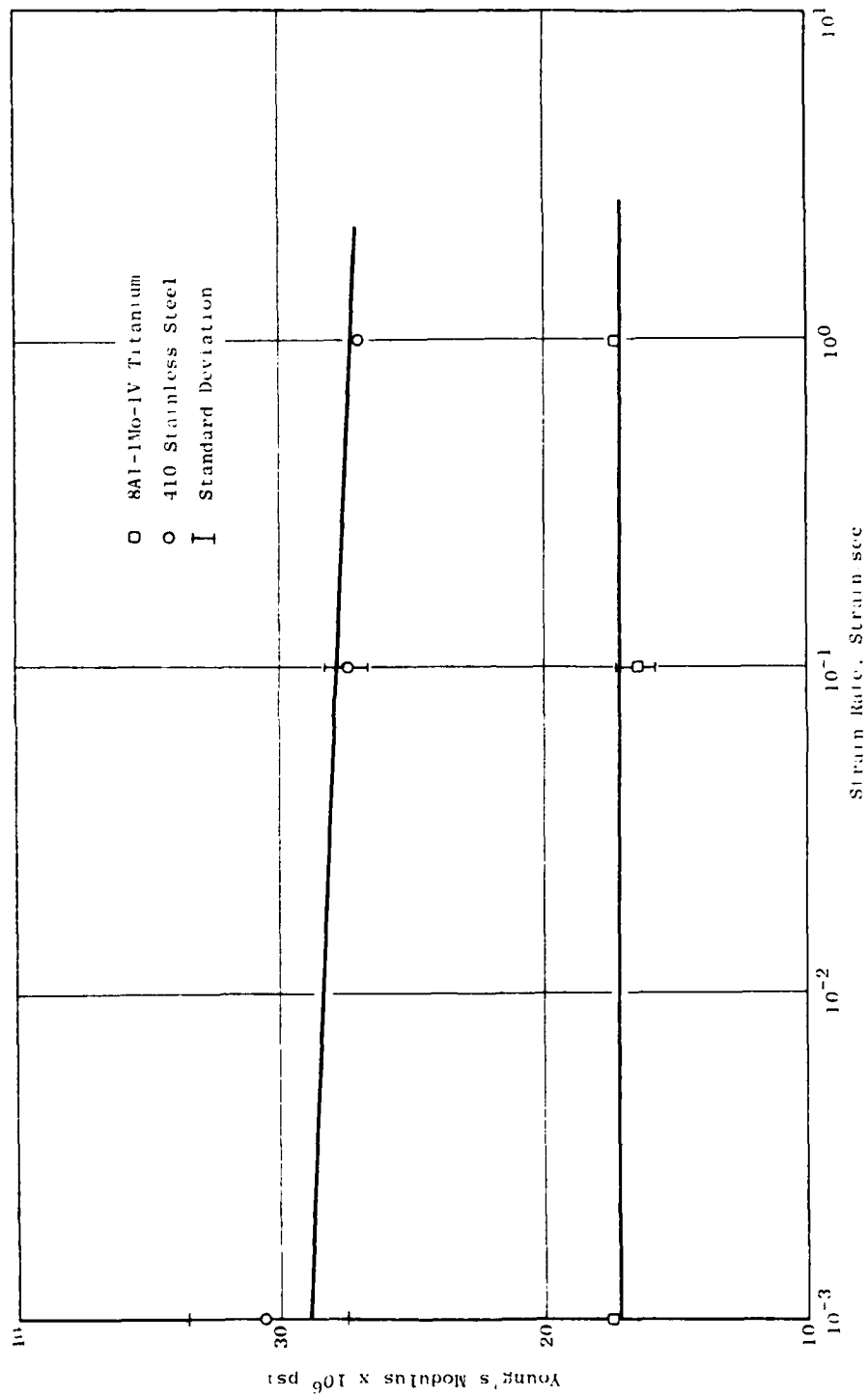


Figure 28. Young's Modulus Vs. Strain Rate.

SAE-1010 Titanium

○ 410 Stainless Steel

□ Standard Deviation

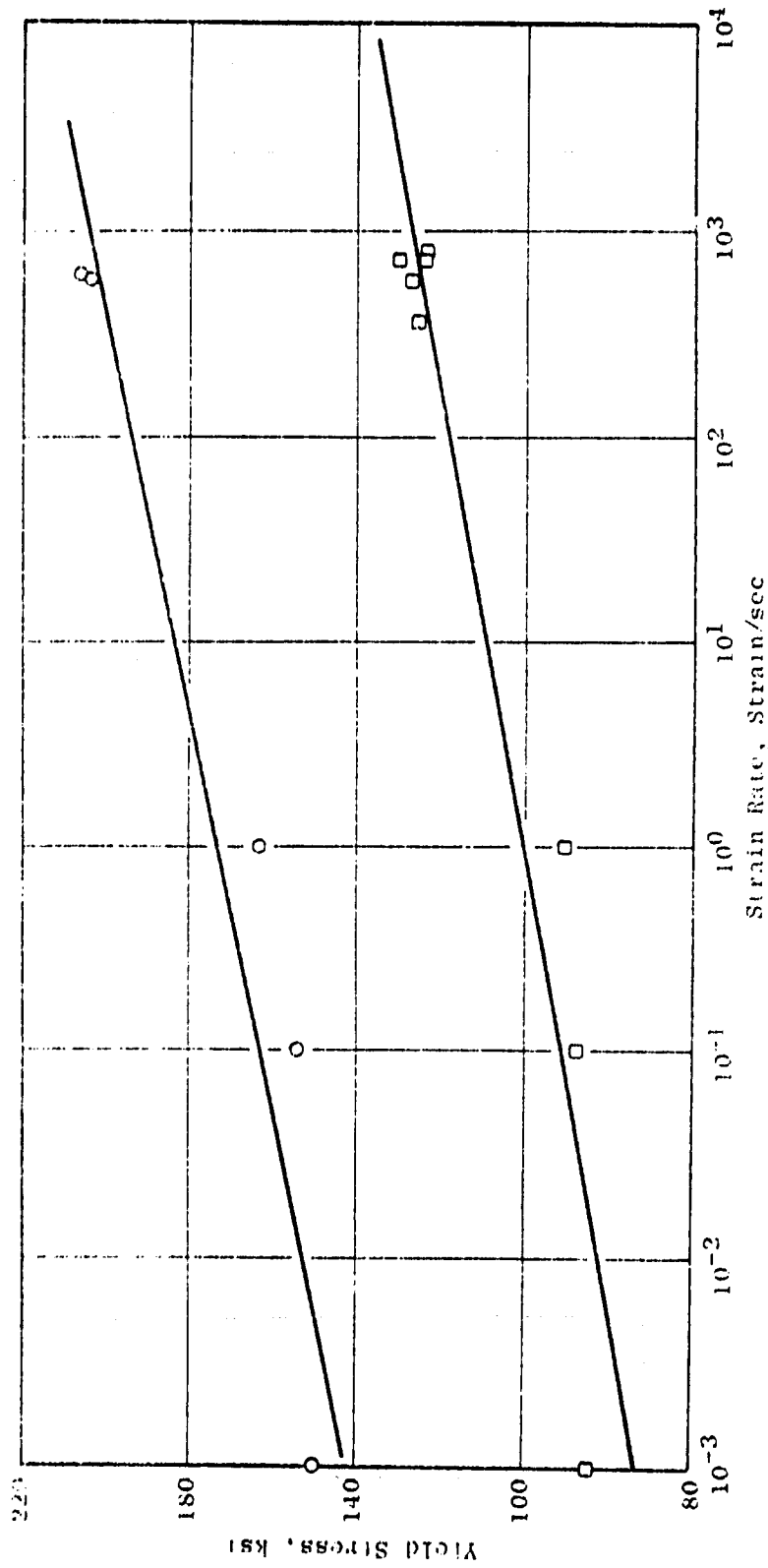


Figure 29. Yield Stress Vs. Strain Rate.

Best Available Copy

The test matrix that will be used for the characterization of the boron/aluminum and the stainless steel wire mesh is shown in Table 9. For the tensile tests in the direction of the symmetry axes ( $0^\circ$  and  $90^\circ$ ), a modified ITTRI specimen configuration will be used<sup>8</sup>. This specimen is shown in Figure 30. For the shear tests in the interlaminar plane, the  $10^\circ$  off-axis shear test developed by Chamis and Sinclair<sup>9</sup> will be used for the B/Al. A drawing of the specimen appears in Figure 31. Torsion rod specimens will be used to determine the transverse shear properties for both the B/Al and the stainless steel wire mesh. The in-plane shear properties for the stainless steel wire mesh will be determined with the  $\pm 45^\circ$  shear panel specimen.

Table 9. Characterization Tests for B/Al and Stainless Steel Wire Mesh.

<u>Material</u>	<u>Test Description</u>	<u>Strain Rates (<math>\text{sec}^{-1}</math>)</u>
B/Al	$0^\circ$ Tension	1,10
	$90^\circ$ Tension	1,10
	$10^\circ$ Off-axis Shear	10
	Rod Torsion Shear	10
SSWM	Tension (in plane)	1,10
	Torsion (through the thickness)	1,10
	$\pm 45^\circ$ Shear	10
	Rod Torsion Shear	10

The through-the-thickness tensile specimen shown in Figure 32 will be used to determine the normal-to-the-plane tensile properties for the stainless steel wire mesh. The tensile specimens (including  $10^\circ$  off-axis and  $\pm 45^\circ$  panels) will be instrumented with high-resistance strain gages. For the through-the-thickness and torsion rod specimens, it is planned to use an extensometer to measure displacement.

It is not anticipated that the composite will be significantly strain-rate sensitive. Strain-rate effects in B/Al were investigated by Krinke, Barber, and Nicholas<sup>10</sup> using a three-point bend (Charpy impact) technique. They found no significant strain-rate effects over six orders of magnitude; the highest strain rate employed in the study was  $100 \text{ sec}^{-1}$ .

## 6.2 SUBTASK B - LOCAL LEADING-EDGE DAMAGE

### 6.2.1 Introduction

This subtask is concerned with the generation of empirical design data for local leading-edge damage to first-stage fan and compressor blades. Most of the testing to determine and quantify the damage caused by leading-edge impacts for a range of pertinent impact conditions has been accomplished. The results of this study will include data expressed in terms of the residual properties of the materials which are directly relevant to fan and compressor designers.

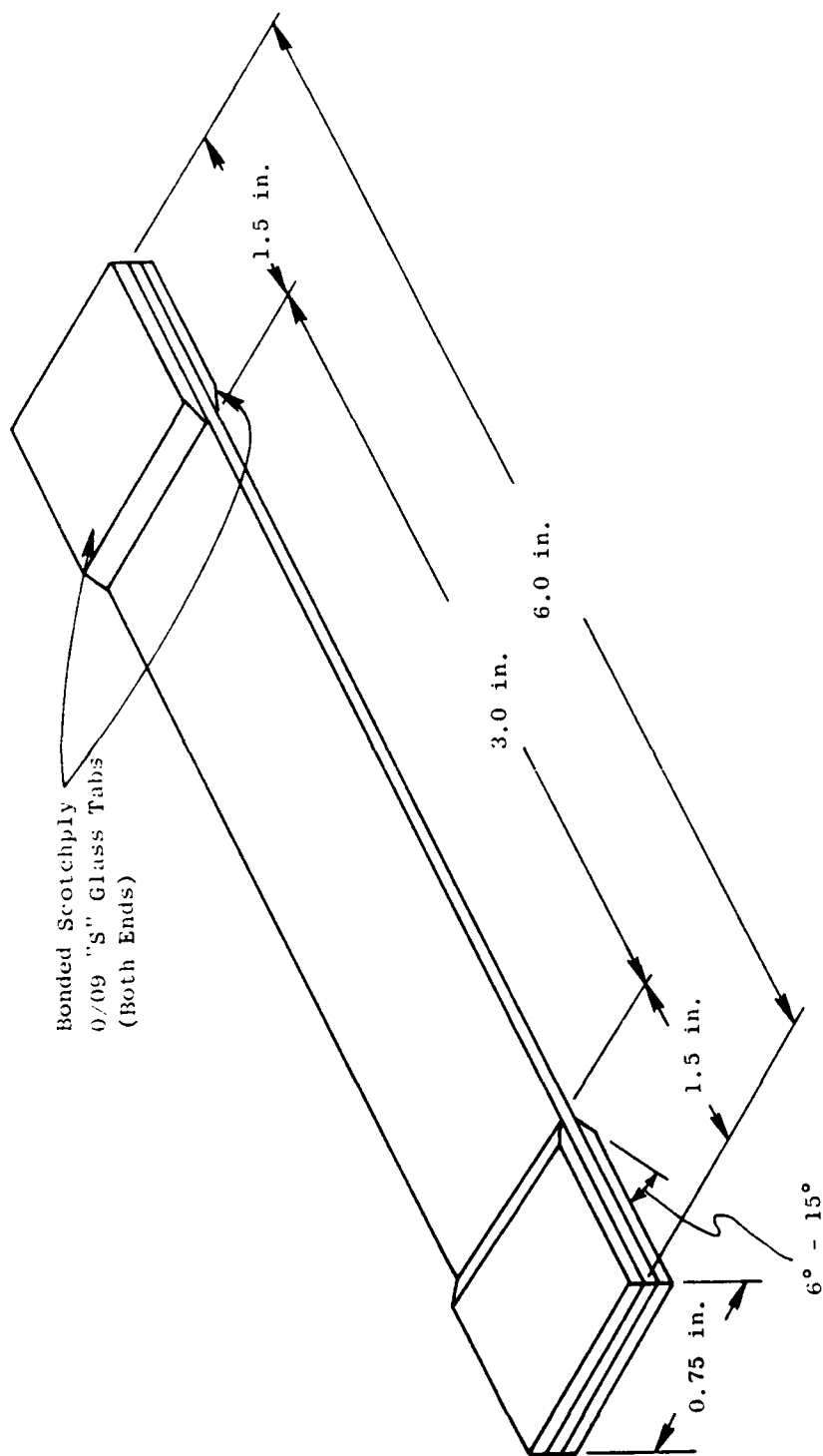


Figure 30. Modified ITTRI Specimen.

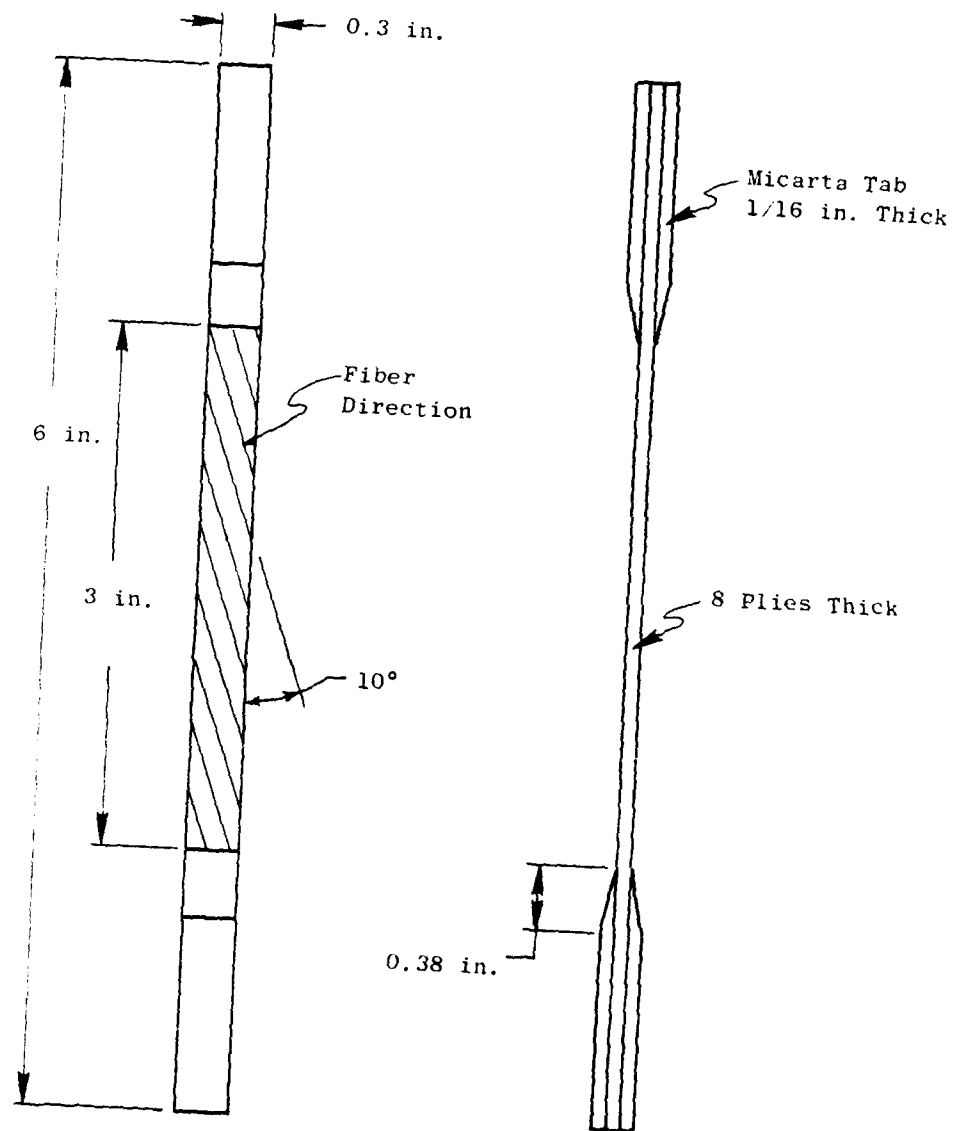


Figure 31. Modified 10° Off-Axis Shear Specimen.



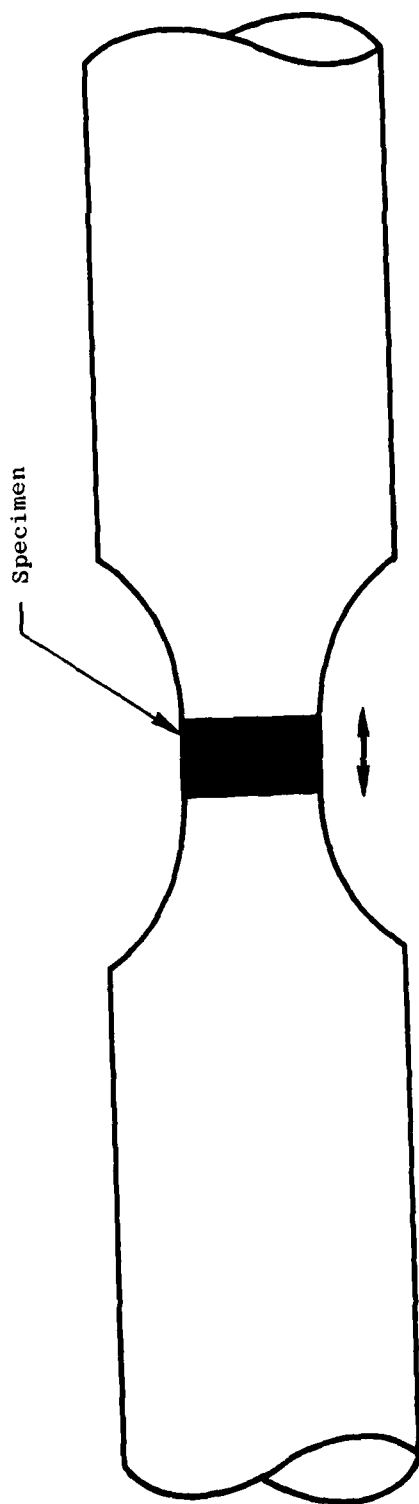


Figure 32. Through-the-Thickness Test Specimen.

### 6.2.2 Overall Approach

Three types of blade materials, geometries, and sizes have been investigated using substitute bird materials, ice, granite pebbles, and steel spheres as the impactors. This range of impactors is representative of the types of objects commonly ingested into engines. The three blade types are the J79 blade using type 403 stainless steel, the F101 blade using 8-1-1 titanium, and the APSI metal-matrix boron/aluminum blade. Fabricated metal and composite specimens and actual APSI blades have been tested. The geometries of the leading edges of the fabricated specimens are similar to the geometries of the blade types at the 50% span location. Three specific investigations have been conducted in this subtask. The first investigation established a base of damage data. The second addressed scaling and subscale tests. The third investigated the effects of preload and possible damage enhancement. In conjunction with the above investigations, fatigue and tensile tests are being performed on damaged and undamaged specimens to establish the effect of impact on these properties.

Damage base data were generated using nominal-thickness, fabricated specimens (the leading-edge thicknesses are identical to the corresponding blade type at the 50% span level). Half-thickness fabricated specimens were then used in a scaling-effects investigation. Preload investigations were performed on the fabricated metal specimens to simulate the effects of centrifugal loading on local leading-edge damage. The specimens were preloaded at stresses typical of the impact locations (30 and 70% span levels).

## 6.3 SUBTASK C - MATERIAL-SCREENING TESTS

### 6.3.1 Introduction

This subtask addressed the development of material-screening tests necessary to evaluate and effectively rank candidate materials for fan and compressor blades that possess superior FOD resistance. The material parameters investigated in this study include: (1) the perforation resistance of the material, (2) the extent the material may plastically deform, (3) the extent to which the material is vulnerable to catastrophic structural failure, and (4) the extent to which the material is vulnerable to degradation of fatigue properties.

In this investigation, the above material parameters will be defined in terms of response to impact in small-scale tests. The perforation-resistance parameter will be quantified as a ballistic limit velocity,  $V_L$ , for a given impact configuration. The quantity  $V_L$  is a direct measure of the amount of impact energy the material can absorb without catastrophic local damage. The plastic-deformation parameter will be quantified by conducting impact tests which maximize the likelihood of plastic deformation. The catastrophic structural-failure parameter will be quantified in a Charpy impact test designed to produce gross structural failure. The fatigue-properties parameter will be quantified in terms of reduction of ultimate fatigue strength. The parameters defined by these tests may be considered individually or combined with suitable weighting functions to compute an overall figure of merit for a particular material.

### 6.3.2 Testing and Analysis

The experimental work in this subtask has been completed, and the data analysis for the residual fatigue testing is underway.

Table 10 gives the results of the ballistic-limit and maximum-deformation testing. The projectiles used in the testing included the 0.25-inch diameter granite pebble, the 0.5-inch diameter microballoon gelatin bird, and the 0.5-inch ice ball.

Table 10. Ballistic Limit Results (ft/sec).

Target Material	0.25-inch Pebble	0.5-inch Microballoon Gelatin Bird	0.5-inch Ice Ball
410 Stainless Steel (annealed)	3379	>3012	>2036
410 Stainless	3335	>1957	----
8-1-1 Titanium	2859	>1961	>2173
6-4 Titanium	----	>1923	----
B/Al Composite	633	913	----
G/Ep. Composite	----	318	----

The specimen size used in the testing was 3 x 3 inch having a thickness of 0.06 inches. All of the impacts were normal impacts (90°). The results show that the composite materials had the lower ballistic limits.

The six materials evaluated in the instrumented Charpy impact tests included 8-1-1 titanium, 6-4 titanium, 410 stainless steel in the annealed condition, 410 stainless steel in the heat-treated condition, boron/aluminum, and graphite/epoxy. The instrumented Charpy impact tests were conducted on a Tinius Olsen pendulum impact machine instrumented with a Dynatype loading device and associated electronics. Prior to testing, dimensions were measured for all specimens. Load-versus-time and energy-versus-time curves were recorded on a storage oscilloscope and photographed. The results of the Charpy impact test analysis are shown in Table 11 for individual specimens. The peak force (lb) and peak energy (ft-lb) readings were measured from the oscilloscope traces. The energy must be corrected to account for the reduction in velocity resulting from the impact with the sample. The last column of Table 11 gives the corrected energy (ft-lb) taking into account this reduction of velocity. The table indicates that the 8-1-1 Ti material is the best material in regards to the Charpy test. The ranking of the metals would be as follows: 8-1-1 Ti is first, followed by the 6-4 Ti material, then the heat-treated 410 stainless steel, and finally the 410 stainless steel in the annealed condition. For the composite materials, the Charpy tests indicate that the graphite-epoxy material is better than the boron-aluminum material.

Table 11. Charpy Test Results.

Material	Specimen Number	Peak Force (lb)	Peak Energy (ft-lb)	Corrected Peak Energy (ft-lb)
8-1-1 Ti	1	180.6	10.1	8.6
8-1-1 Ti	2	183.6	10.7	9.1
8-1-1 Ti	3	180.6	10.7	9.1
8-1-1 Ti	4	188.1	10.9	9.2
6-4 Ti	1	167.2	9.4	8.1
6-4 Ti	2	167.2	9.6	8.3
6-4 Ti	3	164.2	9.0	7.8
6-4 Ti	4	165.7	9.3	8.1
410 SS (annealed)	1	77.6	4.3	4.0
410 SS (annealed)	2	79.1	4.3	4.0
410 SS (annealed)	3	76.1	4.2	3.9
410 SS (annealed)	4	76.1	4.2	3.9
410 SS (heat-treated)	1	153.7	9.1	7.9
410 SS (heat-treated)	2	153.7	9.0	7.8
410 SS (heat-treated)	3	149.3	8.8	7.7
410 SS (heat-treated)	4	149.3	8.7	7.6
Boron/Aluminum	C-1D	85.1	0.45	0.45
Boron/Aluminum	C-1E	88.1	0.51	0.51
Boron/Aluminum	C-2E	92.5	0.51	0.51
Boron/Aluminum	3D	89.6	0.51	0.51
Boron/Aluminum	C-3D	87.3	0.43	0.43
Graphite/Epoxy	BA-3-A	148.5	0.87	0.86
Graphite/Epoxy	BA-3-B	150.0	0.97	0.96
Graphite/Epoxy	BA-3-D	128.6	0.70	0.69
Graphite/Epoxy	BA-3-C	134.3	0.78	0.77

## 7.0 TASK V - PARAMETRIC ANALYSIS

### 7.1 INTRODUCTION

Parametric relationships describing the changes in dynamic structural response of impacted simple-plate elements with the progressive introduction of blade airfoil geometric features will be derived in this task. Additionally, the adequacy of the structural-response models formulated in Tasks II, III, and IV will be investigated and modifications made as necessary.

This task is broadly divided into three phases. The first phase is analysis and correlation of Task VI tests conducted with simple, cantilevered, flat plates with different aspect ratios and thicknesses. The second phase is the analysis and correlation of Task VI tests with geometry and impact conditions more representative of actual airfoil FOD dynamics but still simple enough that the sources of observed effects can be isolated. The third and final phase of this task is the analysis and correlation of Task VI and Task IX tests of the three selected first-stage airfoils in stationary and rotating environments.

### 7.2 BLADES SELECTED FOR ANALYSIS

The three blades selected are representative of first-stage airfoils from Air Force inventory, production development, and advanced-development engines. These blades include subsonic, transonic, and supersonic airfoil shapes and stainless steel, titanium, and an advanced composite material. The blades selected are listed below:

<u>Blade</u>	<u>Representing</u>	<u>Airfoil</u>	<u>Material</u>	<u>Shrouded</u>
J79	Air Force Inventory	Subsonic	Stainless Steel	No
F101	Production Development	Transonic	Titanium	Yes
APSI	Advanced Development Supersonic Engines	Supersonic	B/Al Composite	No

### 7.3 PARAMETRIC MATRIX

A parametric matrix has been formulated to define the impact conditions and response-model geometries that will be analyzed in Tasks V and X and provide guidance in the selection of the structural-element and full-scale-blade tests that will be conducted in Tasks VI, IX, and XI.

## 7.4 NOSAPM MODELING AND ANALYSIS

### 7.4.1 Normal-Impact Analysis

The following paragraphs discuss the modeling and analyses of Task VI tests. Table 12 lists the principal conditions of one of these tests. It should be noted that, in this test, both the projectile mass and the enclosing sabot impacted the blade. Thus, although the projectile mass alone is 3.81 cm in diameter and 81.4 g in weight, the total weight of 100.5 g with an outside diameter of 5.08 cm must be considered for full momentum transfer. The geometry of the test plate and the impacting object are shown in Figure 33. The planform is the same aspect ratio as the F101 blade.

In order to carry out the analysis, a finite-element model of this test case was constructed using thirty-four 16-noded elements. The finite-element model is shown in Figure 34 looking straight down on the planform of the plate. As can be seen in the figure, the mesh was made finer in the vicinity of the impact in order to better approximate the expected local bulging. Beaming action is expected to dominate in the areas remote from the impact site, and the elements are larger. The impact pressure is spread over Elements 20, 21, 24 and 25. These elements bound a rectangular area of 16.94 cm<sup>2</sup> (2.62 in.<sup>2</sup>). Because the sabot as well as the projectile mass impacted the target plate, there is a degree of uncertainty with respect to the details of the loading condition. It was decided to use the 16.94 cm<sup>2</sup> impact area which is intermediate to the total area of mass plus sabot and mass alone. The length of the impacting mass both in the test and in the analysis was 7.62 cm (3 in.). The properties of 8-1-1 titanium used in this analysis are listed on Figure 35 along with the bilinear approximation to the stress-strain curve used for the finite-element model. It should be pointed out that these properties are more appropriate for 4-6 titanium and were used before the 8-1-1 data from UDRI became available. As a result, the corrected modulus and yield stress should be used in future analyses. However, these properties are adequate for gaining modeling experience.

At the time these analyses were run, the interactive loading model for normal impact was not yet available. As a result, the loading history applied to Elements 20, 21, 24, and 25 was derived from simple impulse-momentum considerations and the experimental results reported by Barber, Wilbeck, and Taylor<sup>6</sup>. The pressure exerted by a steady jet of fluid impacting a flat surface can be calculated as

$$P = \rho V^2 \quad (21)$$

where  $\rho$  is the mass density and  $V$  is the normal impact velocity. Refer to Figure 22.

Since the test under consideration involved the impact of both sabot and projectile mass, the density ( $\rho$ ) used here is an effective density calculated as the total mass of sabot and projectile ( $M$ ) divided by the total volume of the impacting mass ( $A \times L$ ). Here  $A$  is the area under the impact on the model

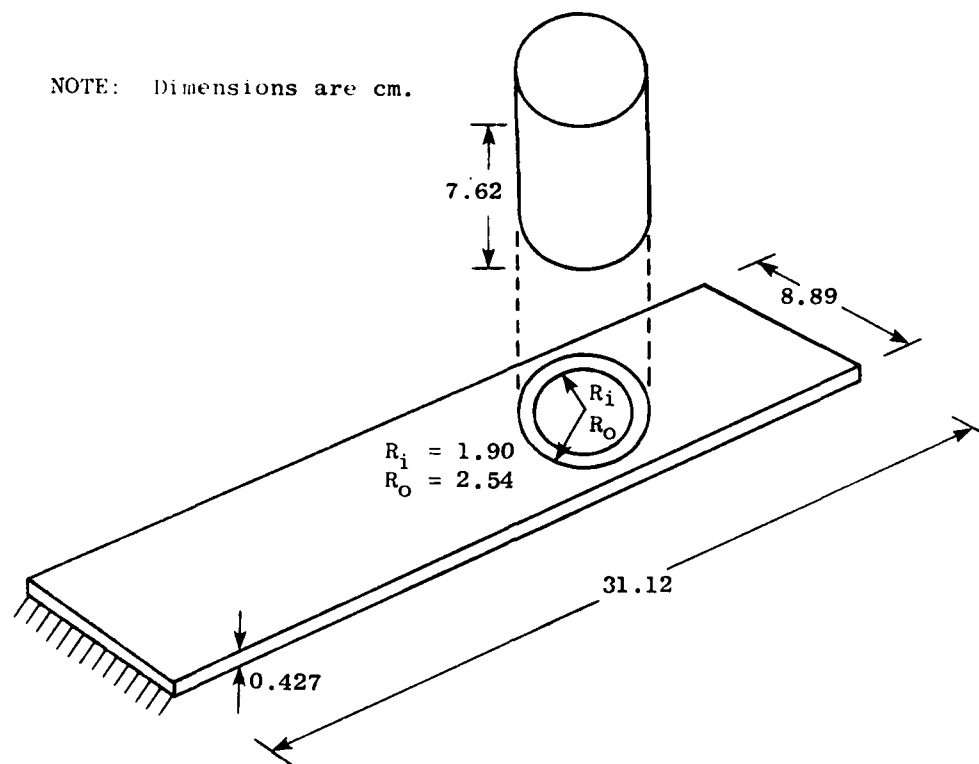


Figure 33. Geometry of Test Impact.

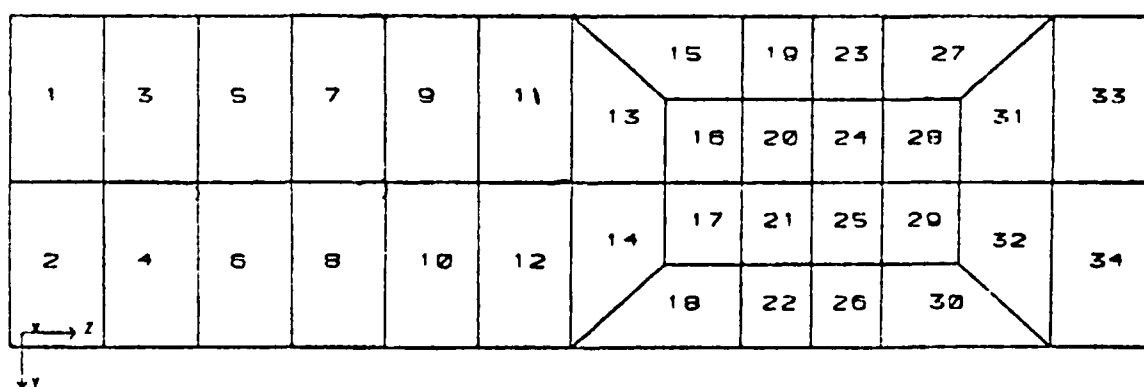


Figure 34. Finite-Element Model.

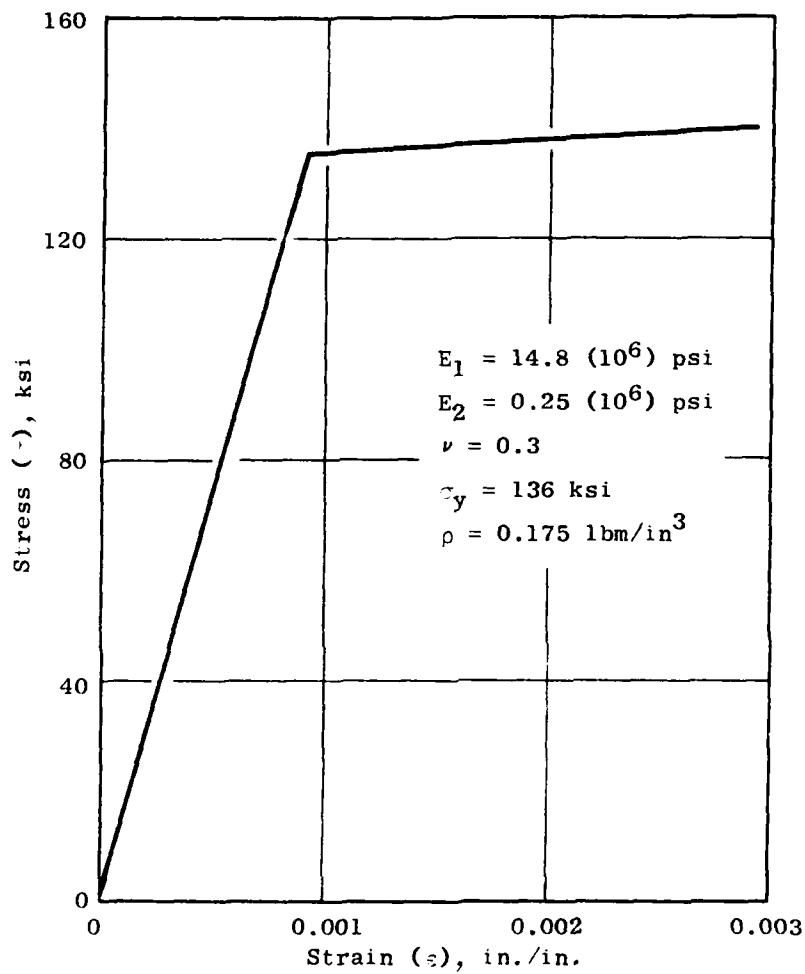


Figure 35. Stress-Strain Curve Used in Analysis of Test Shot 20094.



(Elements 20, 21, 24, and 25) and  $L$  is the length of the impactor. Barber, Wilbeck, and Taylor suggest that, during a normal impact, the peak pressure is a shock pressure about twice the magnitude of the steady-state pressure and occurs at roughly 20% of the total impact time duration. Thereafter, the pressure reduces, in a roughly linear manner, to zero; refer to Figure 23. Using this approach, the model for the impact pressure was formulated. This pressure was spread uniformly over the impact area, and the pressure history is exhibited in Figure 36.

The purpose of this full-scale analysis was to develop experience in the modeling techniques available within the Level 1 package for application to the blade-impact problem. There are numerous decisions which must be made in conducting such a finite-element analysis, including: choice of an appropriate time step, choice of the number of Gauss points for element-stiffness integration, stiffness reformation strategy, and use of the equilibrium iteration technique for equation solution. A great deal of information with respect to all of these questions was gathered during the course of the analyses.

Table 12. Dayton test Conditions.

Shot Number	20094
Date	2-8
Projectile Mass	81.4 g (2.87 oz)
Total Mass	100.5 g (3.54 oz)
Projectile Diameter	3.81 cm (1.5 in.)
Diameter of Projectile and Sabot	5.08 cm (2.0 in.)
Impact Velocity	177.4 m/sec (582 ft/sec)
Target Material	8-1-1 Ti
Impact Angle	90°
Center of Impact (as percent of span from root)	70%
Mount	Cantilever; 31.12 cm (12.25 in.) above mount

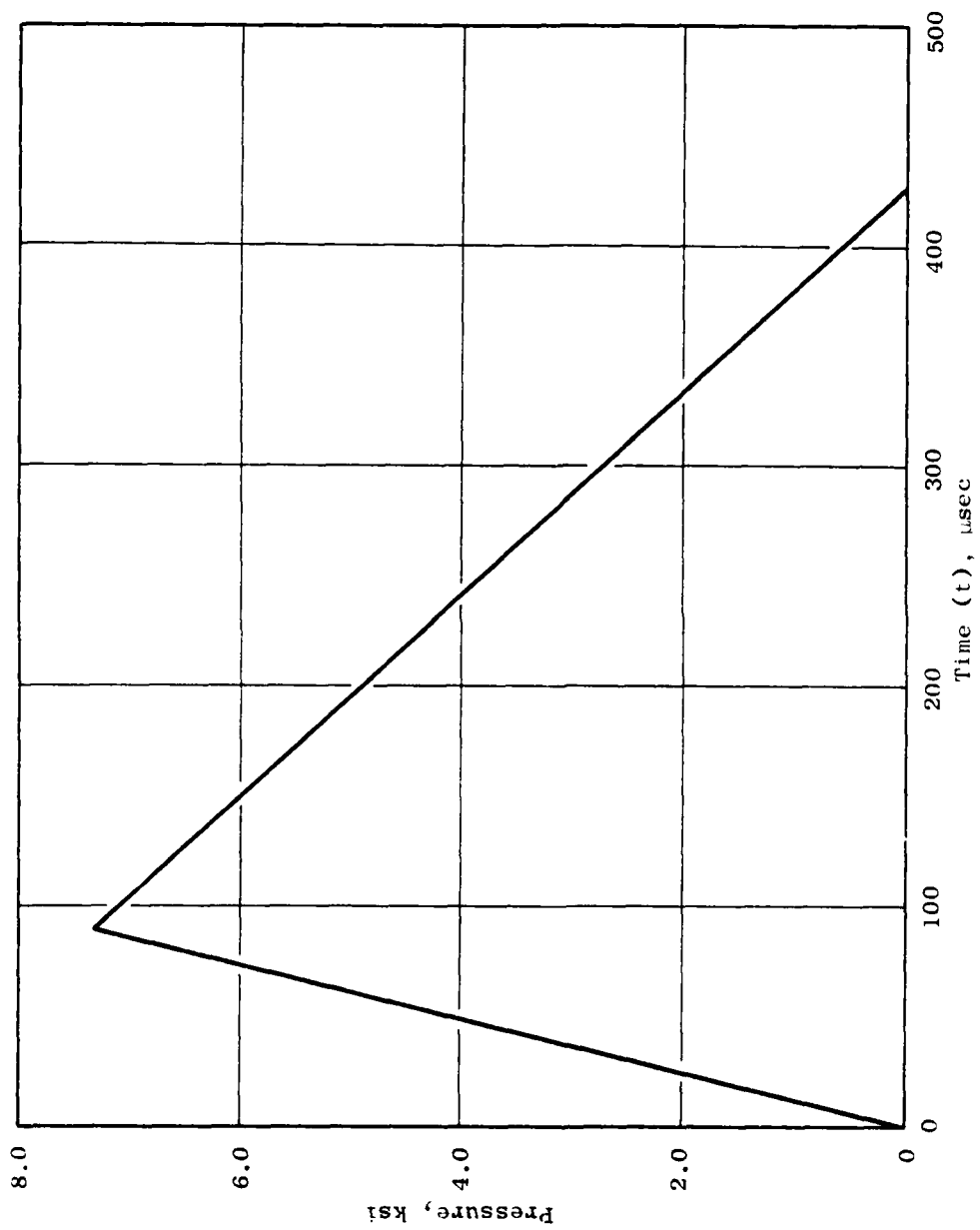


Figure 36. Pressure-Loading History.

Perhaps the most challenging area of computation strategy in this problem is the extremely wide range in time scales that must be considered during a complete impact analysis. Table 13 lists some of the most important characteristic times for the problem described herein and illustrates the extreme differences in time frames. As can be seen, these time frames span almost four orders of magnitude. Yet there are events at both ends of the scale which are regarded as significant. For example, during the time  $0 + 500$   $\mu$ sec the impact is occurring, and the intent of this program has been to deal with interaction between impactor and structure during this time. In addition, it is during this time that large local stresses appear in blades and plates and cause in bulging and curlback. On the other hand, the large tip deflections and large root stresses associated with gross structural damage occur at the other end of the time scale: 10 to 20 msec after impact. It appears that the only way to deal with both of these time frames is with two time steps. One time step would be used for the study of local effects; then, using the restart capability of the Level 1 package, the larger time frame would be studied with a significantly larger time step using the last step of the short-time solution as initial conditions.

Table 13. Characteristic Times.

Time required for a plane stress wave to travel from centerline to plate edge (Y-face) and return	15 $\mu$ sec
Time required for a plan stress wave to travel from 70% span to tip and return to 70% span	40 $\mu$ sec
Characteristic period of plate response for the square impact area	80 $\mu$ sec
Time required for a plane stress wave to travel from 70% span to root and return to 70% span	90 $\mu$ sec
Load duration	430 $\mu$ sec
Characteristic period of 4th flexural mode	870 $\mu$ sec
Characteristic period of 3rd flexural mode	1740 $\mu$ sec
Characteristic period of 2nd flexural mode	4900 $\mu$ sec
Time to maximum tip deflection	8000 $\mu$ sec
Characteristic period of 1st flexural mode	30,000 $\mu$ sec

A time step of  $\Delta t = 20 \mu\text{sec}$  was chosen for this analysis. This time step provides adequate representation for the loading history as well as the flexural modes of the problem. It is too large to closely follow the movement of plane stress-wave fronts in the plate, but since the local or bulging response is nearly quasi-static with respect to the load application this does not appear to be a large disadvantage. For this analysis, three Gauss points through the thickness as well as  $3 \times 3$  in the plane of the plate were used for numerical integration. There is some indication that a  $2 \times 2$  Gauss point scheme should be used in-plane, and a recommendation on this issue will be pursued. If effective, it would substantially reduce the cost of the analysis. The intervals of stiffness reformation and the use of equilibrium iteration are described in Figure 37. Observation of the change in geometry as well as the appearance of plasticity in the problem indicate that these choices are adequate. It has been discovered during application of NOSAPM to other structural problems at CRD that the equilibrium iteration technique will not work during large-scale unloading from plastic states of stress. The job will prematurely terminate if it is used in such cases.

Figures 38 through 42 illustrate some of the results of this analysis for times less than  $500 \mu\text{sec}$  after impact. The general behavior of the response as well as the nonlinear nature of the problem are illustrated. Figure 38 plots the lateral displacement of the plate (X-displacement) versus the Y-location at the 70% span chord-line designated S-S in the drawing. The solid lines illustrate the full nonlinear response of the plate at 60, 100, 220, 380, and  $500 \mu\text{sec}$ . As can be seen, at 60 and  $100 \mu\text{sec}$  the response is characteristic of local plate bulging. The relatively high-speed flexural waves associated with this response reach the edges of the plate around 80 to  $100 \mu\text{sec}$  after the impact; thereafter the lateral displacement of the plate becomes much more characteristic of a beam than a plate, as can be seen from the rather constant value of lateral deflection across the chord line. The dashed lines in Figure 38 illustrate the linear solution to the same impact problem. At 60 and  $100 \mu\text{sec}$  the linear and nonlinear solution coincide. However, comparison of the two solutions for larger times indicates that the nonlinear, in-plane stiffness associated with displacements of the order of the plate thickness is clearly active in reducing the displacements which might be expected from a linear solution. There are no stresses above the yield point of the titanium until about  $140 \mu\text{sec}$ , and even then these stresses are extremely localized, appearing only near plate surfaces where tensile membrane and bending stresses are additive.

Figure 39 plots lateral displacement as a function of the position along the plate centerline B-B described in the accompanying figure. The solid lines describe the nonlinear plate response for 60, 140, 180, 300, and  $500 \mu\text{sec}$  and, again, give a clear indication of how the behavior develops. At  $60 \mu\text{sec}$ , the response is characterized by local bulging as previously noted with respect to Figure 38. Between about 140 and  $180 \mu\text{sec}$  the flexural response reaches the blade tip, resulting in a positive tip displacement. By  $300 \mu\text{sec}$  some of the high-frequency flexural waves are reaching the root of the plate. With reference to Figure 38, it should be noted that the plate response is now much more characteristic of a long beam-plate with relatively

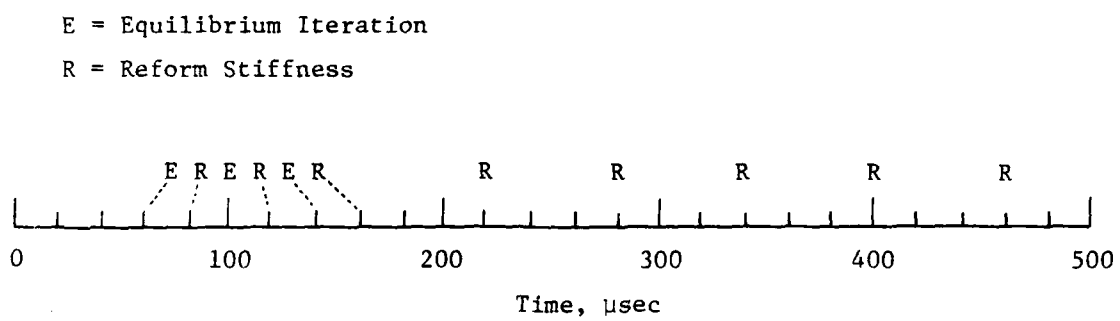


Figure 37. Stiffness Reformation and Equilibrium Iteration Strategy.

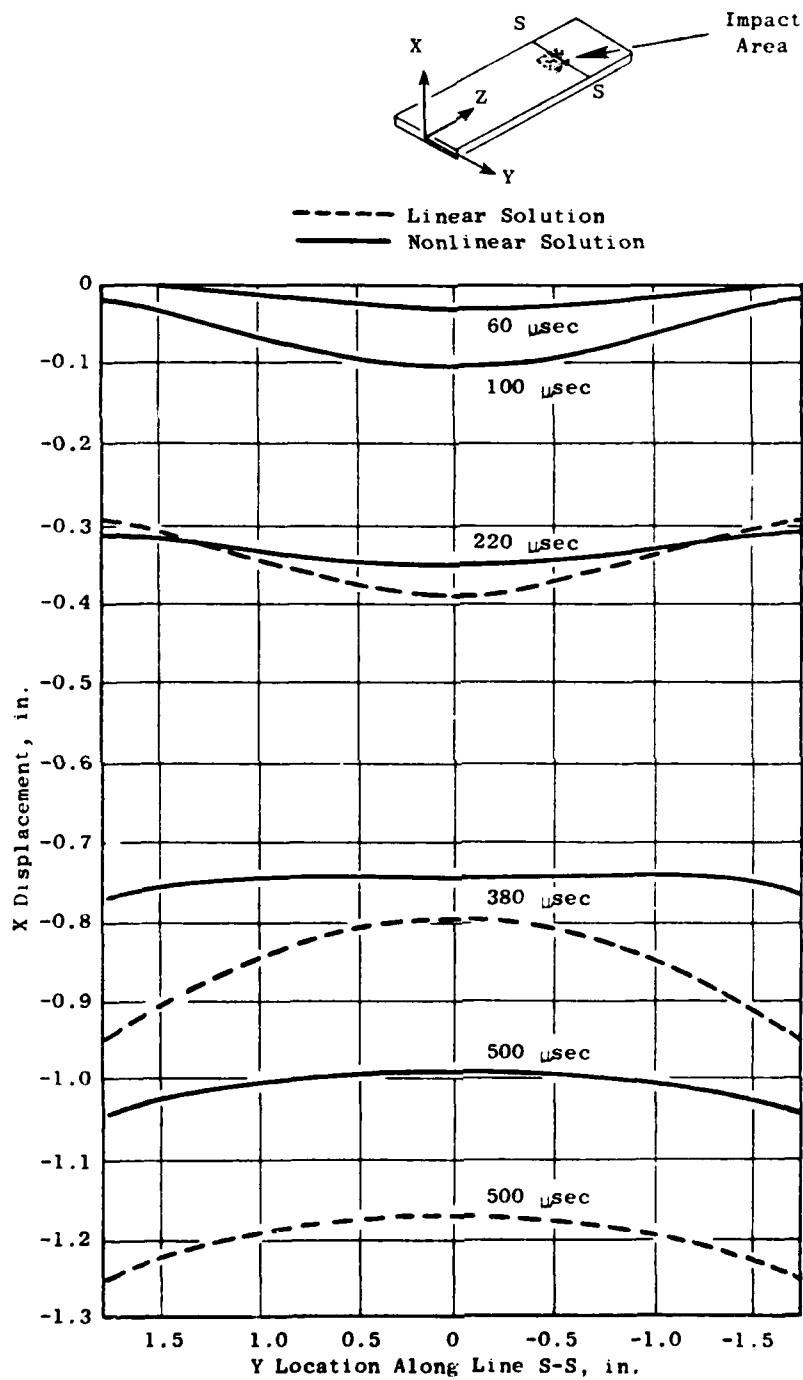


Figure 38. Lateral Displacement Along Chord-Line.

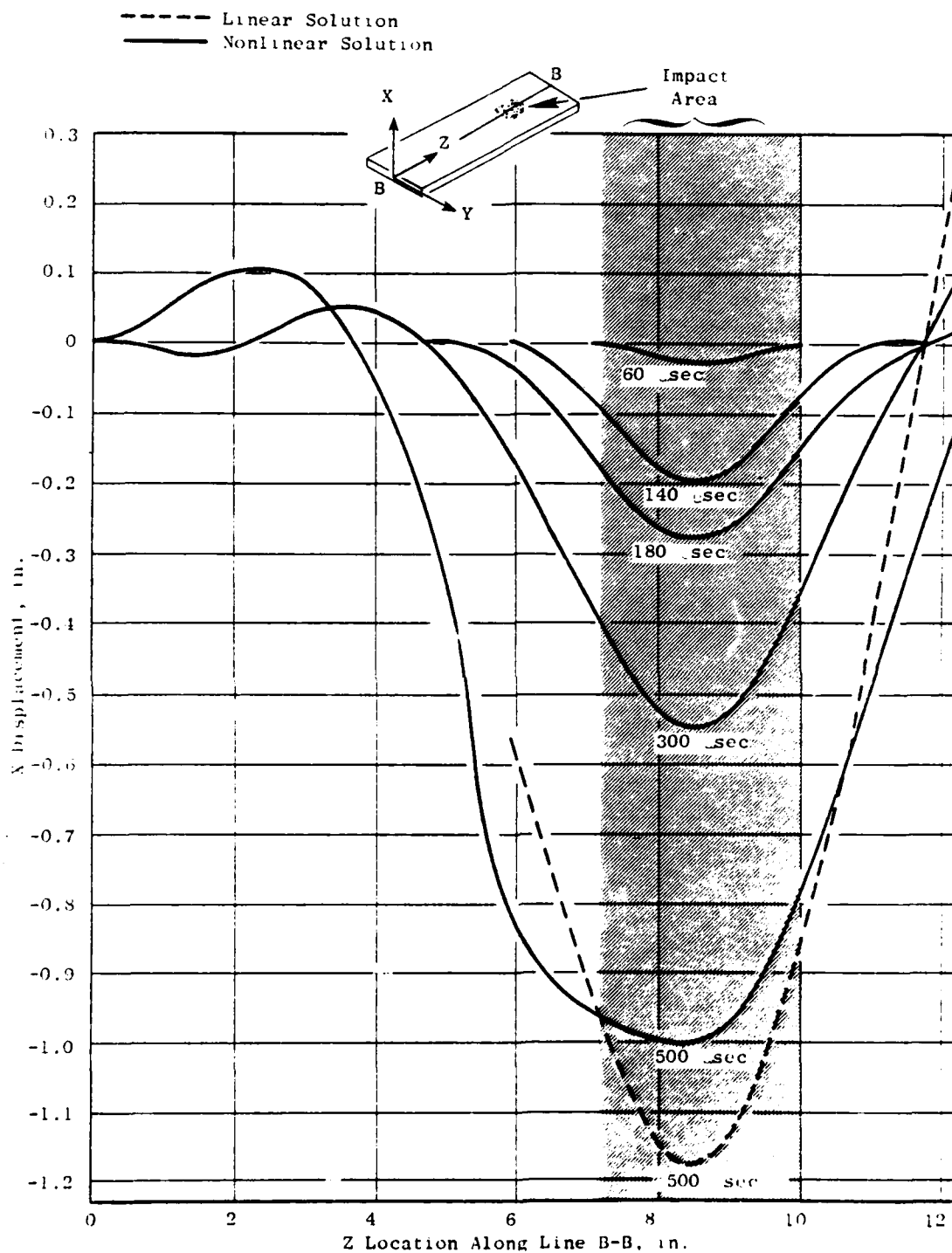


Figure 39. Lateral Displacement Along Centerline B-B.

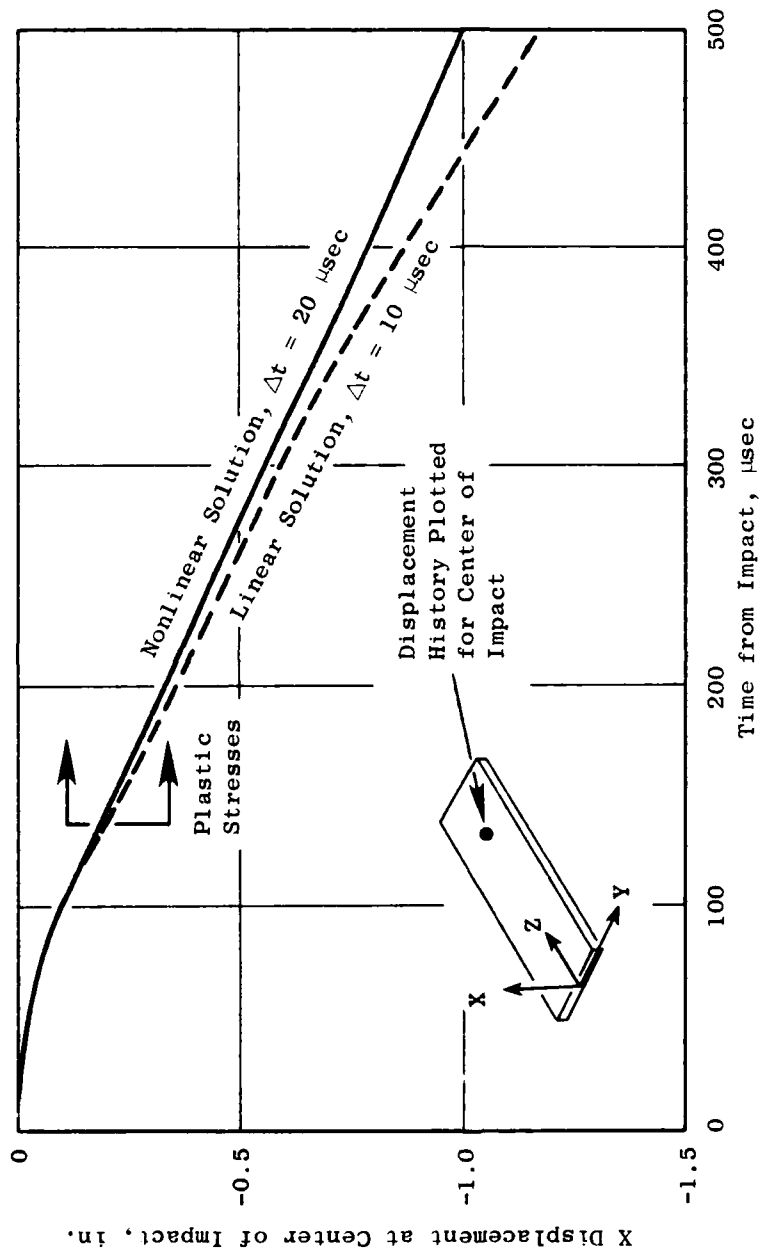


Figure 40. Lateral Deflection Under the Center of Impact.



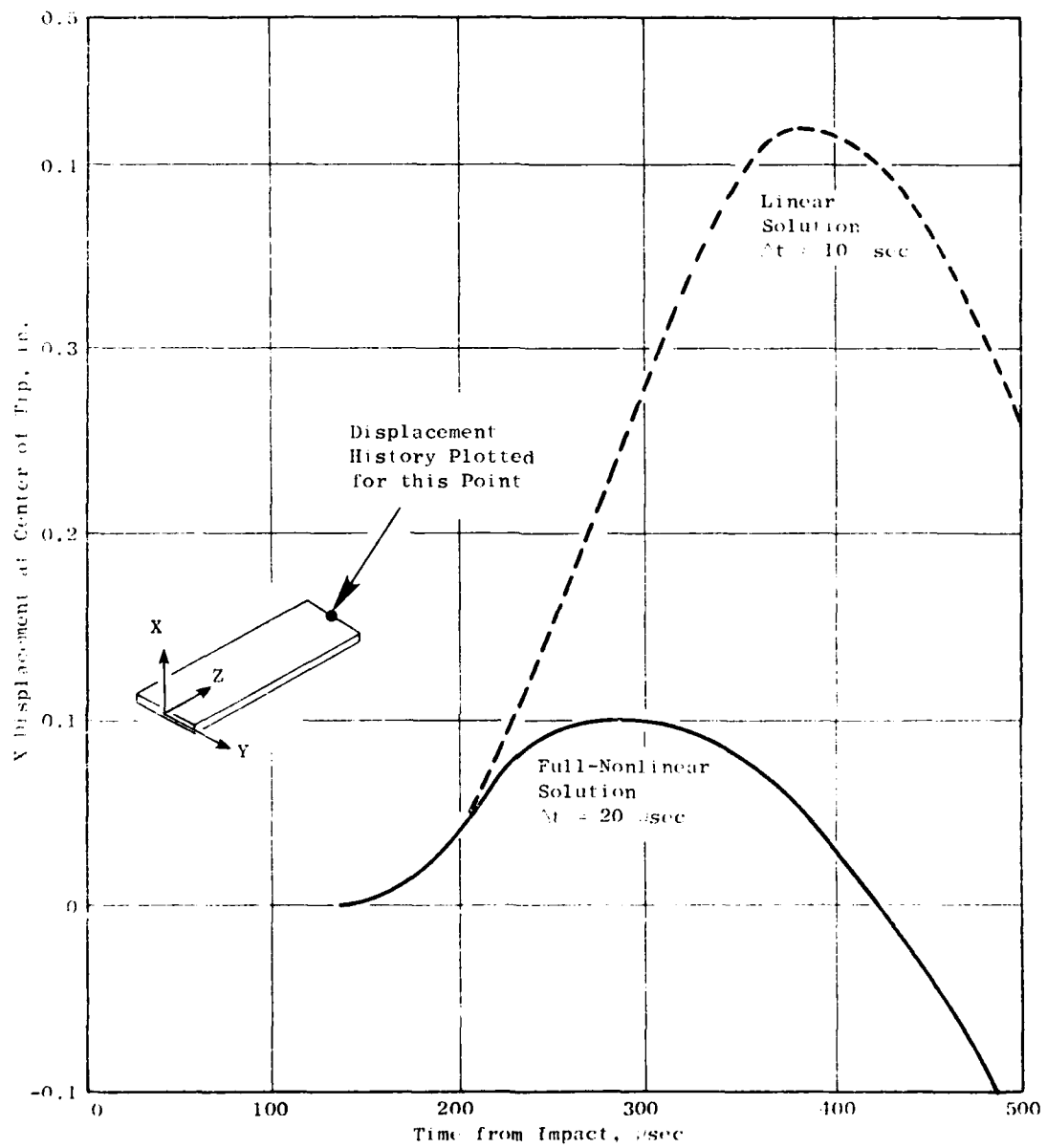


Figure 41. Lateral Tip Deflection.

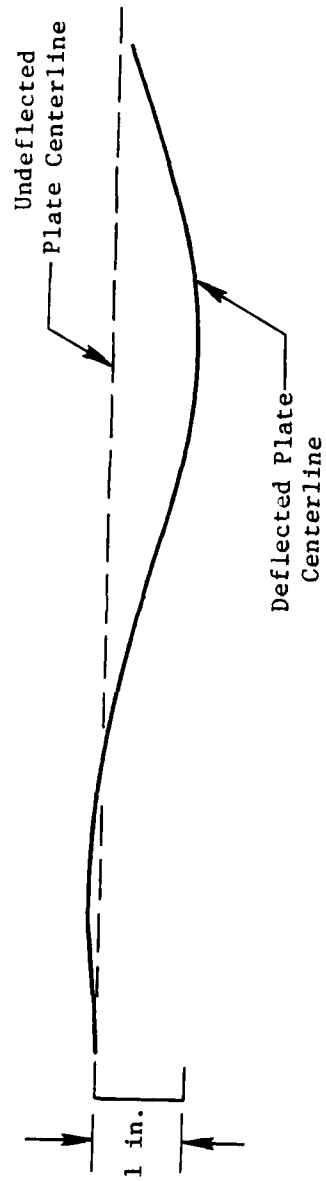


Figure 42. Deflected Shape Along Plate Centerline at  $t = 500 \mu\text{sec}$ .

constant displacement across the chord line. Finally, by 500  $\mu$ sec the lower frequency beaming modes are beginning to develop, and the tip deflection is now negative. For comparison, the linear solution at 500  $\mu$ sec is also presented as the dashed line. As pointed out with reference to Figure 38, the linear solution overestimates the flexural displacements of the plate because of the absence of the nonlinear, in-plane stiffness developed at large displacements.

Figures 40 and 41 help emphasize the nonlinear effects present in the blade-impact problem. In both of these figures, full nonlinear solutions are compared to linear solutions. Figure 40 presents the lateral-deflection history of the plate at the very center of impact. Figure 41 presents the tip-deflection history. In both cases the nonlinear response of the plate is evident in the form of additional in-plane stiffness resulting in smaller displacements with respect to the linear solution. The effect is particularly evident in the tip-displacement history of Figure 41 where the nonlinear effects result in a maximum positive tip displacement which is less than one-quarter that predicted by linear analysis. As indicated in Figure 41 plastic stresses appear after about 140  $\mu$ sec, but they remain extremely localized.

Finally, Figure 42 is presented to illustrate the actual shape of the deflected plate along the centerline at  $t = 500 \mu$ sec. The load has been completely applied by this time, and the presence of the first three cantilever-beam modes are already visibly present in the figure.

The analysis was refined and then extended from the time frame of the load application to include the longer term response of the plate. With respect to refining the previously discussed analysis, two items should be mentioned. First, a 10- $\mu$ sec time step was used to solve the problem from 0 + 500  $\mu$ sec and compared to the solution using a 20- $\mu$ sec time step. Sampling of pertinent results indicated that the reduction in the time step decreased maximum membrane stresses on the order of 10% while increasing the maximum positive tip displacement of the blade (that is opposite the impact-loading direction) by approximately 30%. The spatial distribution of membrane stresses under the load was also smoothed out using the smaller time step. In addition to this comparison, the number of Gauss points used for numerical integration in the plane of the plate was also altered from a 3 x 3 configuration to a 2 x 2 configuration for the sake of comparison. While the 3 x 3 set of Gauss points resulted in extreme discontinuities in stresses between elements, the 2 x 2 scheme provided very smooth and well-behaved distributions. Zienkiewicz also notes in his text<sup>11</sup> that lower order forms of Gaussian integration may sometimes be more appropriate in terms of stress distributions. As a result, it is recommended that a 2 x 2 scheme of Gaussian integration be used in the plane of the plate and three Gauss points through the thickness.

An indication of some of the stress-response behavior observed in this analysis is displayed in Figures 43 and 44. These plots focus upon the nonlinear membrane stresses generated in the plate during impact. These are effects that would not be predictable with a linear analysis. Figure 43 illustrates the  $\sigma_{zz}$  membrane stress generated near the center of impact

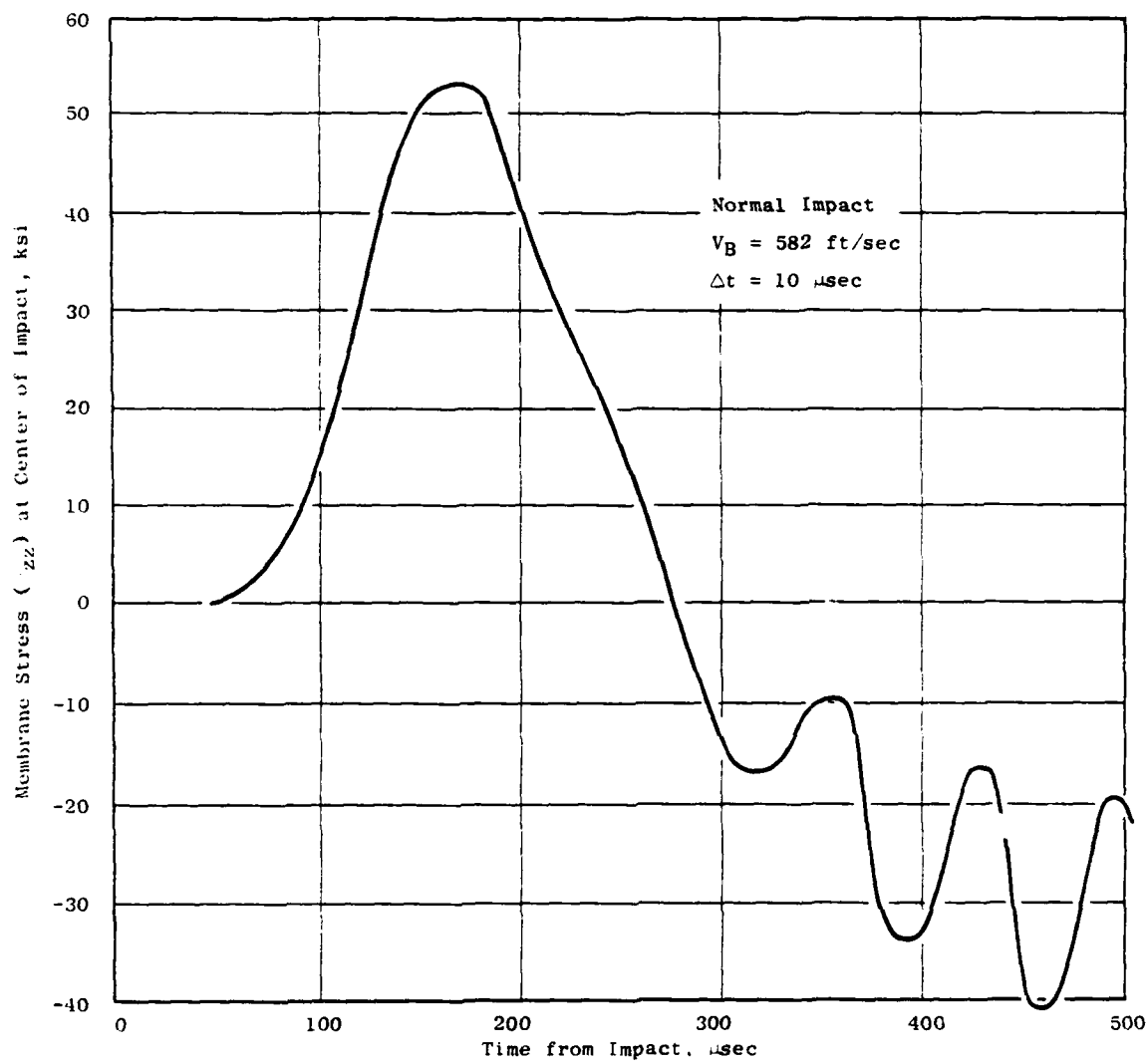


Figure 43. Membrane Stress History at Center of Impact.

Normal Impact

$V_B = 582 \text{ ft/sec}$

$\Delta t = 10 \text{ } \mu\text{sec}$

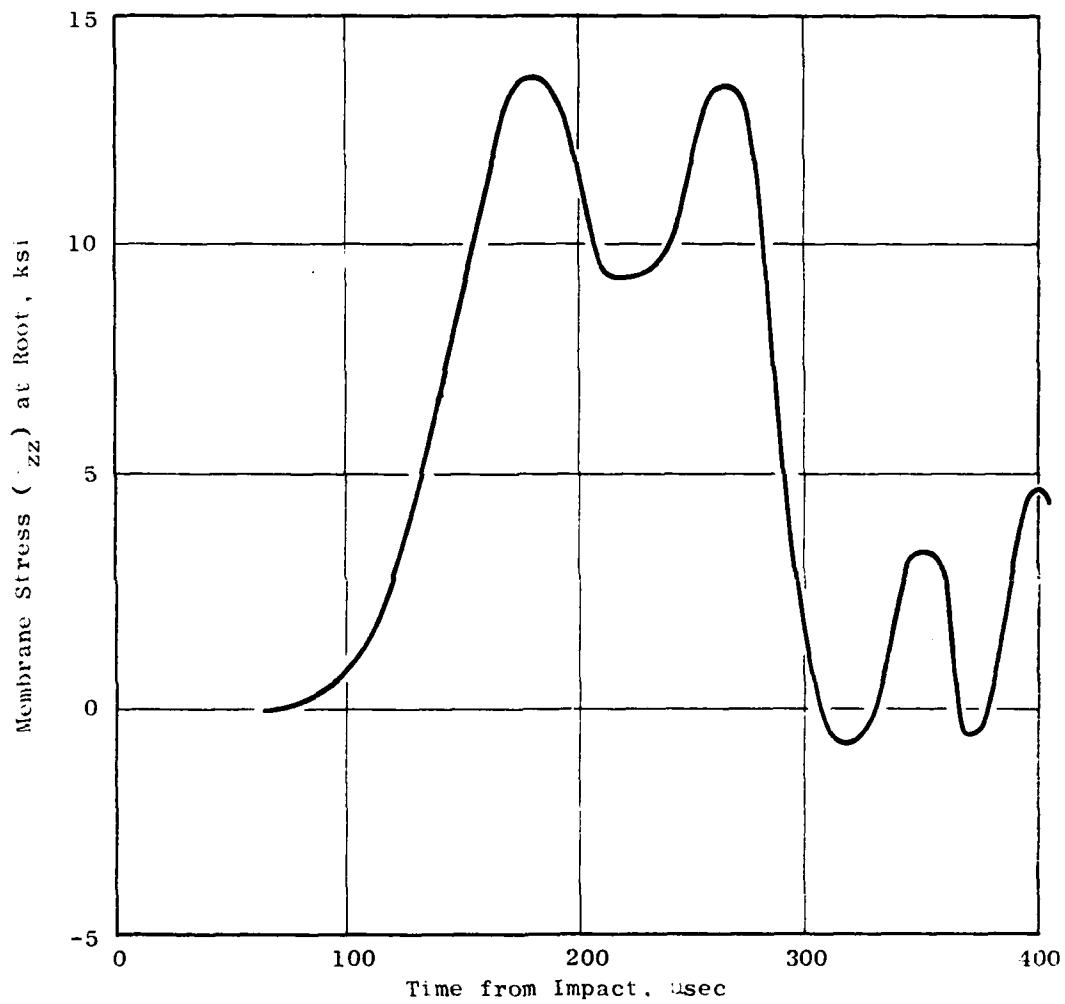


Figure 44. Membrane Stress History at Root.

as a function of time. As can be seen, before approximately 60  $\mu$ sec there is no membrane stress response since the displacements in the area of the impact are less than the plate thickness, and linear bending theory applies. However, shortly thereafter, as the displacement continues to grow, a large tensile membrane stress begins to develop as a result of nonlinear effects. This stress passes through a maximum of over 50 ksi before decaying and beginning to reflect the higher frequency response associated with reflections from the plate end and root. This pulse in the membrane stress spreads and attenuates as it propagates down the length of the plate. By the time it reaches the root area, the magnitude is significantly reduced; this can be seen in Figure 44 which plots the  $\sigma_{zz}$  membrane stress history at the Gauss point nearest to the centerline at the root. The maximum stress here is approximately 13 ksi. Figure 45 plots the centerline displacements of the plate at three different time intervals where plastic action was occurring. At 0.320 msec the yielding is local to the impact area. At 1.15 msec yielding begins to occur at the root. This yielding seems to be associated with the arrival of a flexural stress wave associated with the third natural bending frequency of the plate. Unloading then occurs at the root, and yielding eventually reappears in this area near the maximum tip displacement reached at approximately 6.2 msec.

#### 7.4.2 Comparison Between First- and Second-Level Analyses for Normal Impact

Further refinement relative to the material parameters was accomplished, and a comparison between NOSAPM and COMET (second-level analysis) was made for normal impact. Material data, based upon tensile tests carried out at UDRI at various strain rates in Task IV-A, were used in the analyses. Previous experience indicates that strain rates in these impacted plates will be in the range of 375 in./in./sec. With this prediction and the UDRI test data, the following material properties were used in the analysis:

$$E_1 = 17.3 \times 10^6 \text{ psi}$$

$$E_2 = 0.376 \times 10^6 \text{ psi}$$

$$\nu = 0.3$$

$$\sigma_Y = 191 \text{ ksi}$$

$$\rho = 0.158 \text{ lb/in.}^3$$

In this case  $E_1$  is the linear elastic Young's modulus while  $E_2$  is the tangent modulus which approximates the material response after yielding has occurred. The same NOSAPM finite-element model was used for this analysis as in the previously described normal-impact analyses. The pressure over the impact area was calculated to be 7100 psi and occurred 90  $\mu$ sec after the beginning of impact. The total impact event was assumed to last 430  $\mu$ sec.

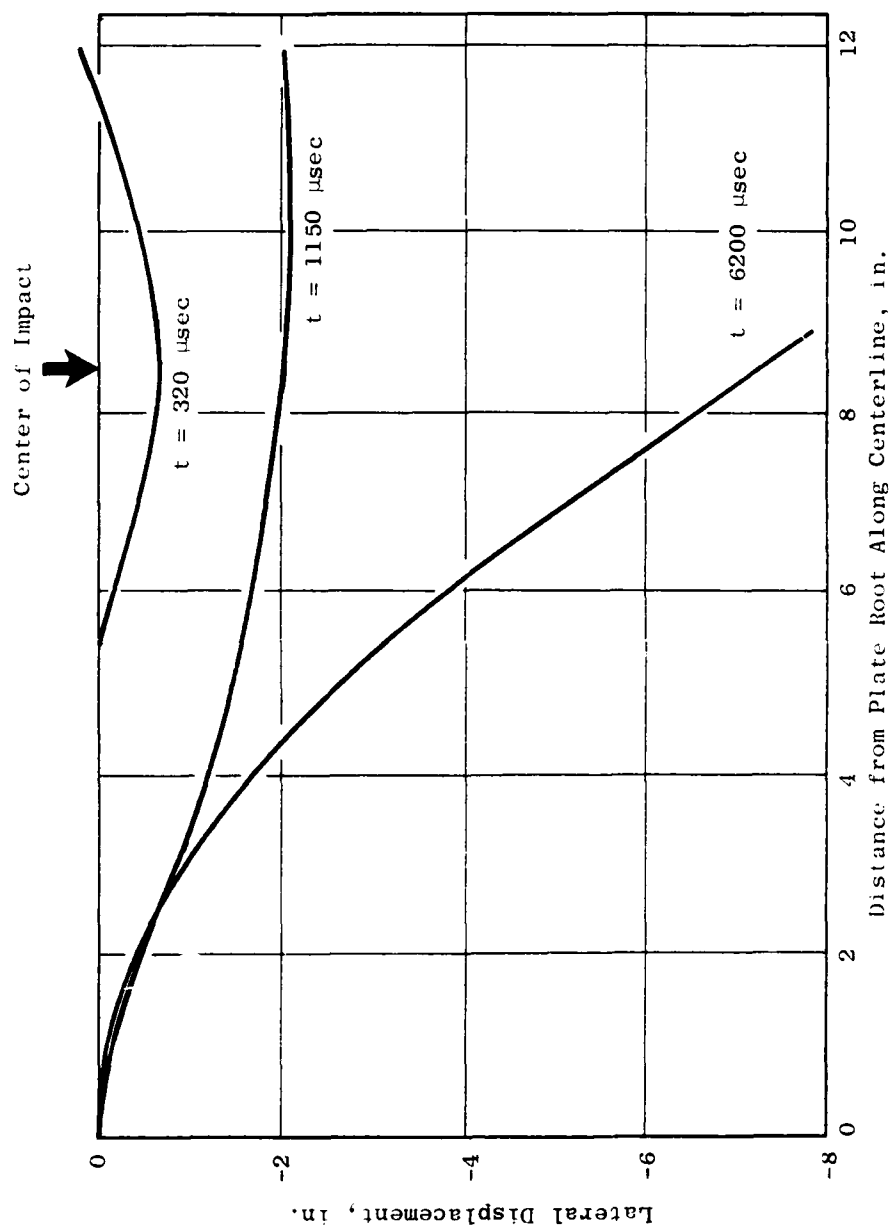


Figure 45. Large Displacements.

For the Level 1 analysis, a 10- $\mu$ sec time step was used. For the Level 2 analysis, a 1- $\mu$ sec time step was used. The two results agree quite closely over the time frame examined in spite of the fact that the elements and numerical techniques are quite different. Unfortunately, the Level 2 analysis did not prove to be substantially less expensive than the Level 1 analysis for the computing strategies incorporated. In an effort to further test the choice of time step used in the Level 1 analysis, the same problem was studied over a reduced time frame with a 1- $\mu$ sec time step. At this time step there was virtually no visible difference between the 10- $\mu$ sec and 1- $\mu$ sec solutions. Perhaps a more pertinent convergence test in this case is a comparison of the membrane stress in the impact area since the propagation of this stress is at near the speed of sound in the plate and, hence, takes place very quickly. Over the time frame studied, the maximum membrane stress under the load was on the order of 6% different for the 1- $\mu$ sec time-step strategy compared to the 10- $\mu$ sec investigation. Thus, although improvements in the membrane-stress distributions can be made by reducing the time from 10  $\mu$ sec to 1  $\mu$ sec, one must trade off this benefit against cost considerations.

#### 7.4.3 Comparison Between First-Level Analysis and Experimental Data for Normal Impact

Two normal-impact correlations were carried out with experimental data obtained by UDRI in Tasks III and VI. In both cases the impact angle was 90°; as a result, a noninteractive impact pressure characterization (based upon previously reported principles) was applied. The correlation obtained in these two examples indicates the success of NOSAPM in predicting displacement histories and deformed shapes both during the initial phases of impact when local deformation governs as well as time periods extending to maximum tip-displacement intervals. It must be noted, however, that achieving maximum-tip-displacement results is much more expensive.

The geometries of the two normal-impact problems under consideration here are characterized in Figure 46. All dimensions associated with the two tests are identical except for the plate thickness; that is 4.27 mm in the first case and 2.21 mm in the second case. The impact masses and velocities are also different. The first impact discussed involved an impact mass of 100 g and a velocity of 177.4 m/sec. The second test used a mass of 82.6 g impacting at 103.8 m/sec. The finite-element model illustrated in Figure 47 has been discussed previously. The impact area in this model is comprised of Elements 20, 21, 24, and 25. Based upon University of Dayton Research Institute data, the Young's modulus for the 8-1-1 titanium used in this experiment was shown to be 119 GPa ( $17.3 \times 10^6$  psi) with a secondary modulus of 2.59 GPa (385 ksi). The material density used in the analysis was 4.38 g/cm<sup>3</sup> (0.158 lb/in.<sup>3</sup>). Although strain rates of 200 to 300 sec<sup>-1</sup> have been measured and predicted analytically during impact response, preliminary analyses indicated that the most substantial yielding in these tests occurs at strain rates of the order of 4 sec<sup>-1</sup>. As a result, the 1.13 GPa (164 ksi) yield stress applied in this analysis reflects such a strain rate. The results



NOTE: Dimensions are cm.

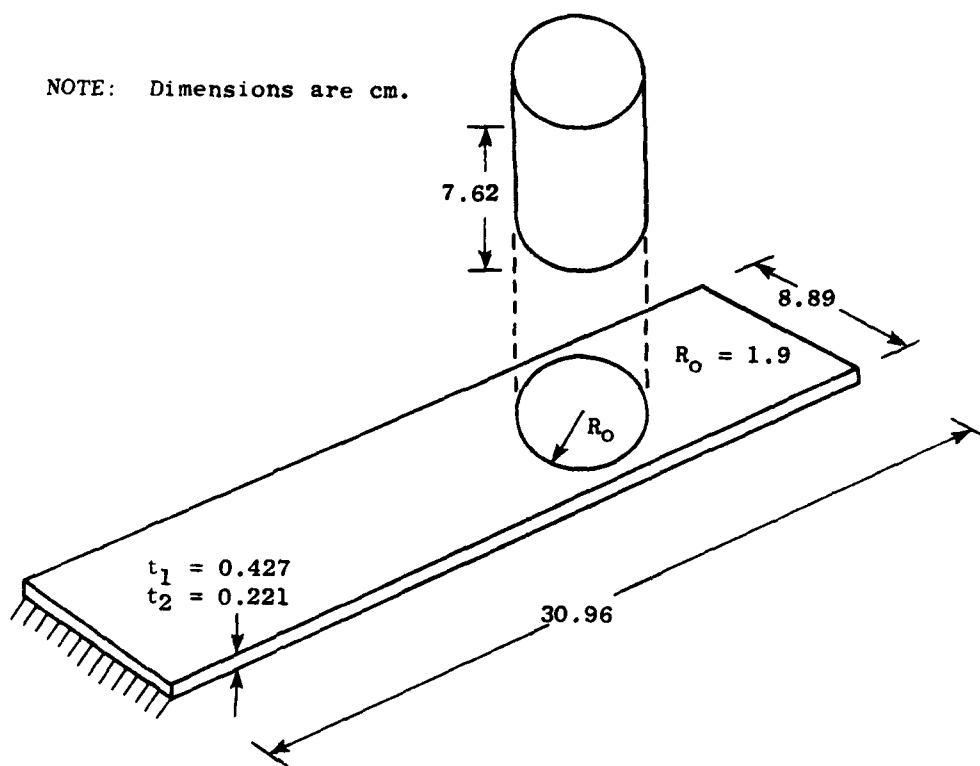


Figure 46. Impact Geometry.

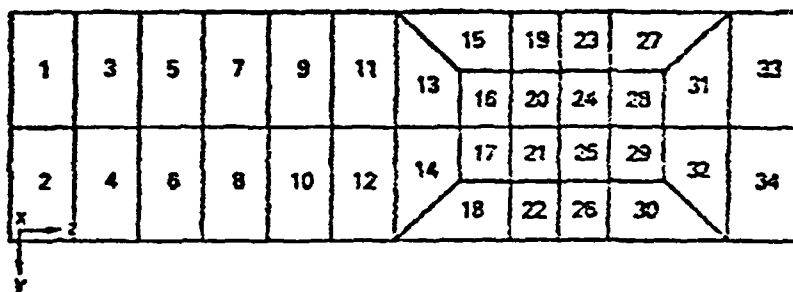


Figure 47. Finite-Element Model.

presented in Figures 48 and 49 were obtained with a 2 x 2 Gauss point array in the plane of the plate and four Gauss points through the thickness. Stagliano and Mentel<sup>12</sup> feel that four Gauss points are necessary through a thin plate in order to accurately describe plastic deformation incurred during large-displacement bending. Results from our work using both three and four Gauss points through the thickness are inconclusive in this respect.

Figure 48 compares the history of the tip-deflection prediction analytically with the data collected using high-speed photography during the actual test. As can be seen, the correlation is reasonably good, especially when one considers the extreme nonlinearity of the problem. The analysis predicts larger tip deflections than those actually measured during the time frame between 1 and 3 msec after impact initiation. It underpredicts the maximum deflection by only about 13%. The discrepancy is most likely a reflection of the approximations made in describing the load history and the "discretization" applied to model the plate.

During the second normal-impact test considered here (Shot 40055), attention was focused upon the local response of the plate. Moiré fringe techniques were used to get a detailed description of the local deformation during the impact response (refer to Figure 25). The plate impacted in this test had the same planform dimensions but was only 2.21 mm thick. The projectile mass was 82.6 g, and the impact velocity was 103.8 m/sec. Application of the same principles previously discussed with respect to modeling the impact loading results in a peak pressure of 14.0 MPa at 150  $\mu$ sec and a total impact load duration of 730  $\mu$ sec. Figure 49 compares the results of this test with analytical predictions. The displacement of the centerline of the plate is plotted for two different times after impact initiation: 150 and 460  $\mu$ sec. The analysis overestimates the local maximum of the plate response by about 30% at 460  $\mu$ sec after the impact initiation. The most likely reason for this overestimation is inaccuracy in the load model. The simple approach used herein to obtain impact pressures is based upon the assumption that the target is rigid. In the case of a thin plate this is, of course, not true. The plate develops substantial structural velocities during an impact, and this response will reduce peak pressure loads and increase the duration of the impact. In addition, although the impact areas over which the pressure loads were applied in the analysis was roughly the cross-sectional area of the projectile, it has been observed<sup>6</sup> that, in a normal impact, there are substantial pressures over an area as much as four times the cross section of the projectile. Proper accounting of both of these effects would tend to reduce the predicted maximum local displacement.

#### 7.4.4 Oblique-Impact Analysis

The following discussion pertains to the results obtained from the combined program representing the UDRI loading model and NOSAPM response model. An example of the pressure calculation for a 24.4° impact on a flat plate with a bird velocity of 15,240 in./sec is presented in Figure 50. The

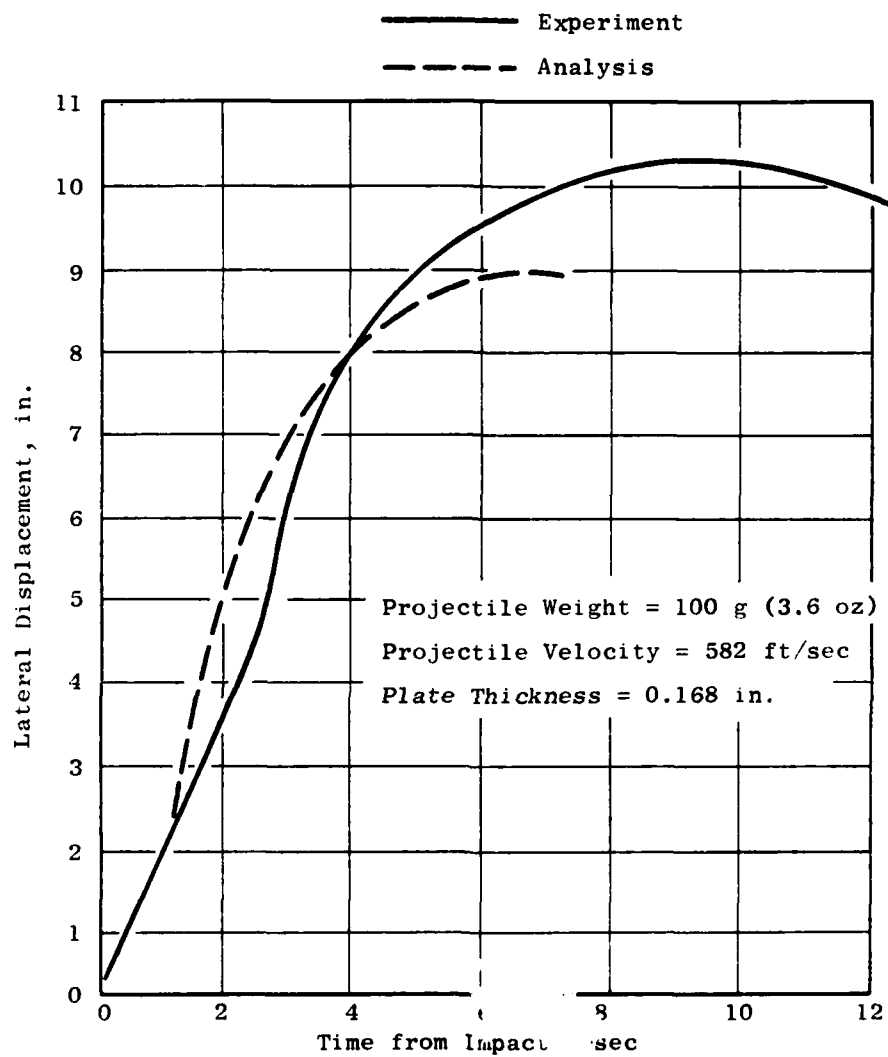


Figure 48. Tip-Displacement History: NOSAPM Predictions Vs. Test for Simulated-Bird Impact.

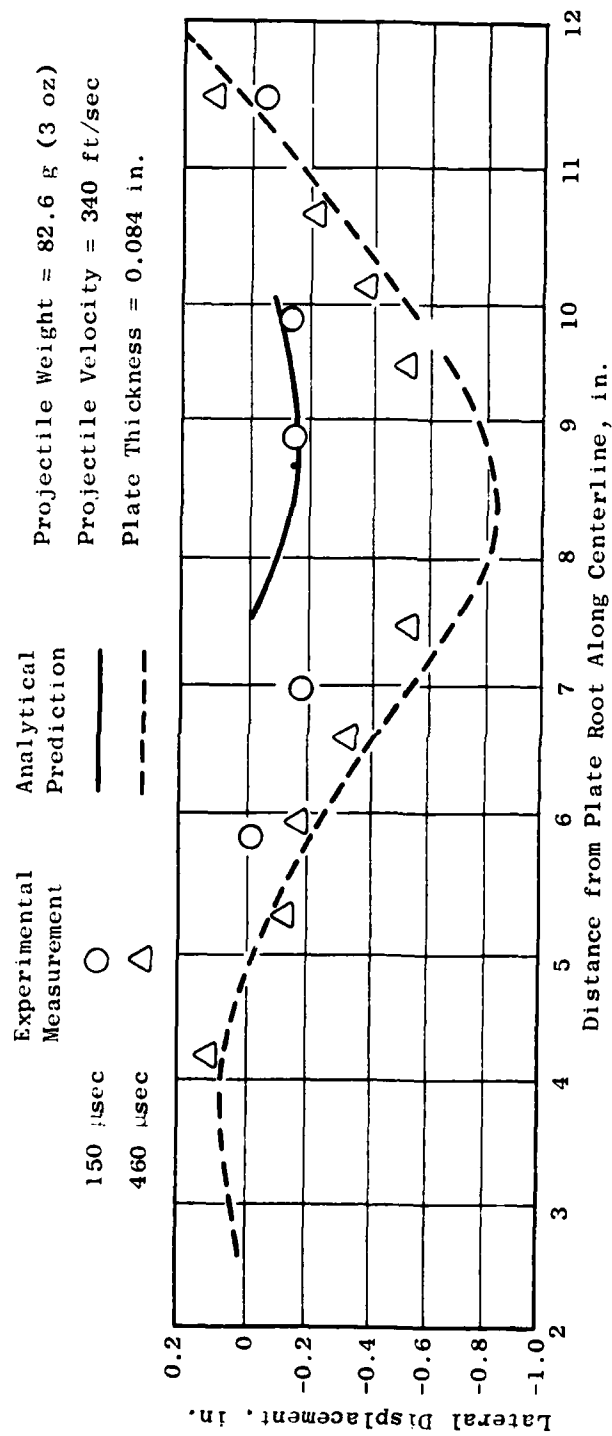


Figure 49. Deformed Geometry Profile; NOSAPM Prediction Vs. Test for Simulated-Bird Impact.

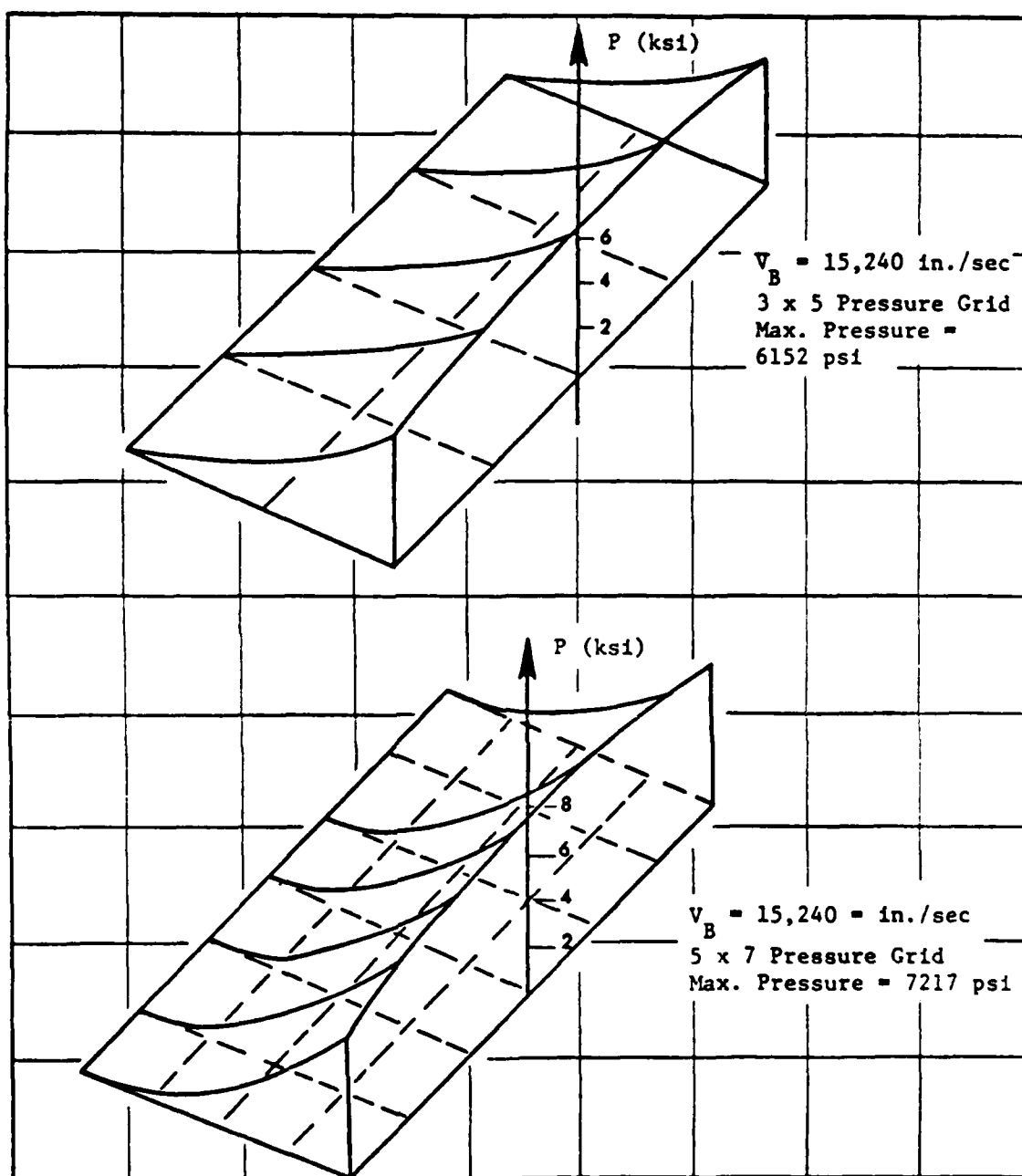


Figure 50. Pressure Distribution for  $\theta = 24.4^\circ$  Impact on a Flat Plate.

density of the substitute-bird material used in the analysis was 0.03567 lbm/in.<sup>3</sup> The computed pressure distributions were symmetric about the centerline in the span direction during the initiation of impact, as would be expected.

The maximum response occurred at the leading edge and decayed to zero toward the trailing edge. With 35 pressure nodes, the maximum pressure at the leading edge was 7217 psi, almost exactly twice the momentum-balance pressure:

$$(\rho/g)V^2 \sin^2 \theta = [0.03567/32.2(12)](15240)^2(\sin 24.4^\circ)^2 = 3659 \text{ psi} \quad (22)$$

This, in turn, means that the momentum transfer is correct, at least at time zero. The predicted pressures are somewhat lower if a coarser grid is used to define the pressure distribution. Figure 51 shows the impact geometry and pressure distribution and Figure 50 shows the details of the pressure distributions for two pressure-grid sizes.

Solution checks were also run on the following operations; in all cases, the results were positive.

- Operation of load interface with centrifugal loads.
- Validity of calculation of equivalent nodal loads from updated pressure data.
- Updating of pressure data during impact.
- Termination of impact loading.

#### 7.5 COMET MODELING AND OBLIQUE-IMPACT ANALYSIS

The loading model developed by CR&DC (described in Section 5.4.5 of this report) has been incorporated into the COMET response program, and initial checks have been made. This loading model takes account of shock waves and other mechanisms, described in Reference 6, while treating the bird/blade relationship interactively. The approach automatically takes account of changes in blade angle during impact and of lengthening of the impact duration by the blade displacement.

Results using this routine are presented in Figures 52 through 55 for a 3/8-in. thick aluminum blade model extending from R = 10 in. to R = 20 in. The blade chord extends 5 in. The bird length is 3 in., and the impact region extends from R = 15.5 in. to R = 18.5 in. The analysis was run using 66 elements and 66 nodes at 1-in. spacing with a time step of 0.000002 sec for 200 times steps.

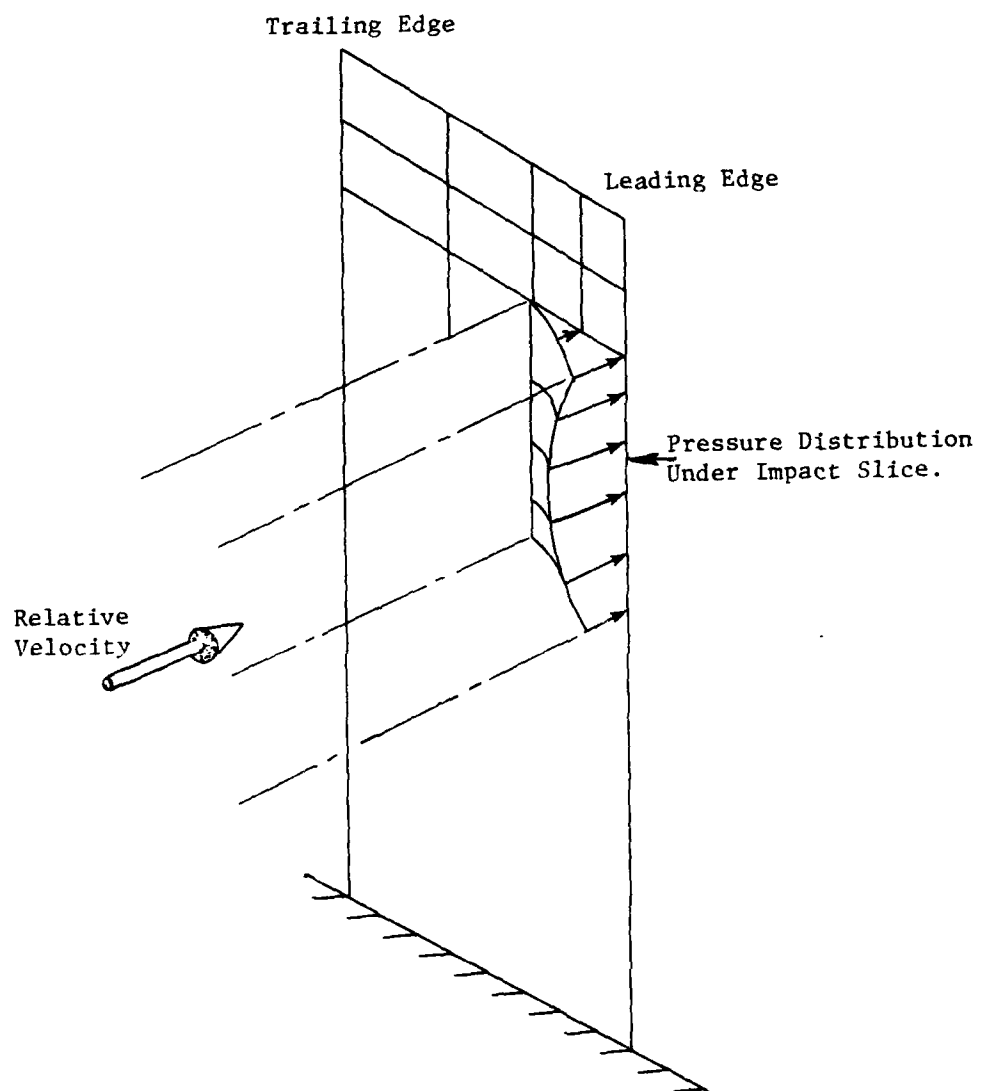


Figure 51. Impact Geometry and Pressure Distribution.

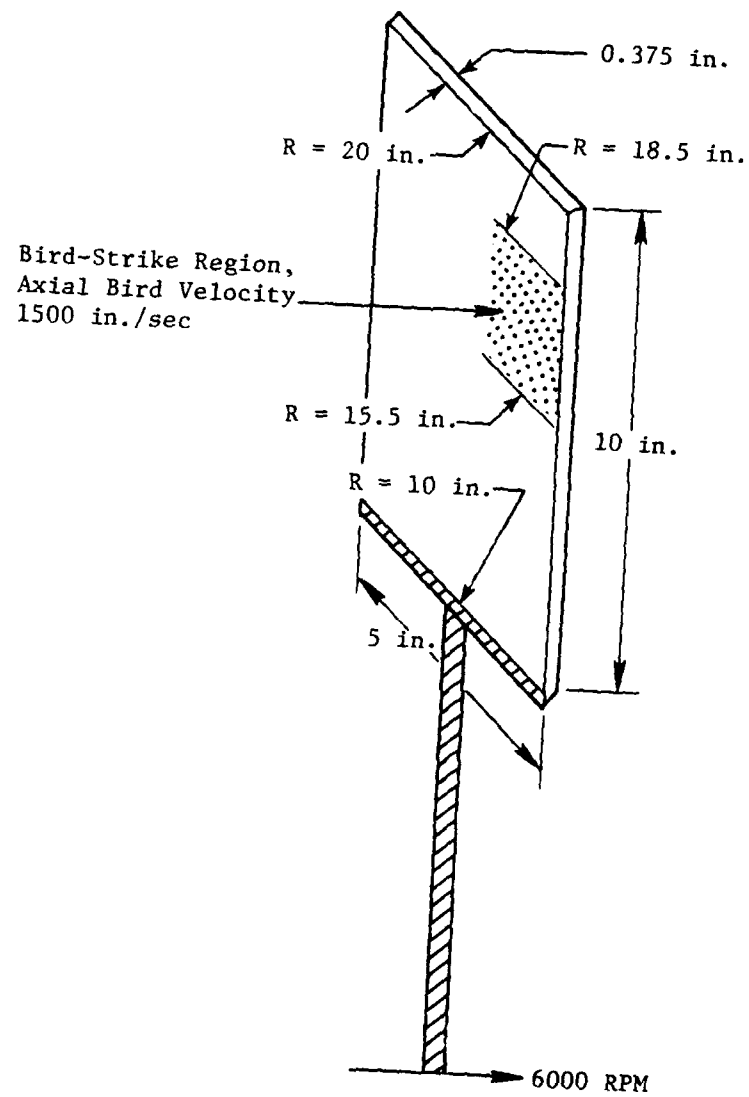


Figure 52. Model of Blade/Bird Impact for COMET Analysis.



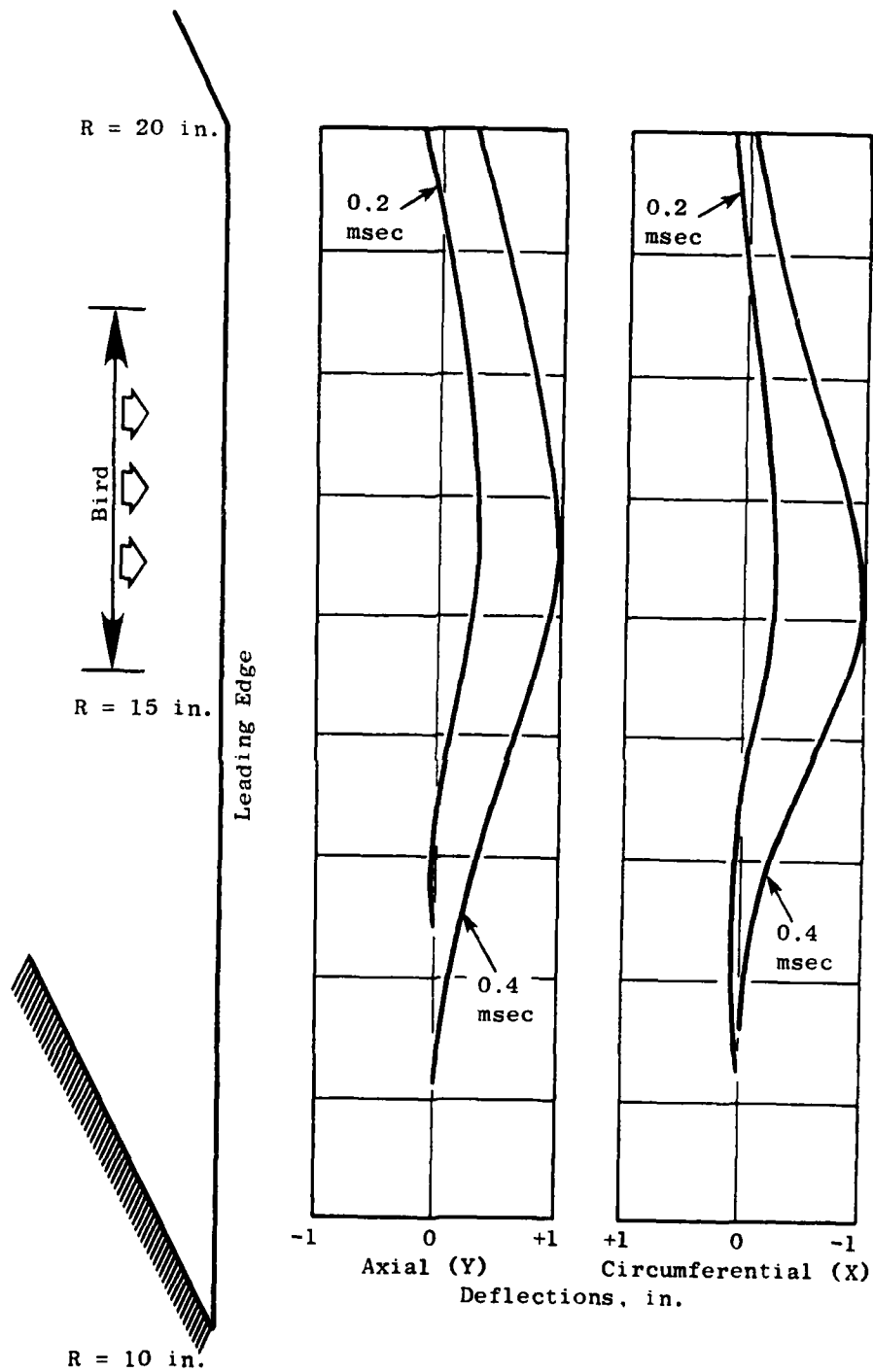


Figure 53. Deflections at Leading Edge.

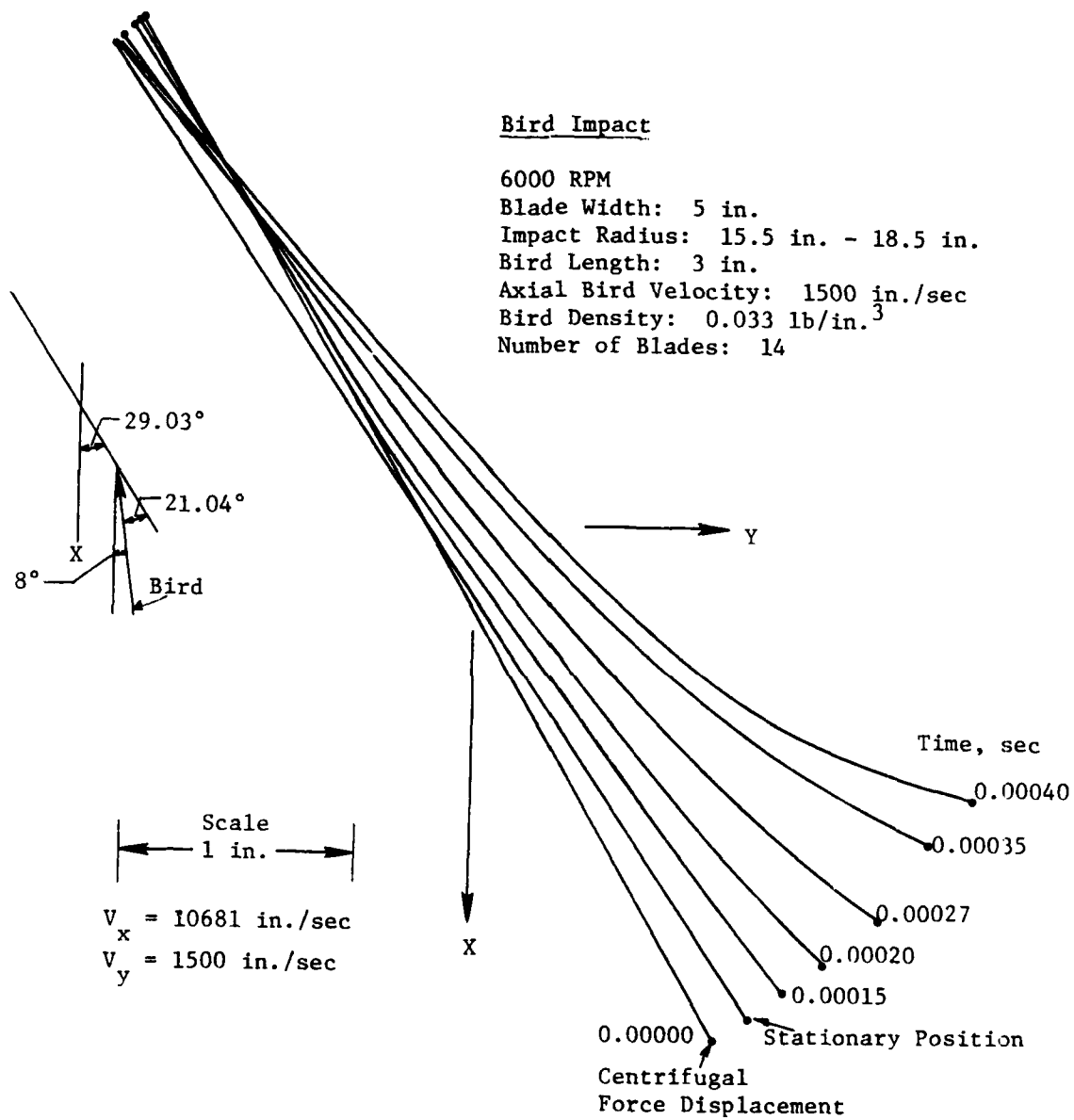


Figure 54. Deflections at Nodal Positions Along Chord Line at 17-in. Radius.

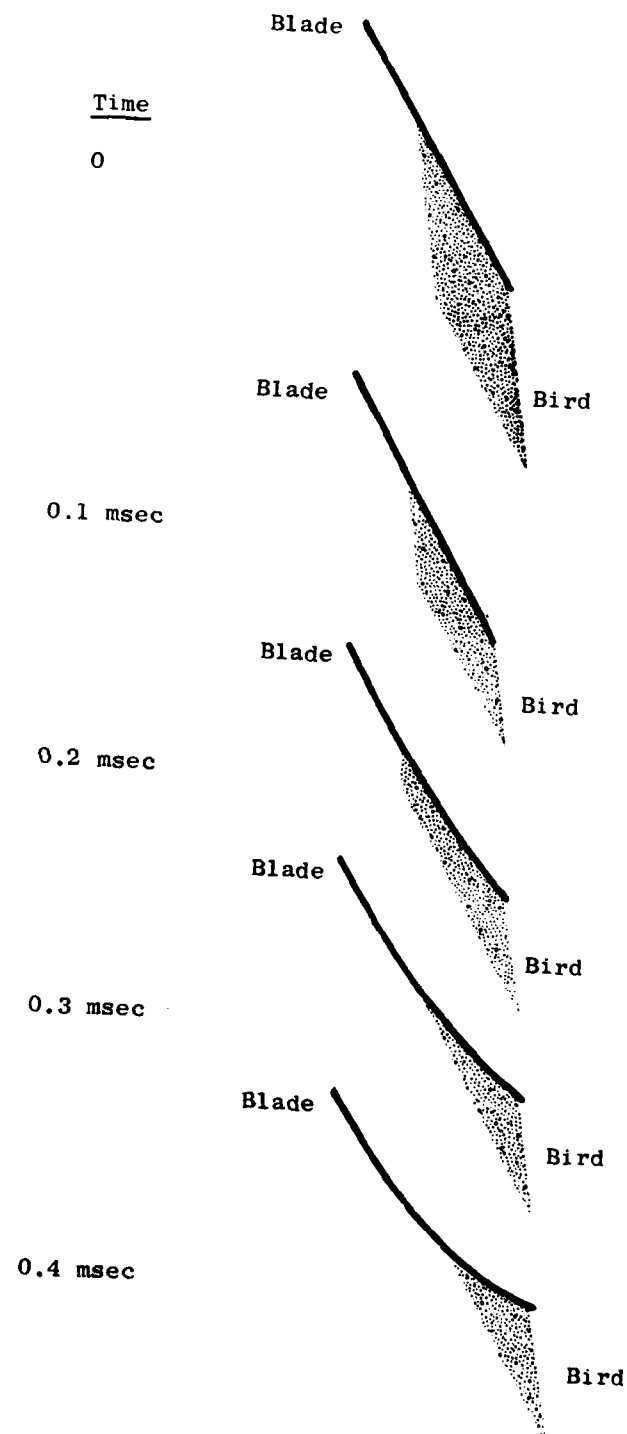


Figure 55. Interaction of Blade and Bird Along Chord at 17-in. Radius.

Lateral deflections at the leading edge at 0.0004 seconds reached about an inch in the axial and the circumferential directions. The lateral deflections were maximum in the impact region and were lower at the tip.

The deflection at the 17-in. chord line show that initially the centrifugal forces rotate the blade a small amount into the plane of rotation. Subsequently the bird-impact forces bend the blade back substantially.

The interaction of bird and blade is shown in Figure 55. It is evident that blade deflection extends the duration of impact substantially. The nominal impact time is 0.000278 sec (3 in. bird length and 10,786 in./sec bird relative velocity), but the figure shows the impact is still in progress at 0.0004 sec due to blade flexing.

The peculiar-shape bird (highly angled) shown in the figure is the result of a need by the University of Dayton to model the front of the bird parallel to the blade. This has been followed in the present COMET version; however, the programming in COMET can permit the front and back of the bird to have other configurations.

## 8.0 TASK VI - STRUCTURAL ELEMENT TESTS

### 8.1 INTRODUCTION

The work of Task VI, "Structural Element Tests," is concerned with performing nonrotating bench impact tests on specimens ranging from simple elements to real blades. The simple elements, such as beams and plates, will be tested with progressive introduction of airfoil geometric parameters to validate experimentally the analytical predictions of Tasks V and VIII. The purpose of Task V is to derive parametric relationships describing the changes in dynamic structural response as a function of material and geometric features. The purpose of Task VIII is to derive criteria for predicting blade FOD tolerance. These criteria will be formulated to make full use of the transient dynamic analysis and experimental results obtained from other tasks of the program.

### 8.2 DESCRIPTION OF TESTS

The materials being investigated in the structural element tests include 403 stainless steel, 8-1-1 titanium, and the boron/aluminum composite. The geometry of the test specimens is arbitrary for the purpose of checking out the analytical predictions of Tasks V and VIII; however, the geometry and thickness were selected to be typical of actual blades of the same material, at the 50% span location along the leading edge.

The impactors for the study include 2- to 3-ounce birds, 1.5-pound birds, and 3-inch ice cylinders. Microballoon gelatin material is used to simulate real birds. The impact velocities were selected to cause no damage, threshold damage, and severe damage. The impact angles selected were arbitrary; however, they will correspond to those of actual blades at the 30 and 70% span locations.

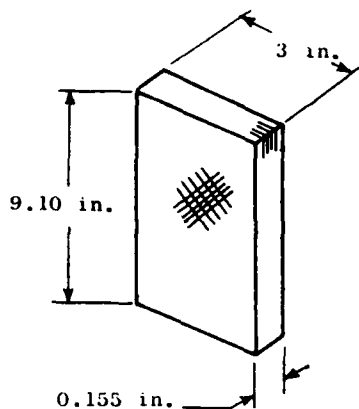
The blade parameters being investigated include aspect ratio, thickness/chord ratio, shape (constant thickness, wedge, and blade-like), camber, twist, and shrouds.

#### 8.2.1 Composite Structural Specimens

The composite specimens include flat panels, airfoil-like cross sections, cambered shapes, cambered and twisted shapes, and real APSI blades. The fabricated composite specimens are shown in Figure 56.

#### 8.2.2 Metal Structural Specimens

The metal specimens include flat plates, airfoil-like cross sections, cambered shapes, cambered and twisted shapes, and real J79 and F101 blades.



Cross-Ply B/A1

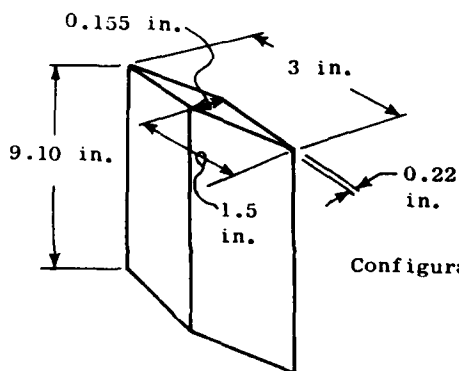
(0/22/0/-22)

Configuration (1) - Blade Type Aspect Ratio Panel

Configuration (2) - Same as (1), Except Length Reduced by 1/2

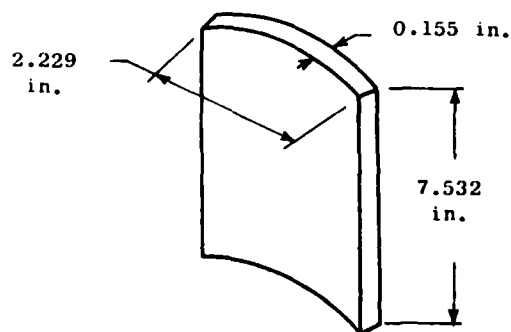
Configuration (3) - Same as (1), Except Thickness Reduced by 1/2

(a) Configurations 1, 2, and 3



Configuration (5) - Airfoil-Like Cross Section Panel

(b) Configuration 5



J79 Specimen Die Used and

Aspect Ratio Same as APSI

Configuration (6) - Cambered Panel

Configuration (7) - Same as (6), Except Twist Introduced After Forming

(c) Configurations 6 and 7

Figure 56. Task VI B/A1 Composite Test Specimen Configurations.

The titanium material was selected for a baseline series of tests, and the stainless steel was selected for a supplementary series of tests. The baseline series of tests on the fabricated titanium specimens considered all geometrical effects except camber and twist. It has been established that camber and twist are not cold-formable on the titanium specimens and that these parameters could be incorporated only through hot-forming or machining operations. Therefore, camber and twist were investigated utilizing the stainless steel cold-formed specimens.

### 8.3 DISCUSSION

All of the impact tests for Task VI have been completed, and analyses of the strain data and of the displacement responses recorded on high-speed movies are underway. Table 14 describes some of the tests performed on real blades. During the testing of the fabricated structural specimens, the different geometry effects (i.e. aspect ratio, thickness/chord ratio, etc.) were introduced in a different sequence for the titanium and steel specimens so that any synergistic effects that might exist could be accurately assessed.

The strain data will be formatted to obtain strain- and strain-rate-versus-time plots for direct comparison with the predictions.

Detailed analysis of the high-speed movies is being conducted to obtain the displacement-versus-time profiles for comparison with the predicted displacement response.

Figures 57 through 59 show examples of the displacement, strain, and strain-rate responses that were obtained from a 3-ounce-bird, normal-impact test at the 70% span location on a 8-1-1 Ti plate-shaped specimen with a blade-like (F101) aspect ratio.

Table 14. Some Task VI Impact Tests Conducted on Real Blades.

Date	Shot No.	Mass (g)	Mass of 3-Inch Ice Cylinder to Impact Target	Velocity (ft/sec)	Description	Group No.	Span (%)	Angle (°)	Comments
12-06-79	2-0231	867.1	75.8	607	F101 Blade S/N KGA01582 Cantilever Mount 8-1-1 Ti	28	30	24.4	2.08-in. Deformation of Leading Edge; 2.56-in. Deformation of Trailing Edge. Unable to Determine Mass.
12-07-79	2-0232	686.5	147.8	326	J79 Blade S/N 1-3 Cantilever Mount Stainless	42	30	51.1	No Visible Damage. <u>No Dynafax Film.</u>
12-07-79	2-0233	716.1	135.7	315	APSI Blade S/N 068 Cantilever Mount B/Al	65	30	38.8	Severe Damage. Blade Broke Off at Mount.
12-10-79	2-0234	758.5	207.4	320	J79 Blade S/N 1-4 Cantilever Mount Stainless	42	30	51.1	No Visible Damage.
12-10-79	2-0235	688.6	158.4	438	J79 Blade S/N 1-4 Cantilever Mount Stainless	42	30	51.1	5.8-in. Deformation on Leading Edge; 6.1-in. Deformation on Trailing Edge. Projectile Broke Up Between Slicer and Impact.



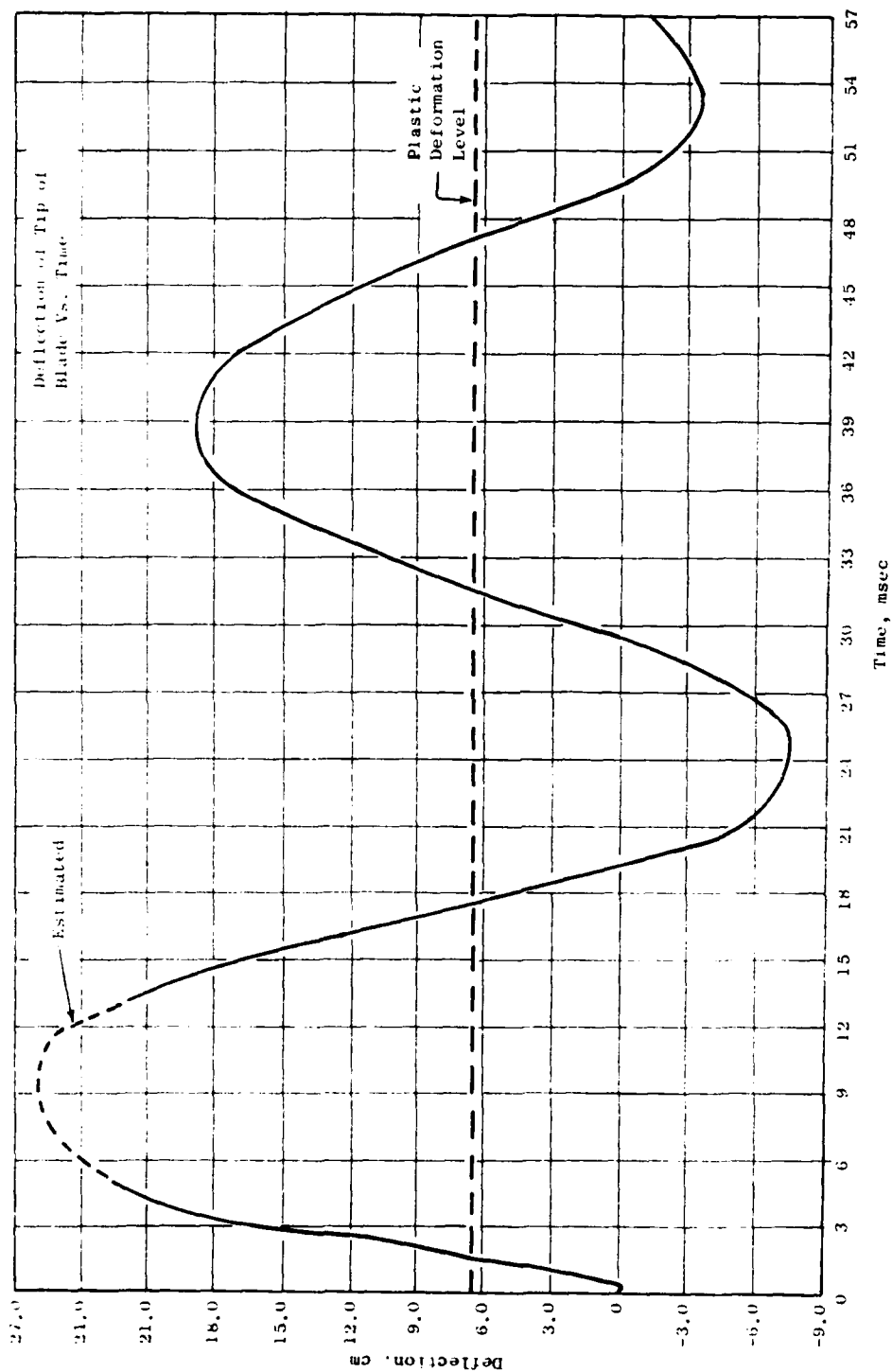


Figure 57. Tip Deflection Vs. Time for 3-Oz-Bird Impact at 70% Span on a Flat Ti Plate.

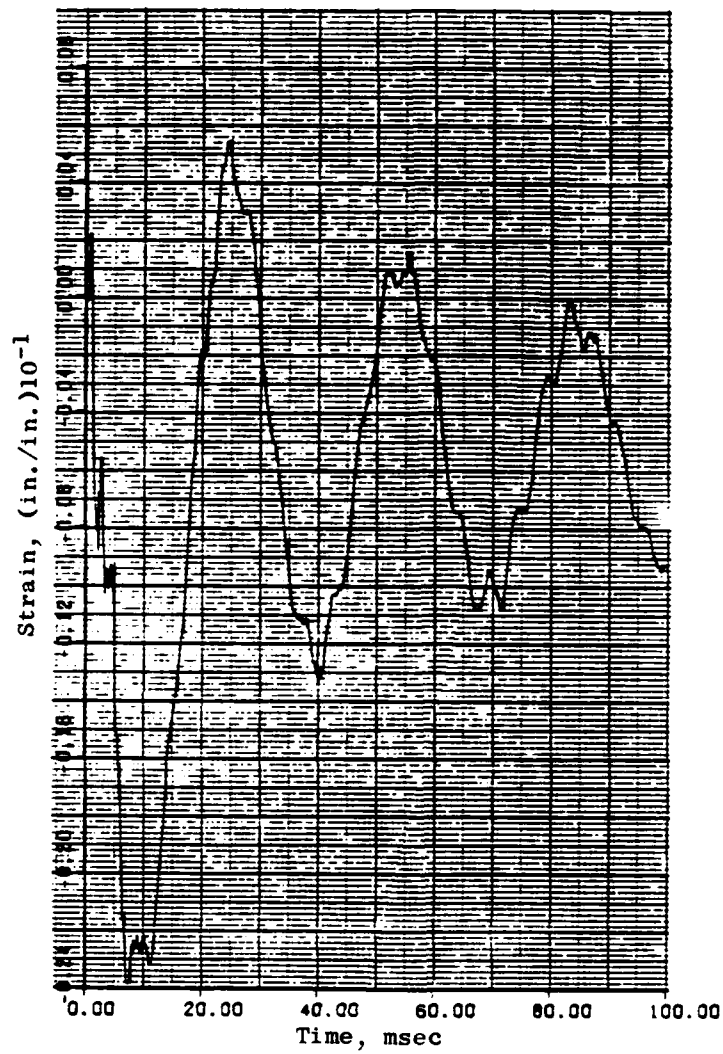


Figure 58. Strain/Time Curve for Root Gage  
in Span Direction

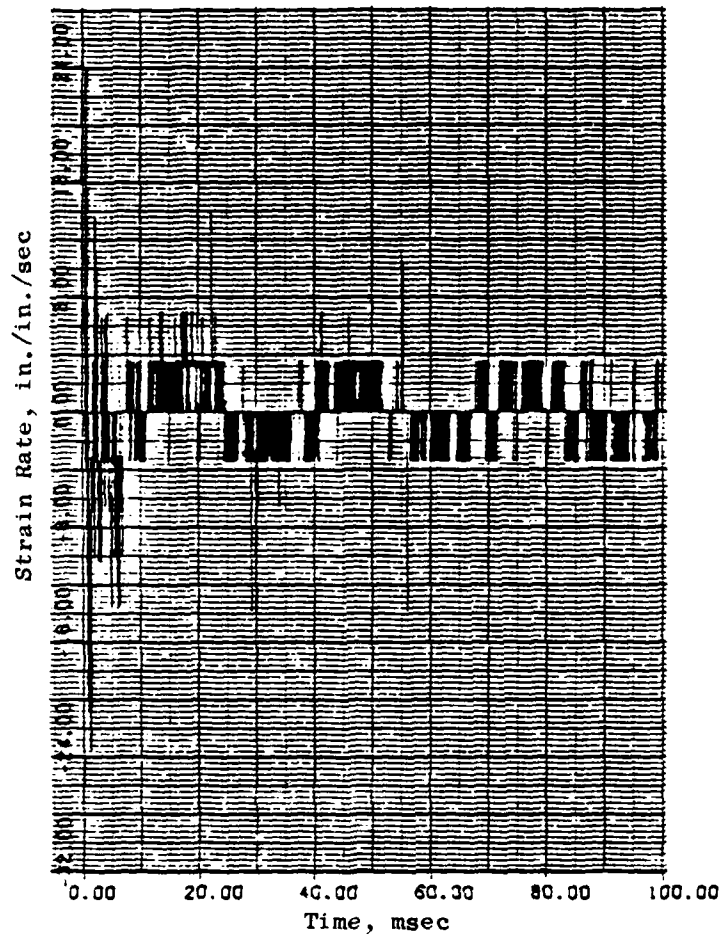


Figure 59. Strain-Rate/Time Curve for Root Gage in Span Direction.

## 9.0 TASK VII - ERROR-BAND ANALYSIS

### 9.1 INTRODUCTION

The objective of this task is to analytically determine the uncertainties in strain history, deflection history, and damage-related parameters of FOD which are introduced by such factors as manufacturing tolerance, variability in material properties, and variability in impact conditions. This determination is important in Task VIII for quantifying variances for the damage model and in Task VI and IX for comparing computer output with test results.

The damage-related parameters will be among those used in Task VIII as the basis for the impact damage model (maximum stress or maximum strain for example). These parameters will be obtained as output from the analysis models defined in Task II. It is expected that the second-level response model will be adequate, but the detailed modeling required for studying the effects of local deviations in geometry within manufacturing tolerance might require the use of the first-level-analysis response model.

### 9.2 PROPERTIES REQUIRING AN ERROR-BAND ESTIMATION

A list of geometries has been compiled relating to blade material, impactor characteristics, and aerogeometric factors for which the FOD design criteria (developed in Task VIII) will most need an error-band estimation. It is believed that variation of these properties within a reasonable range can cause a wide variation in FOD. These error-band properties and the associated damage modes are identified in the matrix shown on Table 15.

### 9.3 DAMAGE VECTOR

The concept of a damage vector will be utilized in the response models to quantify the damage modes identified previously. This damage vector will be used in conjunction with the sensitivity studies for the error-band properties. The damage vector will consist of the numerical values of perhaps a dozen quantities which signal the onset of each of the damage modes. For example, relative to blade displacement and local tearing, the locations and values of the maximum and minimum axial and tangential blade displacements and the location and values of the maximum principal strains will be included in the damage vector.

The damage vector is essentially a list of the values of the failure criteria. This vector provides the user with an appraisal of the damage sustained. The degree to which the damage vector is altered when changes are made in material, impactor, or aerogeometric parameters would identify, in an unambiguous way, the sensitivity of each damage mode to changes in these parameters.

Table 15. Matrix of Error-Band Properties and Associated Damage Modes.

Damage Modes	Metal Blades					Composite Blades					
	Stage to Stage In-terference	Mass Loss	Tear-ing	Large Plastic Deform.	Small Plastic Deform.	Stage to Stage In-terference	Mass Loss	Delami-nation	Fiber Failure	Cracking	Small Plastic Deformation
<u>Impact Para.</u>											
Weight		X	X	X	X		X				X
Location	X	X		X		X	X	X	X	X	
Duration	X			X		X			X	X	
<u>Aero/Geom-etric Para.</u>											
Tip Clear.	X					X					
Interstage and Stage to Stage Clear-ance	X					X					
Max. Thick.		X					X				
LE Thick.			X								
Thick. Dist-ribution		X		X			X				
<u>Material Parameters</u>											
Ductility	X	X	X	X		X	X				
Strain Rate		X	X	X			X		X	X	X
Yield Stress				X							
Surface Quality					X						X

## 10.0 TASK VIII - FOREIGN OBJECT IMPACT DESIGN CRITERIA

### 10.1 INTRODUCTION

The purpose of this task is to derive the criteria for predicting blade FOD tolerance. The criteria will be formulated to make full use of the transient dynamic analysis and experimental results obtained in the previous tasks and will be based on a combination of theory and regression analysis. Dimensional analysis and an examination of the physics of impact will determine which impact-dynamics and airfoil-response parameters will be used to formulate the damage model. Regression analysis will be used to determine the constants in the model by correlation with the experimental results. The experience gained at General Electric in the development of simplified criteria based on purely elastic analyses will provide an excellent basis for the complete elastic-plastic analysis of this program.

The damage models formulated will be correlated with the observed damage from Tasks VI and IX tests, and each will be sufficiently resolved to predict a threshold value beneath which the damage is not observed and above which the prescribed damage is evident. The level of damage for such definitions as local plastic deformation will be of relatively increasing severity from no damage to large plastic deformation so that multiple qualitative thresholds will be required. A more definitive damage criterion is to specify the size of the region of local plastic deformation relative to a normalizing dimension of the airfoil - such as the chord. Damage definitions, such as local fracture, are qualitatively more precise measurements; therefore, a single threshold will be sufficient.

### 10.2 DESIGN CRITERIA

An assessment has been completed of how well the structural-response models can provide the selected failure variables. It was established that the NOSAPM program in the current form provides stresses only at the Gauss points for nonlinear problems. Because a forming-limit concept has been selected that uses the relative values of the maximum and minimum principal strains to establish whether tearing occurs in metal blades, and also because the failure criteria selected for composite blades is based on the maximum bending stresses and shear stresses, the NOSAPM program will be modified to provide surface principal strains and physical stresses as well as the Gauss-point stresses. In addition, surface physical strains will be provided to allow correlation with strain gage data obtained from the Task VI impact tests. The COMET program provides physical and principal surface strains and surface stresses.

Both NOSAPM and COMET provide geometric and material nonlinear analysis capability that addresses the large-displacement, elastoplastic behavior that is characteristic of the transient response of first-stage fan and compressor

blades due to foreign-object impact. This geometric and material nonlinear-analysis capability will be used to predict local plastic deformation, such as bulging, and overall blade displacements resulting from far-field structural response.

The design criteria that have been selected will be consistent with the predictive capabilities of the Task II transient structural-response models and with the test data and methods of Task IV. They are presented below.

#### 10.2.1 Design Criteria for Use with Task II Transient Structural-Response Models and Task IV-A Test Data

##### Metal Blades

- Limit local plastic deformation to a specific percentage of chord to avoid stall/surge.
- Limit strains in the impact region in order to avoid tearing and mass loss.
- Limit strains at the root of the blade in order to prevent airfoil loss.
- Limit displacements in order to avoid contact with adjacent blades and stages.

##### Composite Blades

- Limit spanwise and chordwise normal stress in order to avoid fiber failure.
- Limit shear and through-the-thickness normal stresses in order to avoid delamination.
- Limit displacements in order to avoid contact with adjacent blades and stages.
- Limit spanwise normal stresses at the root of the blade in order to prevent airfoil loss.

#### 10.2.2 Design Criteria Based on Task IV-A, B, and C Test Data and Methods

- Utilize bank of design data to relate residual tensile and fatigue properties to local, leading-edge, ballistic-impact damage.
- Evaluate and rank candidate blade materials through screening tests that address the ballistic limit, local deformation characteristics, gross structural-damage characteristics, and residual fatigue strength.

## 11.0 TASK IX - SINGLE-BLADE IMPACT TESTS

### 11.1 INTRODUCTION

The effort of Task IX, "Single Blade Impact Tests," is concerned with corroborating analytical and parametric predictions and evaluating the validity of design criteria developed in other tasks. This will be accomplished by impact testing full-scale instrumented blades in an existing whirligig facility.

Three blade designs selected for transient-response impact analysis in Task V will be tested under test conditions that duplicate the analytical impact-parameter values used in the earlier tasks. This is necessary to obtain a direct correlation of the analytical and experimental results.

Activities conducted under this task will be carefully coordinated with the analytical studies of Task II, Task V, and Task VIII and the experimental evaluation of Task VI.

### 11.2 TEST PLAN

Impact testing of full-scale, instrumented blades will be conducted in the existing whirligig facilities. The three blade designs selected in Task V will be tested. These are the APSI fan B/A1 blade, the J79 compressor Stage 1 steel blade, and the F101 fan Stage 1 tip-shrouded titanium blade. The J79\* and APSI blades will each be tested using an APSI/J79 single-blade test disk set up in General Electric, Evendale, test cell No. 63. The F101 blades will be tested using an F101 engine disk setup with a soft-mount TF34 vehicle in General Electric, Evendale, test cell No. 62. Figure 60 shows the single-blade impact setup for the APSI and J79 blades, and Figure 61 shows the setup for the F101 blade.

Four blades of each of the three selected configurations will be impact tested. Each blade will be set up for a single-blade impact test and instrumented with three dynamic strain gages.

Rotational speed and angle for the J79 blades will be set to simulate a bird ingestion at takeoff conditions. A simulated bird (or an ice slab) will be injected into the path of the rotating blade. An existing, angled slot in the disk provides additional blade-twist angle to compensate for the zero-velocity state of the projectile on impact and to provide the proper blade-to-projectile incidence angle.

Since it is planned to use existing test hardware in this program, the APSI B/A1 blades will be tested in a slot angled to provide normal running conditions. This will result in a higher than normal incidence angle between the

---

\*Impact Testing has been completed for the J79 Blade.



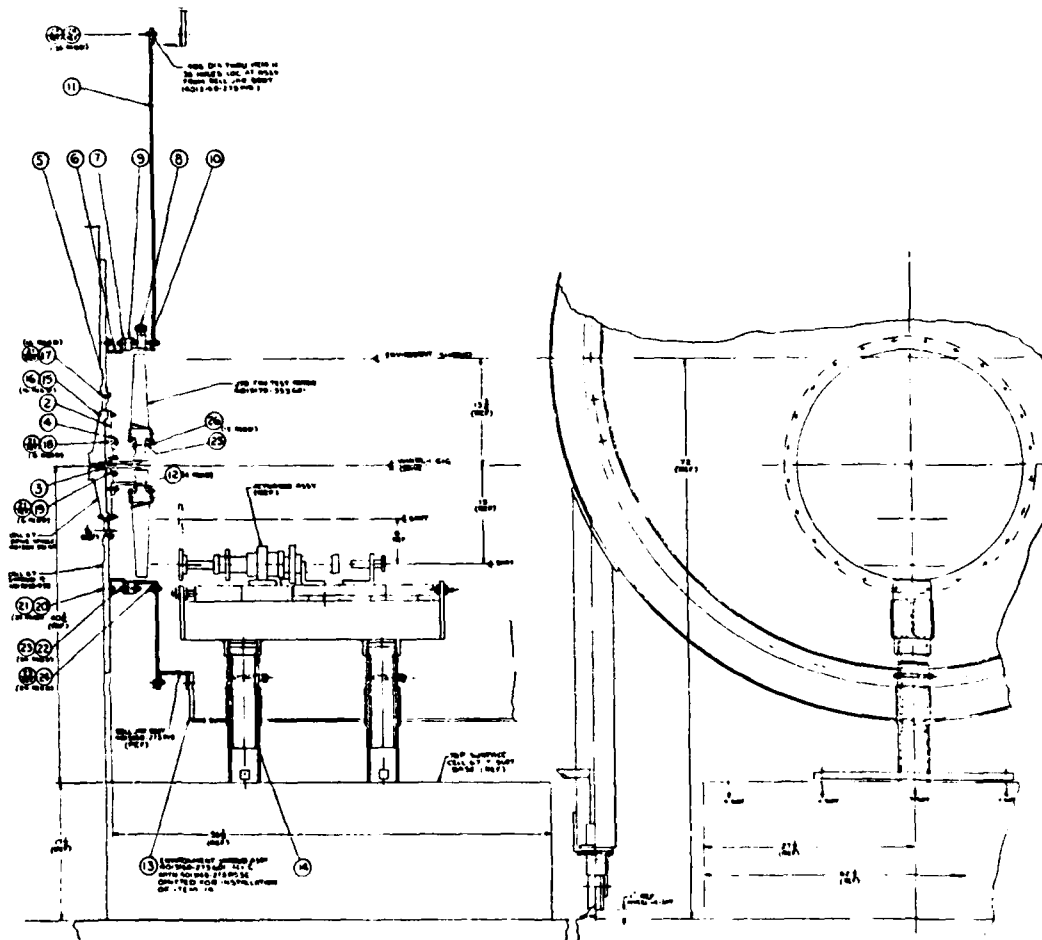


Figure 60. Test Setup for J79 and APSI Blades.

Copyright © 1964 by D.C. does not  
 permit any further reproduction

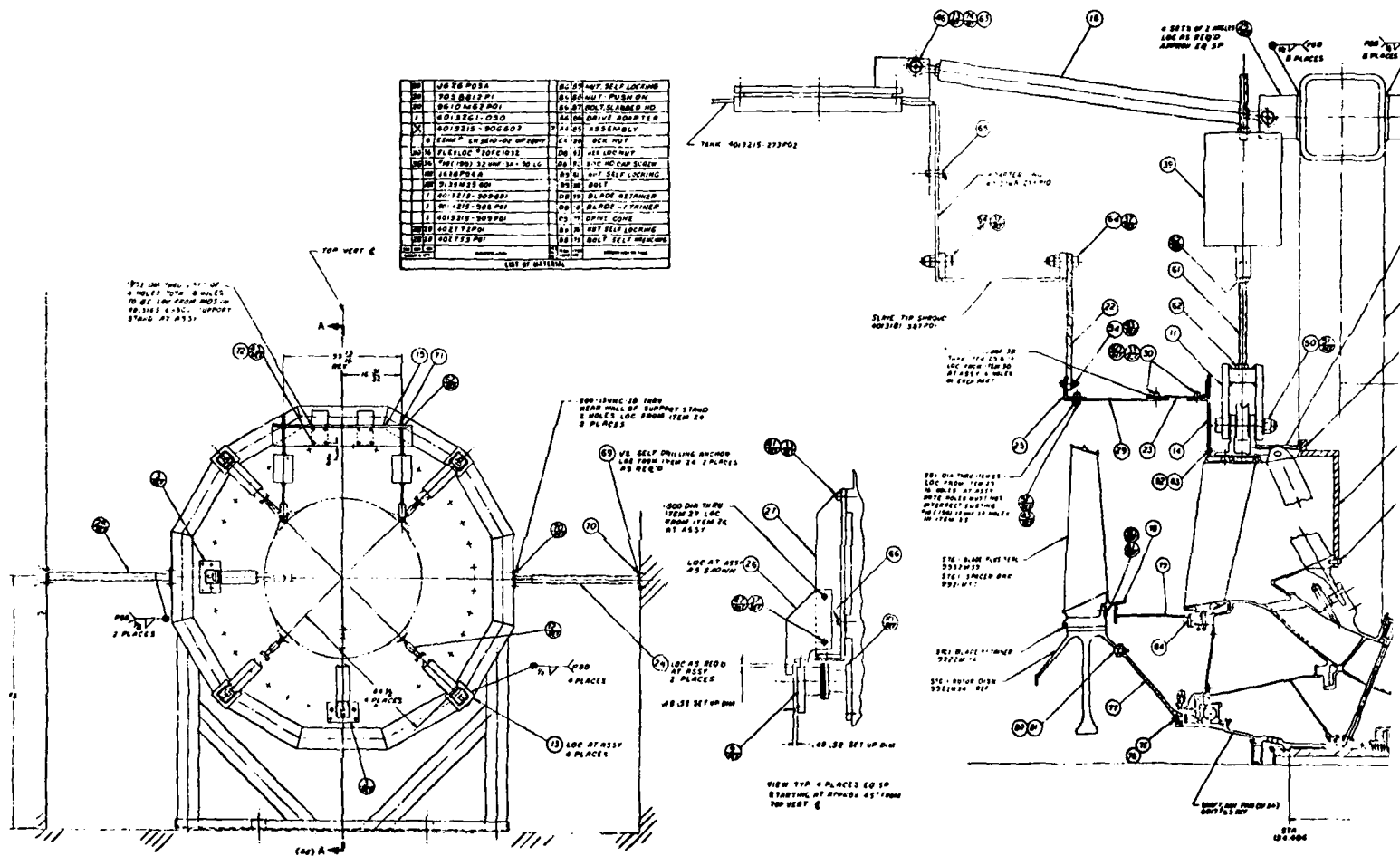
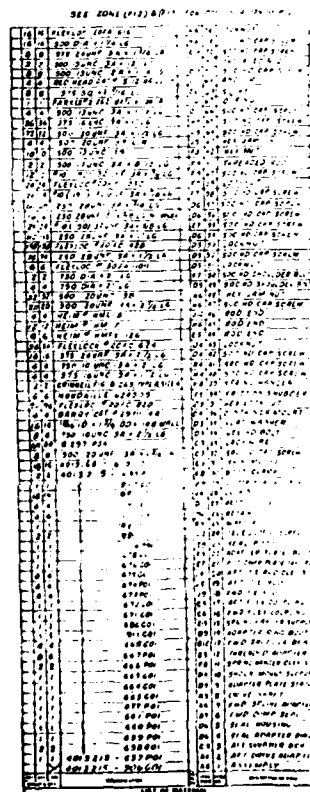


Figure 61. Test Setup for F101 Blade for Tasks



DTIC  
 COPY  
 INSPECTED  
 2

109/110

blade and the injected projectile on impact. A reduced blade rotational speed will be employed to make the impact normal energy transfer more nearly the same as for an impact at takeoff conditions. Some further reduction in rotational speed may be necessary to permit operation with the existing injection mechanism; it has not been used for rotational speeds above 10,000 rpm.

The F101 blades will also be tested, in an unrestrained state at the tip, in a disk with slots angled for normal running conditions. This again will result in a higher than normal incidence angle between the blade and the injected projectile on impact. As with the APSI blades, the blade rotational speed will be reduced to provide an impact normal energy transfer that would be the same as for an impact at takeoff condition.

No problems will result from these different rotational speeds and blade angles since the damage predictions of Tasks V and VIII will be made using the same speeds and angles as for these test conditions. The conditions shown are for simulated takeoff conditions. Blade impact locations are 30 and 70% span. The size of the bird or ice slab for the first impact at each location will be analytically selected to be just below the blade-damage condition. The projectile size for the second impact at a location will be based on analytical predictions for a level slightly above the threshold for local damage. Three blades of each configuration will be used for the bird/30% span, bird/70% span, and ice slab/70% span tests. The fourth blade of each configuration will be held in reserve. The impact conditions selected for the testing of these fourth blades will be determined by the results of the first six tests of each blade configuration. All impacts will be recorded by three high-speed cameras mounted at three different angles to obtain detailed visualization of the impact sequence and to determine the resulting blade deflections.

Each test blade will be subjected to a thorough failure analysis. The failure analysis will consist of visual inspection documented with photographs and supplemented by dimensional and dye-penetration or Magnaflux inspection. Also, frequencies in the first four modes will be measured for any blades with local impact damage. To assess the significance of the damage, selected damaged blades will be subjected to bench fatigue tests in the first-flexural or first-torsional mode and compared to available or control fatigue-test data for these blades.

### 11.3 IMPACT TESTING

#### 11.3.1 J79 Compressor Stage 1 Blade Testing

The J79 compressor Stage 1 steel blades have been single-blade tested, in the GE Evendale Cell 63 whirligig facility, using the disk and setup shown in Figure 60. The facility is comprised of an electric motor, clutch, protective shrouding, bell jar, and injection mechanism. The J79 test disk has a number of slots with different setup angles so that the blade impact angle can be selected to suit the desired impact conditions. The bird-to-blade incidence

angle was set to  $33^\circ$  for 70% radial-span location tests and  $47^\circ$  for 30% radial-span location tests. Rotor speed was 8243 rpm for the 70% span tests and 8904 rpm for the 30% span tests and provided bird-to-blade relative velocities of 809 and 580 feet per second. These angles and speeds simulate an injection at takeoff condition and are the same as would occur if the bird were shot at the engine with a velocity of 250 feet per second. The bird was simulated by a cylinder made of a microballoon gelatin mix.

Figure 62 shows the J79 blade and disk setup and the injector mechanism used to project the bird into the path of the blade. Good strain data and high-speed-movie data are available for these tests and are currently being analyzed.

#### 11.3.2 APSI Fan B/A1 Blade Testing

The APSI fan B/A1 blades will be single-blade tested in the GE Evendale Cell 63 whirligig facility using the same disk and setup as used for the J79 blade. The APSI blades, however, will be set up in the normal-blade-running angular position because the existing test disk is set up for this angle for APSI blade testing. The plan is to test the blade at a rotor speed of 11,521 rpm for the 70% span tests and at 13,846 rpm for the 30% span tests. This will provide a bird/blade incidence angle of  $27^\circ$  and bird-to-blade relative velocity of 922 feet per second for the 70% radial-span location testing and incidence angle of  $49^\circ$  and bird/blade relative velocity of 815 feet per second for 30% radial-span location testing. These conditions provide higher incidence angle and lower relative velocities than would be expected for normal takeoff conditions of this high-tip-speed blade. These test conditions appear reasonable, however, for the following reasons:

1. The resulting projectile-to-blade normal energy transfer would be approximately the same as for an impact involving a lower incidence angle and a higher relative velocity.
2. Damage predictions will be made for the same relative velocity and incidence angle as used for the testing. Predicted bird size for no damage, threshold-minor local damage, and threshold-major damage will be made.

#### 11.3.3 F101 Fan Stage 1 Blade Testing

The F101 fan Stage 1 tip-shrouded titanium blades will be single-blade tested with the tip shrouds remaining unsupported. The setup will be similar to that used for the J79 and APSI blades except that the F101 engine disk will be set up with a soft-mount arrangement in GE Evendale Cell 62 (Figure 61). Since the engine disk has all slots arranged for normal running, the bird-to-blade-impact incidence angle will be higher for single-blade testing because of the zero axial speed of the projectile.

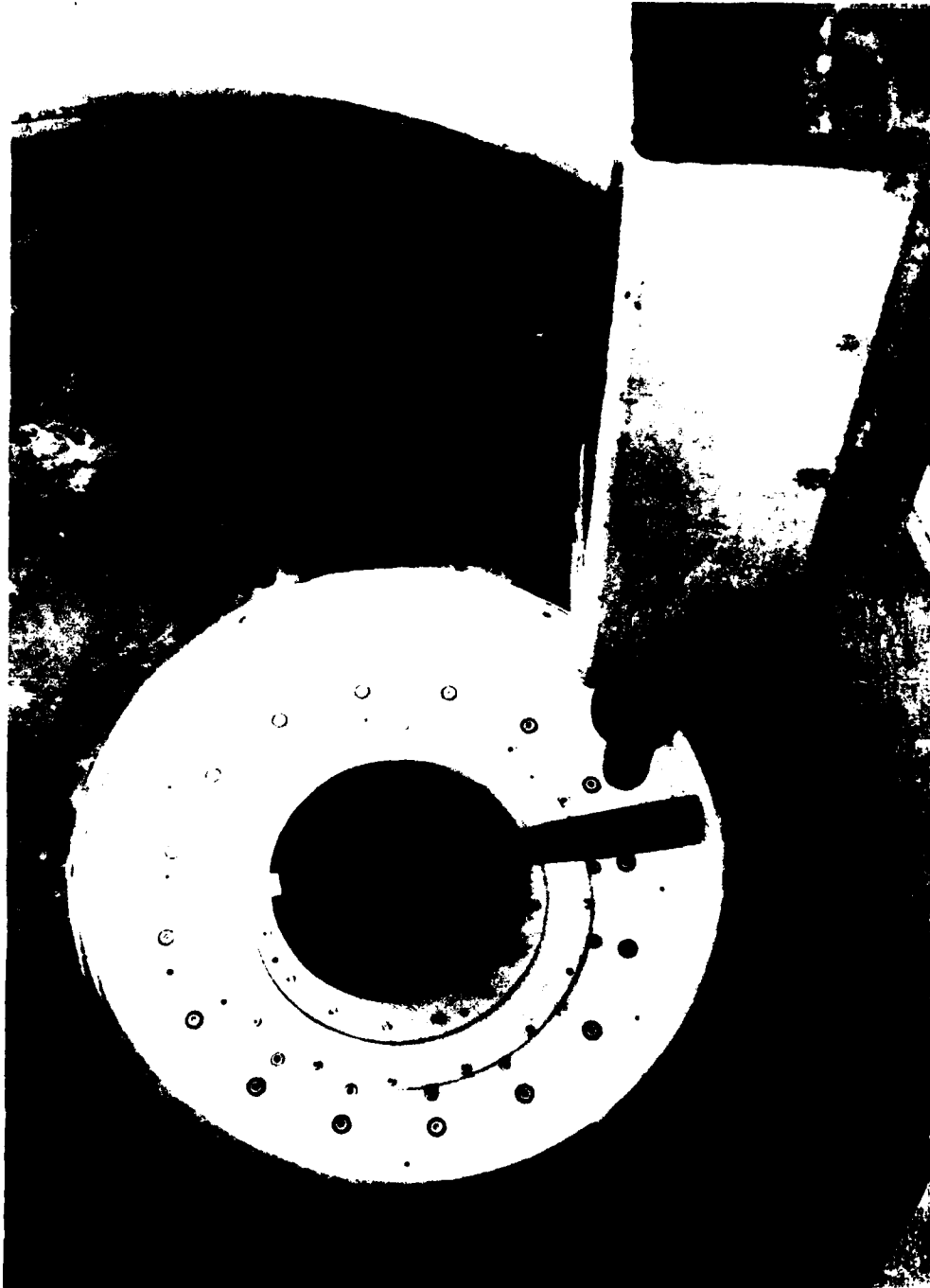


Figure 62. J79 Blade and Injection Mechanism.

The rotational speeds will be taken as 5692 rpm for 70% span tests and 6317 rpm for 30% span tests to provide the same normal energy for impact as a bird ingested at takeoff conditions while accounting for the differences in incidence angles. A projectile velocity of 200 feet per second and a fan rotational speed of 7500 rpm is considered to be a typical takeoff condition for this engine and was used to determine the above test rotational speeds.

#### 11.4 WHIRLIGIG FACILITY

The test-rig facilities (whirligig) to be used for this effort were developed to closely simulate impact conditions that occur in turbofan engines. A rig typically consists of a horizontal spindle shaft, electric motor, gearbox, shrouding, and a bell jar (Figure 63). The electric motor is a constant-speed unit with a dynamic, variable-speed output and magnetic clutch. Power is transmitted through a gearbox and a horizontal spindle shaft to the rotor. Shrouding is provided around the rotor to reduce air turbulence and, thus, heat generation and power requirements. An environmental chamber (bell jar) is soft-mounted to the facility shroud to provide a helium atmosphere to reduce the power requirement and temperatures, to provide a housing for the injection mechanism, and to enable high-speed movies to be taken of the impact sequence.

The soft-mounted vehicle setup to be used for the F101 blade testing is shown in Figure 61. It is basically a standard TF34 engine fan package with some additions and changes. The entire vehicle is soft-mounted and is supported by spring-type hangers and dampers. The test disk is an F101 Stage 1 rotor disk adapted to the setup through a special drive cone. The rotor is driven by a flexible coupling and slave adapting shaft. The extremely high rotor vibrations resulting from loss of significant portions of a blade during impact testing are reduced by the spring-and-damper mounting. The flexible drive coupling prevents damage to the facility drive spindle and bearings that might otherwise result from large, fan-rotor displacements.

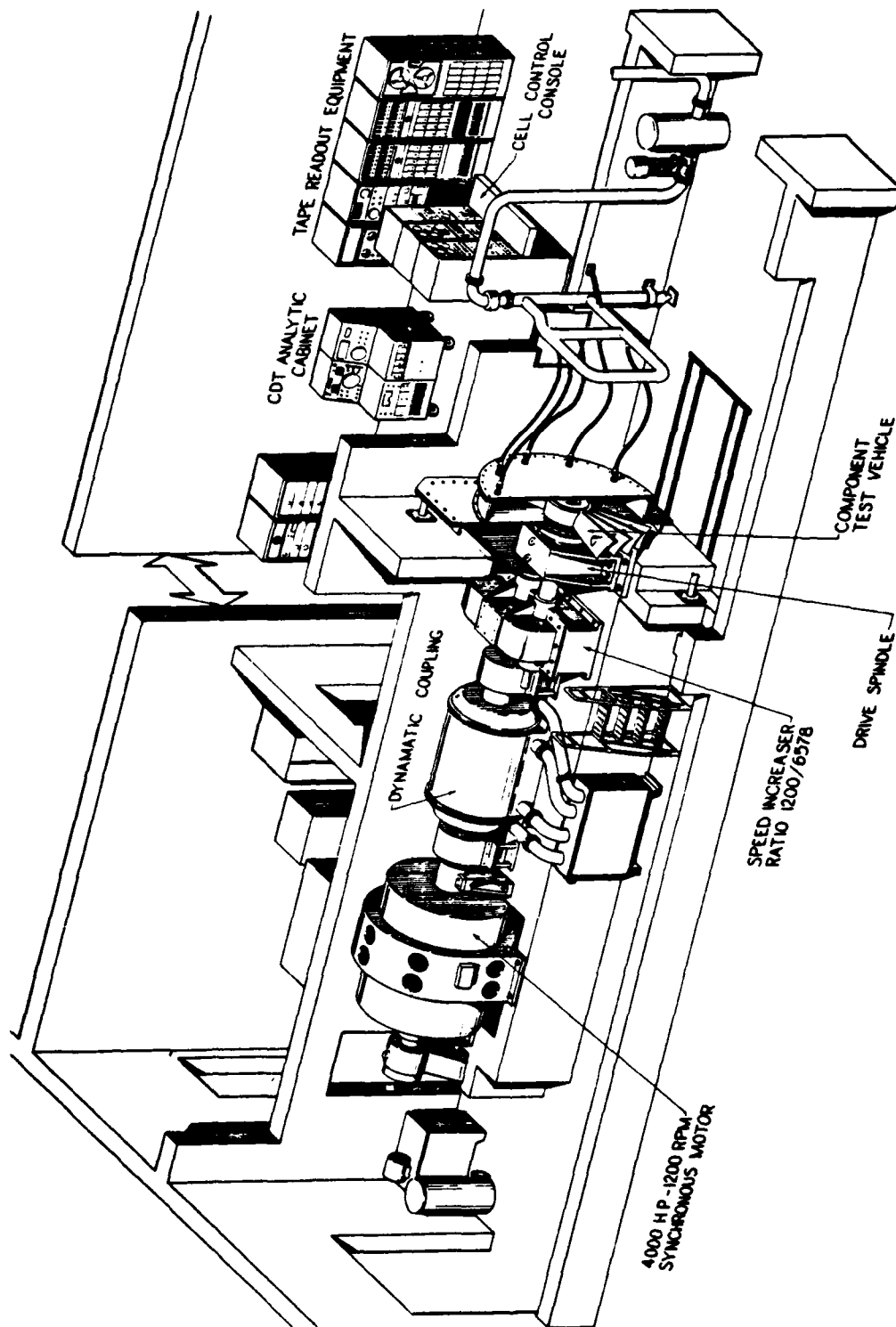


Figure 63. Whirligig Test Facility.



## 12.0 TASK X - FULL-STAGE RESPONSE PREDICTION

### 12.1 INTRODUCTION

The purpose of this task is to predict the initial response of a full set of blades by applying the final analytical models of Task II, the final loading models of Task III, and the final damage models of Task VIII.

### 12.2 ANALYSIS APPROACH

The principal difference between this analysis and those made in Task V for analysis of the single-blade rotating tests of Task IX is the interactive influence of multiple airfoils. The major interactive mechanism occurs when the airfoils are interconnected with part-span shrouds or tip shrouds.

The effect of the concentrated stiffness represented by the shroud will be included in the first- and second-level analyses of Task II through the use of spring elements. This modeling approach will be modified and refined as necessary based on the analyses and test results of Tasks V, VI, and IX. The results of that effort will be utilized in Task X to make the full-stage response prediction.

An additional interaction between airfoils can take place through the dovetails and disk, but this is greatly dependent upon the relative stiffness of the disk rims, the solidity of the stage, the size of the foreign object, and the proximity of the impact to the root of the airfoil. In general, the interaction at the dovetail is usually much less than the interaction at the shrouds.

The cost for running the second-level model (COMET) for far-field analysis would be prohibitive because of the small time step required. We will use the first-level model (NOSAPM) for far-field analysis through the restart capability of this program, and both COMET-FOD and NOSAPM will be used for local-damage/small-time-period analysis.

### 12.3 Response Predictions

Predictions will be made for the F101 shrouded titanium blades. The predictions will span the range of expected foreign objects (small birds, large birds, and ice) and will include relative severities ranging from minor damage to the most severe engine and aircraft ingestion condition, as identified in Task I, which can be expected to result in severe airfoil damage. These predictions will be used to select the impact parameters for the Task XI full-scale tests; the results of these tests will be used, in turn, to make the final correlative adjustments in the models as may be required.

### 13.0 TASK XI - FULL-SCALE IMPACT TESTS

#### 13.1 INTRODUCTION

The object of Task XI, "Full-Scale Impact Tests," is to validate the Task X prediction of how a full stage of shrouded blades will response to impact loadings. The validation will be accomplished by impact testing a full stage of F101 tip-shrouded blades in an existing whirligig facility.

The tests will be conducted under test conditions that duplicate the analytical impact-parameter values used for prediction purposes in Task X. Enough blades will be instrumented to provide the response data needed for the validation. The use of duplicate test and analytical impact parameters will permit a direct correlation of the analytical and experimental results.

Activities conducted under this task will be carefully coordinated with the experimental and analytical studies of Tasks V, VI, IX, and X.

#### 13.2 TEST PLAN

Impact tests will be conducted on a full stage of F101 fan blades in an existing whirligig facility. The F101 fan Stage 1 tip-shrouded titanium blade was selected in Task V for single-blade impact testing in Task IX and the full-stage testing of this Task IX. The blades will be tested using an F101 engine disk setup in a soft-mount TF34 vehicle in General Electric Evendale Cell No. 62. Figure 61 shows the test setup.

Two tests will be conducted. In the first test, the blades will be impacted by a real bird; in the second test, they will be impacted by an ice slab. A summary of the impact-test conditions is presented in Table 16. Rotational speed and projectile velocities will be set to simulate ingestions at takeoff conditions. For both tests, the rotational speed will be 7500 rpm, and the impacts will be at 70% span. The bird will be shot into the blades at a velocity of 200 ft/sec and the ice slab at 75 ft/sec. For each test, nine blades will be instrumented with three gages apiece. This is sufficient instrumentation to record the responses of the impacted and adjacent blades.

The projectile size for each of the tests will be determined in Task X and will be based on an analytically predicted low level of blade damage which slightly exceeds the threshold for local damage. Both impact tests will be recorded by three high-speed cameras mounted from three different angles to obtain detailed views of the impact sequence and to determine the resulting blade deflections.

All damaged blades will be subjected to a thorough failure analysis. The failure analysis will consist of visual inspection documented with photographs and supplemented by dimensional and magnetic-particle inspection.

### 13.3 IMPACT TESTING

#### 13.3.1 F101 Fan Stage 1 Blades - Bird-Ingestion Test

A full stage of F101 fan Stage 1 tip-shrouded titanium blades will be subjected to a single bird impact. The setup will be similar to the setup for the single-blade testing in Task IX, the major difference being that the disk will contain a full set of 50 blades. The F101 disk will be set up with a soft-mount arrangement in General Electric Evendale Cell 63 (Figure 61). Since an engine disk will be used, and the projectile will be shot into the rotor at the same speed expected for the takeoff condition being simulated, the rotor speed will also be the same as for actual engine operation. This will provide conditions identical to those expected for a similar bird ingestion during engine operations. The test conditions are defined in Table 16.

#### 13.3.2 F101 Fan Stage 1 Blades - Ice-Slab-Ingestion Test

The ice-slab-ingestion test will follow the previously described bird-ingestion test. A full stage of F101 blades will be tested. The more severely damaged blades from the first test will be replaced before this test is conducted. The point of impact for this test will again be at the blade 70% span location but will be targeted to occur at a location 180° circumferentially on the rotor from the first test impact. The same basic test setup will be employed, and test conditions will be selected to simulate an ice-slab ingestion at takeoff conditions (Table 16). The ice slab will be an ice spear of approximately 2 inch by 2 inch by 2 inch triangular cross section with a length compatible with the mass predicted to cause an appropriate level of damage in the blades.

### 13.4 WHIRLIGIG FACILITY

The test-rig facilities (whirligig) to be used for this effort were developed to closely simulate impact conditions that occur in turbofan engines. A rig typically consists of a horizontal spindle shaft, electric motor, gearbox, shrouding, and a bell jar (Figure 63). The electric motor is a constant-speed unit with a dynamic, variable-speed output and magnetic clutch. Power is transmitted through a gearbox and a horizontal spindle shaft to the rotor. Shrouding is provided around the rotor to reduce air turbulence and, thus, reduce heat generation and power requirements. An environmental chamber (bell jar) is soft-mounted to the facility shroud to provide a helium atmosphere to reduce the power requirement and temperatures, and to enable high-speed movies to be taken of the impact sequence.

The vehicle setup to be used for the F101 blade testing is shown in Figure 61. It is basically a standard TF34 engine fan package with some additions and changes. The entire vehicle is soft-mounted and is supported by spring-type hangers and dampers. The test disk is an F101 Stage 1 rotor disk adapted to the setup through a special drive cone. The rotor is driven by a flexible

Table 16. Planned Test Conditions for Full-Stage Whirligig Impact Tests.

- Simulated Takeoff
- F101 Stage 1 Fan

	Test No. 1	Test No. 2
Blade Type	Tip-Shrouded	Tip-Shrouded
Blade Material	Titanium 8-1-1	Titanium 8-1-1
Number of Blades	50	50
Number of Blades Instrumented	9	9
Projectile Type	Real Bird	Ice Slab
Projectile Speed	200 ft/sec	75 ft/sec
Rotor Speed	7500 rpm	7500 rpm
Blade Tip Speed	1468 ft/sec	1468 ft/sec
Impact Location	70% Span	70% Span
Incidence Angle	25°	31°
Relative Velocity	1263 ft/sec	1245 ft/sec
Basis for Projectile Size	Threshold Damage	Threshold Damage

coupling and slave adapting shaft. The extremely high rotor vibrations resulting from loss of significant portions of a blade during the impact test are reduced by the spring-and-damper mounting. The flexible drive coupling prevents damage to the facility drive spindle and bearings that might otherwise result from large, fan-rotor displacements.

### 13.5 GAS GUN FACILITY

The gas gun mechanism basically consists of a pressure vessel, a rupture disk assembly, and the gun barrel. The bird is contained in a cylindrical carrier that is propelled down the gun barrel when the pressurized gas (helium) is released. The carrier is retained at the end of the barrel, and the bird is shot out.

A mylar membrane acts as the diaphragm of the rupture disk assembly. Rupture of the diaphragm occurs when the mylar is weakened by heat. A typical gas gun shot-triggering sequence might be as follows.

After the desired rotor speed is reached, a high-speed camera is activated manually. A relay in the camera trips when the film is at speed. The relay activates the flash-lighting system and the whirligig triggering system. After a preset time delay, the whirligig triggering system activates a hot wire that melts the mylar diaphragm, thus, "firing" the projectile.

The technique of synchronizing the bird with the rotor to impact a particular segment of blades is accomplished by using the whirligig triggering system and the hot-wire power-supply unit. The hot-wire power-supply unit was designed and built specifically for the purpose of rupturing the diaphragm rapidly and predictably. The whirligig triggering system has a very precise timing circuit that can be varied and is dialed in to allow for the operating time of the gas gun system and to account for the angular position of the blade segment relative to a 1/rev indicator on the rotor.

## REFERENCES

1. Storace, A.F., "Initial Research and Development Test Plan, Task I - Design System Structure," November 1977.
2. Description of the First and Second Level Analytical Models to be Used in FOD Studies, submitted to Air Force in a letter, A.L. Meyer to Lt. Paul Copp, AFAPL/TBP, December 5, 1977.
3. Levy, S. and Wilkinson, J., The Component Element Method in Dynamics, McGraw-Hill, 1976.
4. Levy, S., "Pipe Whip Dynamics Including Pipe Yielding, Nonlinear Restraints and Variable Jet Force for 3D Systems," General Electric Corporate Research and Development Report No. 77CRD083, March 1977.
5. Wu, R., "Dynamic Analysis of Fuel Assemblies Including Fluid Effects," NEDM-21236, 76NED17, March 1976.
6. Barber, J.P., Wilbeck, J.S., and Taylor, H.R., "Bird Impact Forces and Pressures on Rigid and Compliant Targets," AFFDL-TR-60, November 1978.
7. 1977 Annual Book of ASTM Standards, Part 10 - Metal Physical, Mechanical, Corrosion Testing, pp. 154-173.
8. Structural Design Guide for Advanced Composite Applications, Volume I, Material Characterization - Test Methods, p. 7.3.5.
9. Chamis, C.C. and Sinclair, J.H., "Ten-Degree Off-Axis Test for Shear Properties in Fiber Composite," Experimental Mechanics, September 1977, pp. 39-346.
10. Krinke, D.C., Barber, J.P., and Nicholas, T., "The Charpy Impact Tests as a Method for Evaluating Impact Resistance of Composite Materials," UDRI-TR-77-54.
11. Zienkiewicz, O.C., The Finite Element Method in Engineering Science, McGraw-Hill, Maidenhead, Birkshire, England, 1977, pp 279-285.
12. Stagliano, T.R. and Mente, L.J., "Large Deflection, Elastic Plastic Dynamic Structural Response of Beams and Stiffened or Unstiffened Panels...", Proceedings of the Second ADINA Conference, Cambridge, Mass., August 1-3, 1979, to be published as an M.I.T. Report.